

2016

Development and application of an optogenetic platform for controlling and imaging a large number of individual neurons

<https://hdl.handle.net/2144/17082>

"Downloaded from OpenBU. Boston University's institutional repository."

BOSTON UNIVERSITY
COLLEGE OF ENGINEERING

Dissertation

**DEVELOPMENT AND APPLICATION OF AN
OPTOGENETIC PLATFORM FOR CONTROLLING AND
IMAGING A LARGE NUMBER OF INDIVIDUAL NEURONS**

by

ALI IBRAHIM ALI MOHAMMED

B.Sc., Helwan University, 2001
M.Sc., Texas Tech University, 2011

Submitted in partial fulfillment of the
requirements for the degree of
Doctor of Philosophy

2016

© 2016 by
Ali Ibrahim Ali Mohammed
All rights reserved

Approved by

First Reader

Xue Han, Ph.D.
Assistant Professor of Biomedical Engineering

Second Reader

Jerome Mertz, Ph.D.
Professor of Biomedical Engineering

Third Reader

Ian Davison, Ph.D.
Assistant Professor of Biology

Fourth Reader

Elise Morgan, Ph.D.
Professor of Mechanical Engineering

The noblest pleasure is the joy of understanding. [Leonardo da Vinci]

ACKNOWLEDGMENTS

I would like to thank my dissertation advisory committee for guiding me through this process and providing me with essential and rich feedback along the way. Their insights have been a crucial component of the production of this work. I would also like to express gratitude for all of the members of my laboratory who offered advice and technical knowledge over the past five years.

I would like to thank my adviser Dr. Xue Han. Working with her has been a tremendous opportunity. She has given me a truly unique opportunity for entering the field of neuroengineering.

Finally, I would like to thank Dr. Jerome Mertz for supporting me, He was my great model to be a scientist. All the time he is inspiring me and give me hopes to be a great scientist.

**DEVELOPMENT AND APPLICATION OF AN
OPTOGENETIC PLATFORM FOR CONTROLLING AND
IMAGING A LARGE NUMBER OF INDIVIDUAL NEURONS**

ALI IBRAHIM ALI MOHAMMED

Boston University College of Engineering, 2016

Major Professor: Xue Han, Ph.D., Assistant Professor of Biomedical Engineering,

ABSTRACT

The understanding and treatment of brain disorders as well as the development of intelligent machines is hampered by the lack of knowledge of how the brain fundamentally functions. Over the past century, we have learned much about how individual neurons and neural networks behave, however new tools are critically needed to interrogate how neural networks give rise to complex brain processes and disease conditions. Recent innovations in molecular techniques, such as optogenetics, have enabled neuroscientists unprecedented precision to excite, inhibit and record defined neurons. The impressive sensitivity of currently available optogenetic sensors and actuators has now enabled the possibility of analyzing a large number of individual neurons in the brains of behaving animals. To promote the use of these optogenetic tools, this thesis integrates cutting edge optogenetic molecular sensors which is ultrasensitive for imaging neuronal activity with custom wide field optical microscope to analyze a large number of individual neurons in living brains. Wide-field microscopy provides a large field of view and better spatial resolution approaching the Abbe diffraction limit of fluorescent microscope. To demonstrate the advantages of this optical platform, we

imaged a deep brain structure, the Hippocampus, and tracked hundreds of neurons over time while mouse was performing a memory task to investigate how those individual neurons related to behavior. In addition, we tested our optical platform in investigating transient neural network changes upon mechanical perturbation related to blast injuries. In this experiment, all blasted mice show a consistent change in neural network. A small portion of neurons showed a sustained calcium increase for an extended period of time, whereas the majority lost their activities. Finally, using optogenetic silencer to control selective motor cortex neurons, we examined their contributions to the network pathology of basal ganglia related to Parkinson's disease. We found that inhibition of motor cortex does not alter exaggerated beta oscillations in the striatum that are associated with parkinsonianism. Together, these results demonstrate the potential of developing integrated optogenetic system to advance our understanding of the principles underlying neural network computation, which would have broad applications from advancing artificial intelligence to disease diagnosis and treatment.

TABLE OF CONTENTS

ACKNOWLEDGMENTS	v
ABSTRACT.....	vi
TABLE OF CONTENTS.....	viii
LIST OF TABLES	xi
LIST OF FIGURES	xii
CHAPTER ONE: Introduction and Background.....	1
1.1 Introduction to brain neural network measurement techniques:.....	1
1.2 Calcium (Ca ²⁺) Sensitive Fluorescent Dyes and Protein for imaging neural activities:	2
1.3 In vivo Optical imaging instruments:	4
1.4 Hippocampus function:	9
1.5 Blast Injury to The Brain:	15
1.6 Parkinson Disease and Basal Ganglia:.....	19
CHAPTER TWO: Methods	22
2.1 Animal Preparation for surgery:	22
2.2 Custom Fabrication of Cannula, Animal Holders:	25
2.3 Animal Behavior Protocol:	29
2.4 Wide Field fluorescence Imaging Setup:	32
2.5 Image Processing:	34

2.6	Blast Wave Measurements, Calibration and Procedure:.....	39
2.7	Electrophysiology Recording, pharmacology and Optogenetics.....	42
CHAPTER THREE: High speed wide-field fluorescence imaging in		44
	awake behaving mice yields data from hundreds of individual neurons	44
	over millimeters of tissue with high temporal resolution.	44
3.1	Abstract:	44
3.2	Introduction:.....	45
3.3	Result:	49
3.4	Discussion:	72
CHAPTER FOUR: Calcium Imaging Enables The Analysis of Neural Network Upon Mechanical Blast Relevant to Traumatic Blast Injury.		78
4.1	Abstract:	78
4.2	Introduction:.....	78
4.3	Result:	80
4.4	Discussion:	90
CHAPTER FIVE: Optogenetics Interrogation of Basal Ganglia Network Relevant for Parkinson’s disease		93
5.1	Abstract:	93
5.2	Introduction:.....	94
5.3	Results:.....	95
5.4	Discussion:	102

CHAPTER SIX: Conclusion and Future Work	105
References	107

LIST OF TABLES

Table 1-1: GCaMP comparison in vivo.....	4
Table 1-2: Comparison of Imaging Technique used in Brain Studies.....	19
Table 2-1: camera specifications.....	33
Table 3-1: Behavioral performance and imaging signal to noise ratio.....	55
Table 3-2: Summary of ROIs detected and motion indexes from all animals in study.	61
Table 3-3: Spatial clustering of neurons by modulation type.....	68

LIST OF FIGURES

Figure (1-1). Fluorescence dynamics and spikes in a GCaMP	4
Figure (1-2). Two Photon Microscopy.....	6
Figure (1-3). Wide Field Microscopy.....	9
Figure (1-4) Hippocampus Place Cells Experiment.....	12
Figure (1-5) Illustration Cartoon of hippocampus Circuitry.....	15
Figure (1-6) fMRI Brain Imaging.....	17
Figure (1-7). A graphical representation of a postulated cognitive reserve.....	18
Figure (2-1). Mice Surgical Preparation.....	24
Figure (2-2). Custom Fabrication Holders.....	26
Figure (2-3). Eye-Blink Experiment Setup.....	30
Figure (2-4).Camera Specifications.....	33
Figure (2-5). The process of image processing.....	35
Figure (2-6). Blasting System Setup.....	40
Figure (3-1). (A) Diagram of image acquisition system and behavioral apparatus.....	50
Figure (3-2): Imaging and identification of individual CA1 neurons.....	57
Figure (3-3): Tone evoked responses sorted by response magnitude.....	62
Figure (3-4): Tone evoked responses sorted by latency to peak amplitude.....	65
Figure (3-5): Spatial organization of task related CA1 neurons.....	69
Figure (3-6): Wide field ROI maps for other study subjects.....	70
Figure (3-7): Histograms of distance between cells.....	71
Figure (4-1). Example of some individual imaging CA1 neurons over time.....	83

Figure (4-2). Neurons response magnitude before and after blasting of blasted Mice 1- Day 1	86
Figure (4-3). Neurons response magnitude before and after blasting of blasted Mice 1- Day 2.....	87
Figure (4-4). Z-stack projection of average fluorescence magnitude value.....	88
Figure (4-5). Neurons response magnitude before and after sham blasting of Control Mice.....	88
Figure (4-6). Histogram of neurons average response magnitude for different time windows.....	89
Figure (4-7). Calculating Average Entropy for All of our mice Over Time windows.....	89
Figure (4-8). Calculating Maximum difference in Average Entropy for All of our mice for Blasted Mice and Control Mice.....	90
Figure (5-1). Illustration of the infusion cannula, recording electrodes and optogenetic stimulation fiber configurations.....	96
Figure (5-2). Spectrogram from an individual mouse pre and post striatal carbachol infusion.....	97
Figure (5-3). Population striatum LFP power spectral density.....	98
Figure (5-4). Recording in striatum and M1.....	100
Figure (5-5). Recording in striatum and M1 by using carbachol infusion into the striatum and optogenetic silencing of M1 pyramidal cells.....	102

CHAPTER ONE: Introduction and Background

1.1 Introduction to brain neural network measurement techniques:

The brain is the most sophisticated organ in the body. It receives, computes and sends millions of bits of information all the time in the form of nerve impulse signals and chemical signals. The exchange of this information dictates our bodily function in daily life. Technology provides many useful tools to investigate brain function and exchange of information. There are a variety of techniques to measure brain activities, which are different in spatial resolution, temporal resolution and measured phenomena. fMRI is used to measure "average activity" based on oxygenation and deoxygenation process with a spatial resolution at the scale of 1 mm^3 (100,000 neurons) and a temporal resolution of 1 second. EEG has a better time resolution on the order of 1 ms to measure electrical activity, and MEG on the equivalent time scale to measure magnetic signal, but both have poor spatial resolution of centimeters. These techniques are however noninvasive, without the need of opening the skull. On the other hand, Calcium imaging can provide a middle level to measure brain activity with reasonable spatial resolution (1 neuron) and time resolution. This technique will be described in details in the next part. Electrophysiology techniques such as multi-unit recording and patch clamp recording could record from ~200 neurons with a time resolution of 1 ms, but skull have to be opened for recording. In general, existing techniques, each has its own advantage and disadvantage and suitability of use depending on the type of experiments that we are running.

1.2 Calcium (Ca^{2+}) Sensitive Fluorescent Dyes and Protein for imaging neural activities:

Calcium imaging involves two different approaches. The first one is to develop and improve calcium sensors, and the second is to implement and improve optical methods for imaging. The rapid progress and development of imaging instruments and techniques added a new horizon to calcium imaging, in parallel to the development of fluorescent indicators. A remarkable landmark in the field of functional imaging of biological systems happened upon the emergence of a nonlinear optical scanning microscopy known as Two-photon microscopy (Denk et al., 1990), which is now used all over the world in many laboratories for calcium imaging in neuroscience.

There are a variety of available Ca^{2+} indicators that are used to investigate calcium transients in firing neurons [Kerr, R. et al. 2000, Tank, D et al. 1988, Sabatini, B. L et al. 2002]. Choosing between those Ca^{2+} indicators for experiment must be evaluated in terms of the Ca^{2+} signals, which are going to be measured. Change in Ca^{2+} concentration is a pivot principle underlying the use of Ca^{2+} indicators. Tracking the activity of neuronal populations is the main goal of calcium imaging experiments [Ohki, K. et al. 2005, Huber, D. et al. 2012].

Indicator affinity for Ca^{2+} is considered an important parameter for choosing indicators in experiment, because low-affinity indicators are recommended for large Ca^{2+} signals and high-affinity Ca^{2+} indicators are useful for relatively small changes in Ca^{2+} concentration. Quin-2, fura-2, indo-1, and fluo-3 were the first group of calcium indicators developed for

biological experiments. Quin-2 is excited by ultraviolet light (339 nm), however it is not bright (Pozzan et al., 1982 and Tsien et al., 1982). Fura-2 (Grynkiewicz et al., 1985) is excited at 350 and/or 380 nm and brighter than Quin-2. Fluo-4 dye could be excited by a range of wavelengths (Paredes et al., 2008) and it has been broadly used in neuroscience.

An important next breakthrough was the introduction of protein-based genetically encoded calcium indicators (GECIs) (Miyawaki et al., 1997). The first groups of GECIs showed slow response kinetics and low signal-to-noise ratios, which somewhat limited their use in neuroscience experiments. The improved GECI, GCaMP6 was spectacular, and gave rise to a good tool for imaging purpose (Looger and Griesbeck, 2011 and Rochefort et al., 2008). GECIs can be targeted to specific cell types, which is important for studying neural circuitry and how each type of neuron contributes to a circuit (Tian, L. et al. 2009, Zariwala, H. A. et al. 2012). GCaMP6 is brighter, more stable, has larger dynamic range, higher affinity for calcium, more photostable, greater sensitivity and faster kinetics (Figure 1-1) [Tian, L. et al. 2009, Zariwala, H. A. et al. 2012, Akerboom, J. et al. 2012, Nakai, J. et al. 2001]. Table (1-1) shows difference between different types of GCaMPs (Tsai-Wen Chen & Douglas S. Kim. et al. 2013).

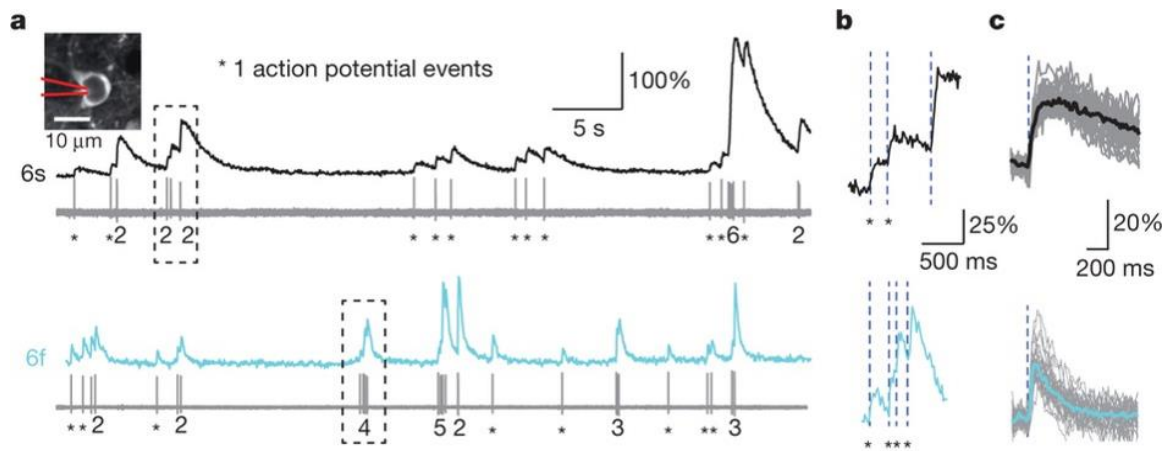


Figure (1-1). (A) Fluorescence dynamics and spikes in a GCaMP6s (top) and a GCaMP6f (bottom) expressing neuron. The number of spikes for each burst is indicated below the trace. (B) Zoomed-in view of bursts of action potentials. (C) Fluorescence change in response to one action potential. (Figure is adapted from Tsai-Wen Chen et al. 2013).

Table (1-1) GCaMP comparison in vivo (Adapted from Tsai-Wen Chen et al. 2013).

Sensor	$\Delta F/F_0$, 1 AP	Decay $\tau_{1/2}$ 1 AP (ms)	Rise τ_{peak} 1 AP (ms)
GCaMP5k	$3.6 \pm 1.9 \%$	$268 \pm 20 \%$	$60 \pm 20 \%$
GCaMP6s	$23 \pm 3.2 \%$	$550 \pm 52 \%$	$179 \pm 23 \%$
GCaMP6m	$13 \pm 0.9 \%$	$270 \pm 23 \%$	$80 \pm 7\%$
GCaMP6f	$19 \pm 2.8 \%$	$142 \pm 11 \%$	$45 \pm 4 \%$

1.3 In vivo Optical imaging instruments:

Simultaneous measurement of neural activity in the context of their spatial locations introduces a new trend to understand functional neurons and their networks. In addition, using optical imaging in conjunction with calcium indicators will allow imaging of neural populations in vivo, including deep brain tissue with a spatial resolution depending on the specific optical techniques used.

1.3.1 Two photon microscopy:

Two-photon microscopy gives rise to better resolution and contrast in biological tissues due to its lower sensitivity to scattering light, because scattering is a major problem in optical imaging that leads to resolution degradation. The pivot idea underlying the working principle is that two photons arrive 'simultaneously' (within 0.5 fs) at a molecule, and then combine their energies to promote the molecule to an excited state for a transient period of time, which was followed by a normal fluorescence-emission (Figure 1-2A). The absorption of photons depends on the properties of the molecule, and the property of the excitation light. Excitation light is achieved by generating laser beam squeezed spatially and temporally, called laser ultrashort' pulses (less than a picosecond to femtosecond long), which has high peak intensities. For laser pulses with a Rate R and a pulse width τ , the signal gets enhanced by a factor of $1 / (\tau R)^{n-1}$ relative to continuous wave illumination, where n is the number of photons (Denk, W. & Svoboda, K. et al. 1997). Two-photon microscopy needs laser pulses of about 100 fs width and repetition rates of approximately 100 MHz to match the nanosecond fluorescence lifetime of many fluorophores. Ti:sapphire laser with 700 – 1100 nm tunable output is commonly used in ultrashort pulse generation (Xu, C. & Webb, W.W. et al. 1996). 2 photon Microscope setup is similar to a confocal microscope because the scanning mechanism and lenses arrangement are almost similar, but with different lasers. Figure (1-2B) shows the main parts of a two photon microscope.

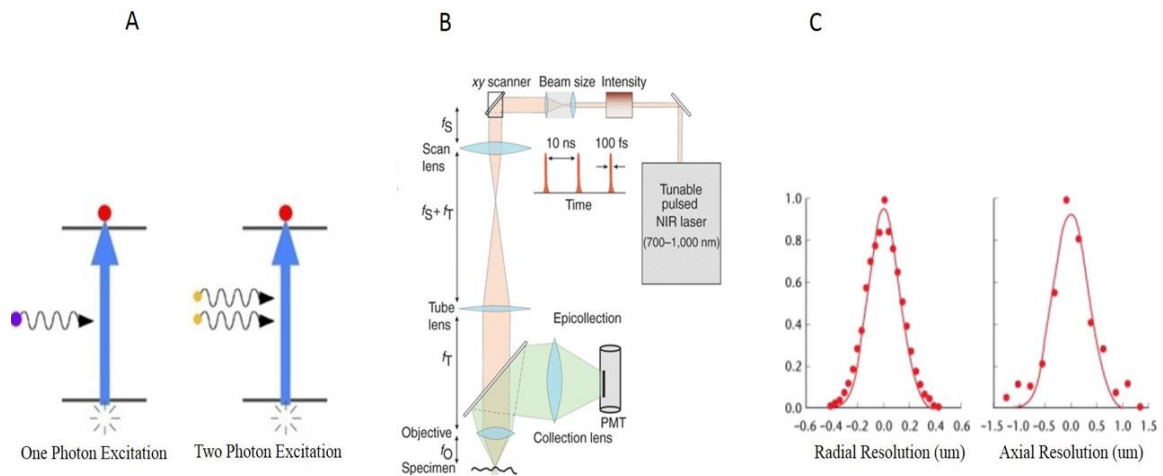


Figure (1-2). (A) Single Photon vs. Two Photon transition Mechanism. (B) Two Photon Microscope Setup (Fritjof Helmchen et al. 2005 Nature Methods). (C) Two Photon Resolution in Radial and Axial directions (<http://web.mit.edu/solab>)

Imaging depth is limited by some factors, one of them is laser output power which is (~1W) and wavelength because tissue scattering and absorption is depending on wavelength. Optimization of signal collection and detection is very important because scattering is more severe for shorter wavelengths, efficient fluorescence detection requires a large detection field of view even with a small imaged field of view (Mertz, J. & Charpak, S. et al. 2001, Beaurepaire, E. & Mertz, J. et al. 2002) and this in turn require special objective lens with high NA and low magnification. Also in vivo two-photon microscopy, photomultiplier tubes are used with large sensitive areas and high quantum efficiencies.

The ultimate imaging depth in two photon microscope is proportional to the scattering of laser wavelength and laser power, imaging depths is about 600–800 μm for 1 watt average power (Kleinfeld, D. & Tank, D.W. et al. 1997, Kerr, J.N. & Helmchen, F. at al

2004). For a deeper imaging area that is hard to reach by two photon microscope, it is possible to penetrate brain mechanically by using microprism or a small objective lens which is called gradient-index (GRIN) lens to relay image from deep image plane to microscope imaging plane (Jung, J. & Schnitzer, M. et al. 2003).

The image of any object is obtained by convolving the object intensity distribution with the point spread function (PSF). Point spread function of two-photon excitation has a full width at half-maximum (FWHM) of 0.3 μm in the radial direction and 0.9 μm in the axial direction by using 960 nm light wavelength and 1.25 NA objective lens (Sheppard and Kompfner, 1978, (Denk et al., 1990) (Figure 1-2BC).

Electrical recording (Electrophysiology) have been used for a long time to study neural activity with certain limitations compared to optical techniques. Electrophysiology techniques are recording from spatial dispersed neurons. On the other hand Two-photon microscopy could overcome those problems. Besides long wavelengths are less damaging and can penetrate deeper into tissue, and there is no out-of-focus light that affect imaging quality. Electrophysiology can detect signal with a very high temporal resolution on the sub-millisecond time scale. On the other side, two photon signal is limited by fluorophore kinetics and camera (CMOS camera), which operate around tens of milliseconds.

1.3.2. Wide Field Imaging:

The uses of wide-field fluorescence imaging microscopy to record neural activity in awake and freely moving mice started to emerge recently after all of the progress in

optoelectronics devices in term of quality, size and price. This miniature scope pioneered by Mark Schnitzer's Lab has a mass around 3 grams. The tiny microscope is based on the advancement in nanofabrication in semiconductors and optoelectronics, and it integrates all these parts in a tiny package. This microscope consists of a blue LED printed on a circuit board, a drum lens to collect the LED's emissions, excitation filter, dichroic mirror, a gradient refractive index (GRIN) objective lens, an emission filter and an achromatic doublet lens that focuses the image onto a CMOS sensor (640×480 pixels) mounted on printed circuit board.

The microscope housing is made from polymer materials. The field of view is $800 \mu\text{m} \times 600 \mu\text{m}$; the optical magnification is almost 5X; and the lateral resolution is almost $2.5 \mu\text{m}$. (Jung, J. & Schnitzer, M. et al. 2003, Wilt, B.A. et al. 2009, Tank, D. & Denk et al. 2001, Adelman, T.L. & Tank, D.W. 2007, Flusberg, B.A. et al. 2008, Sawinski, J. et al. 2009). This resolution is set by the limit of the camera's $5.6 \mu\text{m}$ pixel pitch, but the optical limit of the lens design is almost $1.5 \mu\text{m}$ resolution. The valuable part of this imaging technology is the ability to visualize an animal's brain over weeks, months, or longer, in freely moving animals. This scope can help understand neural circuit development and cellular changes in response to stimulus, as well as to study the brain for a prolonged period of time. The rapid progress in optoelectronics technology and semiconductors will open new horizon to improve optical imaging tool to be cheap, portable and easy to assemble in small labs (Figure 1-3).

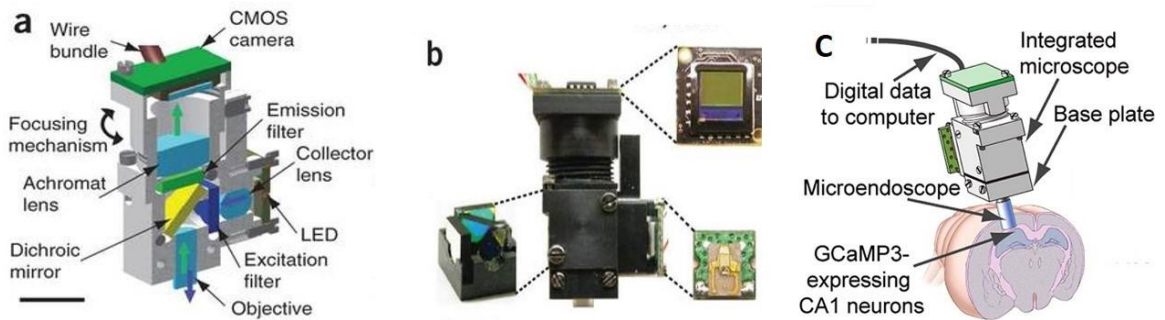


Figure (1-3). (A) Set Up and Components of Microendoscope. (B) Plastic Housing of Microendoscope. (C) Cartoon Picture show how to set up Microendoscope over Brain (Figure is adapted from Schnitzer, M. et al. 2003).

1.4 Hippocampus function:

The hippocampus is a fundamental component of the mammals' brains. It is part of the limbic system and plays important roles in memory and spatial navigation. The hippocampus is located beneath the cortical surface inside the medial temporal lobe. Damage to the hippocampus produces memory problems and could lead to amnesia (the inability to form or retain new memories). In rodents, hippocampus has been used as a neurological model to study brain as a system responsible for spatial memory and navigation. Hippocampus neurons respond to navigations through place cells, which fire bursts of action potentials when the animal passes through a specific place in environment. Place cells interact with others types of neurons as grid cells and other sensory neurons. On the other hand, long-term potentiation (LTP), which is a form of neural plasticity occurs in the hippocampus, is widely believed to be important for neural mechanisms by which memory is stored in the brain. Historically, hippocampal functions were related to inhibition, memory, and space. Behavioral inhibition theory is known as

“slam on the brakes!” (Nadel L, Black A. et al. 1975), which was proposed from behavioral observations after hippocampus damage such as hyperactivity in animal behavior and difficulty to inhibit responses that had been taught previously. Memory function is discovered accidentally from a surgical removal of the hippocampus in an attempt to cure epileptic seizures in a patient named Henry Molaison. The unexpected result of the surgery was amnesia: Henry Molaison was unable to form new episodic memories after surgery and could not remember new events, but he could retain memories for events happened years earlier such as his childhood. The hippocampal function was related to space and spatial navigation, as an essential discovery, which is proved experimentally by measuring action potentials from neurons while animals navigate in maze (O'Keefe, J; Nadel L. 1978).

Hippocampus role in spatial memory and navigation:

It is well known that Hippocampus is very essential in forming new memory and detecting places (Squire, LR, Schacter, DL, 2002, Ekstrom, AD, Fried, I, et al. 2003). Hippocampal damage leads to difficulty to form new memory, but older memory remain intact, which give rise to the concept that consolidation over time and long term memory storage occur outside hippocampus. On the other hand, hippocampus damage does not affect motor skills such as learning musical instrument or driving car, because it depends on different brain regions.

Hippocampus Place cells have been discovered when experiments were done in mice and rats moving in specific environment. Those neurons fire when animal pass through

certain place in its environment, this discovery led to the hippocampus might work as a cognitive map of environment. The hippocampus is mainly composed of pyramidal cells in a densely packed layer, and place cells are mainly represented by these pyramidal neurons. The adjacent place cells next to each other show uncorrelated spatial firing patterns, and also they are typically silent when a rat is moving around outside the place field, but can reach maximum rates when the animal is near the center. Also, the firing rate of place cells depends not only on place but also on the direction of moving animal (Moser, EI, Kropf, E, Moser, M-B, 2008). Figure (1-4) shows electrophysiology experiments that determined neural activity in pyramidal cells which is correlated with locations. Hippocampal place cells are using two types of inputs: path integration and sightings. The grid cell system provides path integration input, and lateral entorhinal cortex convey sensory information for “sighting”. The place cells combine both types of inputs to create a map to determine path and location.

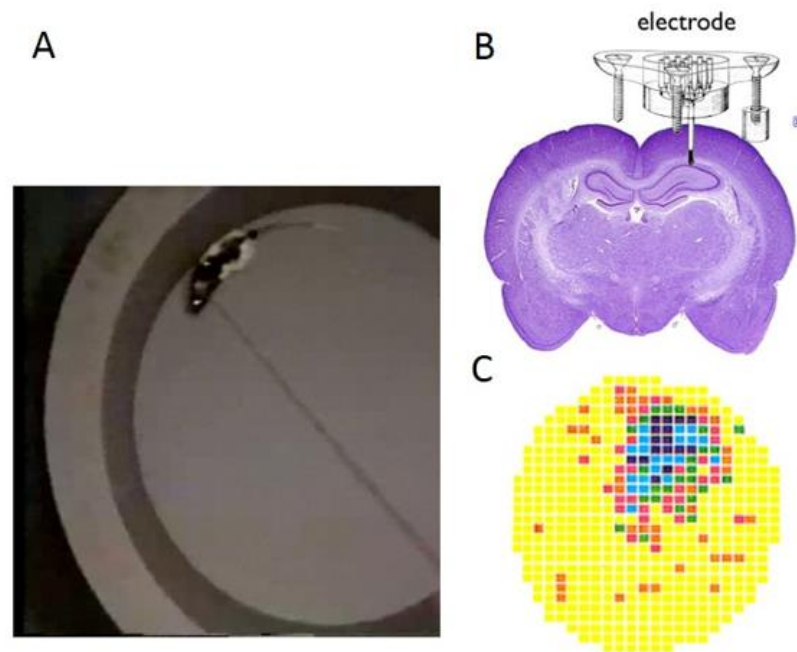


Figure (1-4) (A) Overhead Camera view of a rat in cylinder during recording, (B) Rat brain include hippocampus with Electrode, (C) place Cell firing rate map dark colors are pixel with high mean firing rates, yellow with zero firing rate. (Figure is adapted from Muller, et al., 1987).

Many studies have shown the role of hippocampus and its activation in organizing memories in the order of sequential events, and time stamp those events (Eichenbaum, H 2013). Associative memory and conditioning performance depend mainly on the temporal organization in hippocampus. In a classical trace conditioning experiment, a tone (Conditional Stimulus) is associated with Shock (Unconditional Stimulus) across a temporal gap, a central component of the time memory organization. It has been found that many neurons respond to Conditional Stimulus, and others respond to Unconditional Stimulus and when animal learn to associate the two stimuli. The hippocampus neurons play a role to estimate temporal separation between stimuli, which shows the importance of hippocampus in temporal dimensions of memory (Nguyen, N. & Fortin, N. J. et al.

2013). In this experiment, rats were trained to visually associate two different objects with two different cups of scented sand. Rats were first exposed to one object, and after a certain period of time, they were exposed to a cup with certain scent. If the scent and object match what animals were present it earlier, they need to dig in the sand for reward. During the delay time between the presentation of the object and the scented cup, different neurons fire at successive moments for the duration of this delay time (MacDonald, C. J., Eden, U. T. & Eichenbaum, H. et al. 2011). Another experiment is using two-photon calcium imaging in mice undergoing classical conditioning. Mice were presented with a tone for a short period of time, and then there was a temporal gap followed by an air puff to the eye. CA1 neurons response shows time-locked firing sequences throughout the temporal gap. This demonstrates that CA1 neurons encode temporal structure, and it is not relating to place cell ideas (Modi, M. N., Dhawale, A. K. & Bhalla, U. S. et al. 2014).

Hippocampus waves and Formation:

Theta rhythm in the hippocampus is a type of wave generated at 3–10 Hz. This wave strongly modulates the spiking of hippocampal neurons and synchronizes across the hippocampus in a travelling wave pattern. Theta wave appears during REM sleep, when an animal is walking and interacting with its surroundings, and it is relating to learning and memory. The phase of theta wave is very important for learning and memory at the time of neural stimulation (Huerta PT, Lisman JE, 1993). Medial septum area is considered the main source of theta wave and lesion of this area severely deteriorate

memory and learning in animal (Amaral, D, Lavenex P. 2006). Sharp waves appear during sleep, or during animal resting. These waves are associated with bursts of spike activity and associated also with high-frequency called "ripples", with frequencies in the range 150–200 Hz. The function of sharp wave was proposed as a neural pattern reactivations of memories stored in hippocampus during behavior, which is important to transfer stored memories from hippocampus to neocortex during sleep (Sutherland GR, McNaughton B. 2000).

Long-term potentiation (LTP) is a characteristic feature and fingerprint of hippocampus. Through LTP, brain stores memory by changing the synapses connections between neurons which is participating in behavior paradigm, this idea was proposed by Donald Hebb in 1948. This effect happens through changing synaptic responsiveness induced by consistent neural activation, which is lasting for hours or days. LTP occurs at synapses terminals which changes depend on a special type of glutamate receptor called NMDA receptor, which allows calcium to enter the postsynaptic spine when presynaptic get activation in the same time with postsynaptic. Drugs that block with NMDA receptors have major effects on memory and learning (Bliss T, Lømo T. 1973).

Information Flow in the Hippocampal Formation: The excitatory trisynaptic pathway in hippocampus (entorhinal cortex (EC)–dentate gyrus (DG) – CA3 – CA1– EC) is illustrated in figure (1-5). Layer II neurons in the entorhinal cortex (EC) send projection to the dentate gyrus and CA3 through the perforant pathway (PP) and layer III neurons in EC send projection to CA1.

The dentate gyrus (DG) sends projections to the pyramidal cells in CA3 and CA1 through mossy fiber and Schaffer collaterals respectively. CA1 pyramidal neurons send back-projections into layer V and VI neurons of the EC. Figure (1-5) Illustration Cartoon of hippocampus Circuitry (Javier DeFelipe et al. 2014).

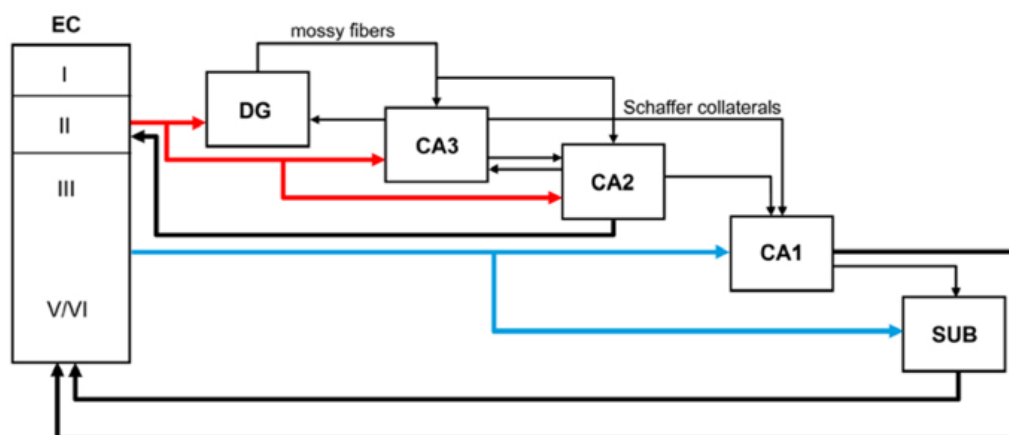


Figure (1-5) Illustration Cartoon of hippocampus Circuitry (Adapted from M. L. Martín et al. Front. Neuroanat., 2014).

1.5 Blast Injury to The Brain:

Blast Injury lead mechanical stress to brain tissue, which can lead to disability and many other mental and behavioral problems depending on the severity of injury. Its impact could last for a long time and affecting memory, movement, vision, hearing, epilepsy and depression. Blast Injury cost annually an estimated \$76 billion. Seatbelts and helmets have reduced the effect of Blast Injury consequences substantially. However, there are many unanswered questions regarding the impact of Blast Injury on brain, and how brain responds to it and how it may be treated. Blast Injury is caused by an external force that produces movement of the brain within the skull. Causes include falls, motor vehicle crashes, and sports injuries. Blast Injury can range from mild which is affecting

consciousness for a short period of time, to severe which extends to a longer period of time and many other consequences.

During the movement of the skull through space by acceleration or deceleration, the brain moves inside the skull. Because the skull is hard and inflexible while the brain is soft, this gives rise to brain moves at a different rate than the skull. In addition, different parts of the brain move at different speeds which alternately compress and stretch brain tissue when it is exposed to sudden movement inside the skull. If the impact is strong enough, axons can be stretched. This might lead to brain injury and neuron death. Understanding the multidimensional cascade of injury could thus offer therapeutic options (Lee E. Goldstein et al. 2012).

Neuroimaging of Blast Injury which lead to TBI:

There are structural and functional imaging techniques for Blast Injury research clinical studies, such as Computed tomography (CT) for clinical quantifications of Blast Injury. CT is an imaging technique that uses x-ray to create detailed pictures of areas inside the body. CT was used to investigate abnormalities arising from Blast Injury. Also, CT is highly effective in detecting bleeding (hematomas) as well as brain swelling (edema) which is very important for emergency cases to determine with surgery is required or not. Magnetic resonance imaging (MRI) is another powerful technique that can detect micro bleeding (microhemorrhage), small areas of bruising (contusion) or scarring (gliosis), which are invisible to the CT scan (Figure 1-6). On the other hand, MRI could also be used to link tasks to brain activity to get connectivity maps between neural regions. Both

techniques have been used to detect consequences of Blast Injury over the years (Lystad RP., Pollard H. 2009). Neuropathological damage is often evaluated histologically by using bio markers and imaging techniques and behavior test to evaluate brain resilience Fig (1-7) (Bigler ED. 2013). Table (1-2) shows the difference between different types of imaging techniques.

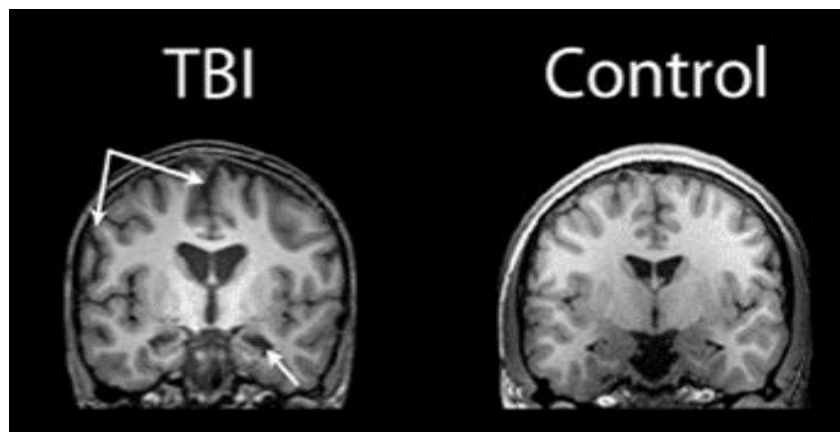


Figure (1-6) T1-weighted coronal images of a TBI patient on the left and an age-matched control on the right, both young adolescent males. Arrows point to a prominent interhemispheric fissure and cortical sulci (Adapted from Bigler ED. 2013).

Mental fatigue and cognitive functions:

TBI can be quantified through measuring mental fatigue and cognitive reserve. Cognitive reserve describes the brain resistance to damage. Mental fatigue occurs after both mild TBI as well as moderate to severe TBI. It is characterized by reduction mental activity and mental exhaustion. The main symptoms of mental fatigue include: mental exhaustion already after ordinary activities, long mental recovery, distinct 24h variation. Mental fatigue affects cognitive functions after TBI which correlates to poor performance in cognitive task (Belmont, Agar, & Azouvi, 2009). Also it has been reported to correlate to

processing speed and attention, (Johansson, Berglund, & Rönnbäck, 2009). Reduction in cognitive capacity could be compensated by increase mental effort due to impaired neural network, which in turn lead to increase in mental fatigue (Zomeran & van den Burg, 1985) due to recruitment of brain areas outside the working memory network. This effect has been measured using functional Magnetic Resonance Imaging (fMRI) (Kohl, Wylie, Genova, Hillary, & Deluca, 2009).

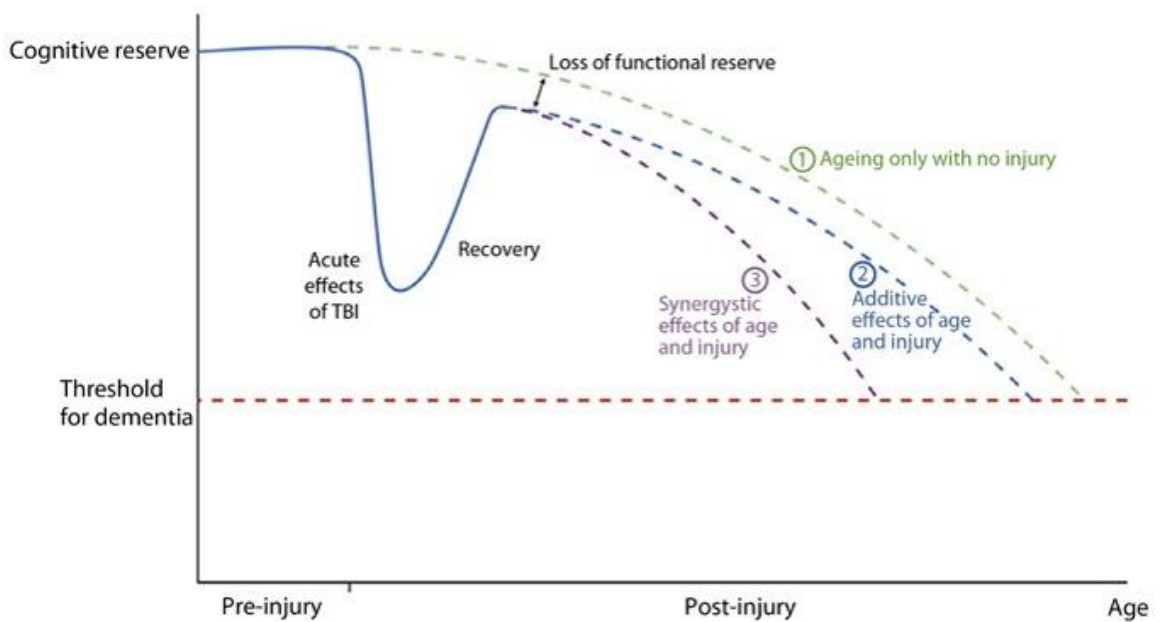


Figure (1-7). A graphical representation of a postulated cognitive reserve and how head injury may increase the risk of cognitive decline (Bigler ED. 2013).

Table (1-2) Comparison of Imaging Technique used in Brain Studies (Lystad RP, Pollard H, 2009)

	PET	SPECT	fMRI	EEG	MEG
Measure of neural activity (Biological Process measured)	indirect haemodynamic response	indirect haemodynamic response	indirect haemodynamic response	direct neuroelectrical potentials	direct neuromagnetic field
Invasiveness	invasive	invasive	non-invasive	non-invasive	non-invasive
Temporal resolution	poor (1–2 min)	poor (5–9 min)	reasonable (4–5 s)	excellent (<1 ms)	excellent (<1 ms)
Spatial resolution	good/excellent (4 mm)	good (6 mm)	excellent (2 mm)	reasonable/good (10 mm)	good/excellent (5 mm)

1.6 Parkinson Disease and Basal Ganglia:

Parkinson's disease (PD) affects millions of people in the world today, and many more will likely be diagnosed as the population ages. PD is characterized by the loss of midbrain dopamine innervation to the basal ganglia, resulting in an array of motor impairments, including akinesia, bradykinesia, rigidity, and tremor, as well as cognitive deficits. As the disease progresses and increasing numbers of dopamine neurons die, the motor and cognitive deficits become worse. Treatment with a dopamine precursor (levodopa) is successful but results in dyskinesia after several years of treatment. Deep brain stimulation (DBS) of the subthalamic nucleus (STN) is effective for treating motor symptoms in patients with severe PD, but not much is understood about the mechanism behind its success (Eusebio, A., and Brown, P., et al. 2012). A characteristic of PD patients is the presence of pathological beta band oscillations (10–30Hz) recorded from motor areas of the brain. These beta oscillations are correlated with motor deficits and are

reduced with either pharmacological treatment or DBS (Priori et al., 2004, Brown et al., 2004, Silberstein et al., 2005). Furthermore, data suggest that abnormally enhanced beta oscillations may result in features of PD such as bradykinesia (Brown, 2007, Hammond et al., 2007).

The source of pathological beta oscillations in Parkinson's disease is not currently known; however, several theories exist. One hypothesis that is widely cited proposes that the recurrent connections between the STN and the external globus pallidus (GPe) form a pacemaker that independently generates oscillatory activity (Bevan et al., 2002, Plenz and Kital, 1999). A second hypothesis proposes that cortical patterning of the STN and GPe, dependent on cortical slow-wave activity, generates beta oscillations in the dopamine-depleted state (Bevan et al., 2002, Magill et al., 2001). A third, recently proposed theory from our labs suggests that beta oscillations can originate from striatal dynamics (McCarthy et al., 2011). In the striatum, dopamine modulates the release of acetylcholine (ACh) by cholinergic interneurons (DeBoer et al., 1996). However, dopamine is depleted in the Parkinsonian state, leading to abnormally high levels of ACh in the striatum (Ikarashi et al., 1997). Acetylcholine in the striatum activates muscarinic M1 receptors (Kreitzer, 2009), decreasing M-current activation in the medium spiny neurons (MSNs) of the striatum, increasing MSN excitability (Shen et al., 2005) and enhancing beta frequency oscillations. Furthermore, the infusion of carbachol, an acetylcholine agonist, into the striatum resulted in increased beta oscillations (McCarthy et al., 2011), supporting the idea that increased cholinergic tone in the striatum may be a source of enhanced beta oscillations in PD. Although the striatum is the main target of the

dopaminergic neurons that degenerate in PD, the striatum is connected in a loop with the rest of the basal ganglia, the thalamus and the cortex. Parkinsonian symptoms are thought to result from the impact of altered striatal output on network dynamics throughout the CBT loop. Beta oscillations (8–30 Hz) have been observed throughout the CBT loop, are prominent in the Parkinsonian state and are both modulated by movement and decreased by dopaminergic drugs and DBS. Sub-divisions of the beta frequency band correlate with different symptoms in Parkinson's disease: low beta (~13–20 Hz) is correlated with bradykinesia and rigidity, and high beta (~20–30 Hz) is correlated with freezing of gait. The source of these beta oscillations is unknown. Previous studies have suggested pathologic beta oscillations may arise from reciprocal connections between GPe and STN, from motor cortex (Yamawaki, N., et al. 2008), or from striatum (Damodaran, S., et al. 2015, McCarthy, M.M., et al. 2011).

CHAPTER TWO: Methods

2.1 Animal Preparation for surgery:

Putting animal under isoflurane is considered as a standard technique of general anesthesia for rats and mice used in biomedical research. Mice were placed on Stereotaxic with thermal pad adjusted to 37 C, Stereotaxic is used to manipulate and target discrete regions of mice brain. Stereotaxy is locating the targeted region of the brain on a three dimensional axis. To determine the location of a region of interest for surgical purpose, a brain atlas is used and spatial coordinates are expressed using a set of 3 axes: Anterior-posterior, medial-lateral and dorsal-ventral. Skull landmarks which are formed by bone plate intersections are used for coordinate measurement. The most prominent landmark is bregma which is defined as the point of intersection of the sagittal suture with the coronal suture. The second point is lambda which is more posterior and formed by intersection of sagittal suture with the lambdoid suture. The probe holder and micromanipulator, which is attached to the mounting clamp is used to determine location precisely and precise movement of surgical probes. Ear bars hold the head in a fixed position.

Equipment required to achieve this procedure

1. Isoflurane vaporizer Supply gas (oxygen)
2. Supply gas regulator Flowmeter (0–1000 ml/min)
3. Connection tubing and valves Facemask
4. Stereotaxic apparatus (e.g. KOPF) (Figure 2-1A)
5. Stereomicroscope (e.g. Leica M80)

6. Scalpel blade and handle
7. Scissors

Surgical standard preparations are going as fellow

1. The ear bars are gently placed in the ears and the front teeth are placed in the incisor bars (Figure 2-1B).
2. Eye ointment is used on mice eye to prevent corneal drying during surgery.
3. the scalp of an anesthetized animal is shaved and disinfected
4. clean the surface of the skull
5. use the micromanipulator to determine bregma and lambda and adjust level between them to be exactly equal or with less than 0.1 mm difference
6. use brain atlas to know coordinate and move our probe from bregma to the target position
7. Under the skull you will find the dura, a thick membrane tissue that can be removed by using tip of a small needle.

Viral Injection

All animal procedures were approved by the Boston University Institutional Animal Care and Use Committee, and the methods were carried out in accordance with the approved guidelines. Female C57BL/6 mice, 8–12 week old at the start of the experiments, were used in all studies (Taconic; Hudson, NY). Mice were first injected with AAV9-Syn GCaMP6f.WPRE.SV40 virus obtained from the University of Pennsylvania Vector Core (titer $\sim 6 \times 10^{12}$ GC/ml). 250 nL of virus was stereotaxically injected into the CA1 region (AP: -2 mm, ML: 1.4 mm, DV: -1.6 mm) using a 10 μ L syringe (World Precision

Instruments, Sarasota, FL) fitted with a 33 gauge needle (NF33BL; World Precision Instruments, Sarasota, FL), at a speed of 40 nl/min controlled via a microsyringe pump (UltraMicroPump3-4; World Precision Instruments, Sarasota, FL). Figure (2-1C) depict the injection location in Hippocampus.

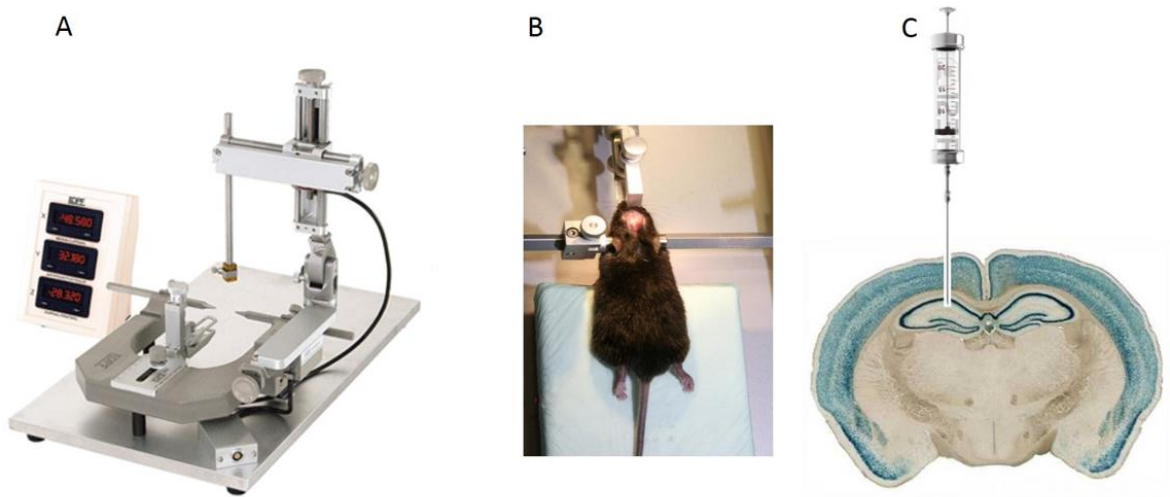


Figure (2-1). (A) Stereotaxic apparatus, (B) Positioning Mice in Stereotaxic apparatus, (C) Cartoon Picture Showing the injection process and location of injection.

Standard Method for Viral Injection:

- 1- Check out the amount of gas and Isoflurane to make sure it is enough for running this surgery.
- 2- Turn on gas tank and regulators.
- 3- Turn on flowmeter between 600 ml/min.
- 4- Turn on vaporizer to 2 %.
- 5- Place mice in induction tube for 3 mins before transferring it to Stereotaxic tube till animal completely sleep.

- 6- Switch system to flow to Stereotaxic nozzle.
- 10- Monitor mice respiration and response to stimulation to adjust vaporizer as needed
- 11- Use scissor to open skin over skull
- 12- Fill syringe with virus (1 ul)
- 13- Determine the coordinate of injection and position needle over the target place,
- 14- Use microsyringe pump controller to inject virus (injection rate 40 nl/min)
- 15- After injection and before pulling needle out of brain, leave needle inside brain for 10 mins to make sure that all virus diffuse in brain tissue.
- 16- At completion of procedure, turn vaporizer off and allow animal to breathe supply gas until it begins to awaken.
- 17- Place animal in recovery area with thermal support until fully recovered.

2.2 Custom Fabrication of Cannula, Animal Holders:

Head plate holder is a piece of metal with (1 mm thickness, 3 cm length) which is fabricated in Boston University machine shop. (Figure 2-2A).

Mice holder is a plastic holder designed and fabricated using 3D printer to fit mice size and provide a tide place to reduce mice movements (Figure 2-2B).

Custom imaging windows (Cannulas) are fabricated in EPIC, Boston University, College of engineering, This Cannula made from a stainless steel tube (OD: 3.17 mm, ID: 2.36 mm, height, 2 mm) then putting this metal tube in acetone for a day to remove debris then

use 70% Alcohol for extra cleaning. Afterward metal tube get ready to be adhered to a circular coverslip (size 0; OD: 3 mm) using a UV-curable optical adhesive (Norland Products) and UV lamp working at wavelength 360–420 nm for 3 mins (Figure 2-2C).

Implanting Window (Cannula):

Upon complete recovery which is taking 1 week, animals were surgically implanted with custom imaging windows. After careful aspiration of the overlying cortical tissue, using the corpus callosum as an anatomical guide, the imaging window was placed above the CA1 viral injection site. During the same surgery, a custom aluminum head-plate was attached to the skull anterior to the imaging cannula.

The procedure for implanting a cannula for chronic *in vivo* brain imaging using wide field microscopy and mice preparations. This process starts after 1–2 weeks from viral injection. We are using the same tools that is mention in viral injection part plus extra equipment that will be mention in this section.



Figure (2-2). (A) Cartoon picture showing Mice Holder, (B) Head Plate, (C) Optical window (Cannula).

Equipment and setup:

1. Cannula, for implantation (3 mm outer diameter)
2. Kwik-Sil (Silicone Elastomer) – (World Precision Instrument)
3. Micro drill (Lynx™ 333 Standard High Speed – 4-Hole)
4. Dental Carbide Burs (Round)
5. Surgical setup & Anesthesia system for mice (Mentioned in viral injection part)
6. Surgical tools and instruments (e.g. Fine Science Tools)
7. C&B Metabond
8. Amalgambond Metabond Catalyst
9. Clear L-Poweder for C&B Metabond
10. Distilled water, sterile, for rinsing cannula
11. Ethanol, 70%,
12. Needle tips, ½”, blunt, 27- and 30-gauge
13. Ophthalmic ointment
14. PBS
15. Skin disinfectant, e.g. betadine, iodine
16. Vacuum line for tissue aspiration, custom-made
 - Access to vacuum line
 - Glass vacuum flask
 - Tubing and fittings

Procedure:

1. Anesthetize mouse using isoflurane.
2. Position the animal in the stereotaxic frame and maintain the animal's body temperature at 37 °C with heat pad.
3. Put ophthalmic ointment on the eyes of mice.
4. Remove the fur from mice head, and disinfect the area with alternating washes of 70% ethanol and betadine.
5. Expose the surface of the skull by using skin scissors to remove part of skull skin.
6. Using Hydrogen Peroxide to clean skull surface to remove connective tissue then dry out skull surface.
7. Open a round craniotomy around coordinates of interest area using the micro-Dental drill (3 mm).
8. Use forceps to remove dura and keep exposed brain moist all the time by using ACSF or Saline.
9. Start aspiration with a 27-G blunt needle tip attached to the suction line, this is the most important step and we should do it slowly and trying to avoid and stop bleeding all the time and keep area clear.
10. Monitor visual landmark for target structure. In targeting hippocampal area CA1, stop after passing through the corpus callosum.
11. After reaching the target depth, we trying to control bleeding from the sides and bottom of the aspirated area by flashing ACSF or Saline and leave it for some seconds then suck it again gently and repeat this many times.

12. Once bleeding has been stopped, Fill the area with saline and leave it for a while to make sure that no bleeding will come over again.
13. Place cannula gently into the craniotomy. Do not put any pressure once cannula touch tissue.
14. Fill the gap between cannula and brain tissue with Kwik-Sil (small drop) and wait till it solidify.
15. Ensure that the skull is dry. Apply a thin layer of metabond to the skull and the edges of the skin surrounding the tissue.
16. Using 3 screws (000x3/32 flat screws F000ce094) over different area of skull to make sure that dental metabond will stay stable over long period of time.
17. Apply a layer of dental metabond over the exposed skull, and sidewalls of the cannula.
18. Put a piece of adhesive dressing over the cannula to prevent dust and dirt from going inside cannula while the animal is in the home cage.
19. Allow the animal to recover from anesthesia and return it to home cage.

2.3 Animal Behavior Protocol:

In this study, classical conditioning paradigm (Trace condition) has been used which is important to study neural substrates of associative learning. In this paradigm we are pairing two stimulus, conditional stimulus (CS) and unconditional stimulus (US).

Trial Configuration. Individual trials consisted of a 350 ms, 9500 Hz pure tone (CS), digitized at 100 kHz with a 5 ms cosine ramp, delivered at 80 dB SPL. The tone was

followed by a 250 ms trace interval and then a 100 ms long 5psi air puff (US) (Figure 2-3) controlled via a solenoid (Clippard EV-2, Cincinnati, OH) and delivered through a 0.5 mm cannula positioned 2–3 cm away from the right eye. Trials occurred randomly with an inter-trial interval of 31–36 seconds.

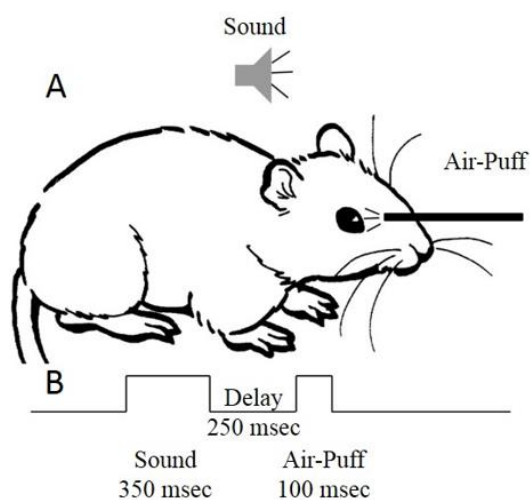


Figure (2-3). (A) Cartoon Picture shows Behavior Task, (B) Behavior Task Protocol

Animal Training

Mice were trained to criterion on a conditioned trace eye-blink task. Training was modified slightly from other previously published paradigms (Disterhoft, J. F. & Weiss, C. et al. 2004; Modi, M. N., Dhawale, A. K. & Bhalla, U. S. 2014). Briefly, animals were allowed to completely recover from surgery (typically about 4 weeks) before being handled and habituated to the training apparatus for 3 consecutive days. During habituation and training, animals were head fixed to custom holder that consisted of a 34 mm diameter aluminum half-tube that supported the animal and allowed for attachment of the head-plate at the anterior end. Animals were covered on top by an elastic wrap that

reduced upward movement out of the half-tube. Habituation occurred at the same time as subsequent training (4–8 hours after lights-on). Following the habituation period, animals began training on the conditioned eye-blink task. With the exception of the first day of training, mice were trained in two blocks of 40 trials each. On the first day of training animals received 20 sound alone trials to determine a baseline level of eye-blink response for the tone prior to any tone-puff pairing. Subsequent training (days 2–5) consisted of 2 blocks of tone-puff training. A single 40 trial block took approximately 25 minutes. Animals were then given a 10–15 minute rest period before being trained on the second block. Prior to the training session animals were positioned underneath the CMOS camera and had the air-puff tube and a USB3.0 camera oriented for air puff delivery and eye movement capture, respectively. A custom MATLAB script controlled the behavioral stimuli and image capture timing using TTLs delivered via a I/O interface (USB-6259; National Instruments, Austin, TX). Image capture for both cameras were time locked to each other and sampling occurred at 20 Hz. Exposure time was fixed at 35 ms. Eyelid position was monitored using Point Grey Fly Capture 2 software and Flea3 USB3.0 camera (FL3-U3- 13S2C-CS; Richmond, BC, Canada). Eyelid position was calculated by converting the area of the eye into a region of interest using ImageJ (NIH; <http://imagej.nih.gov/ij/>). The eye and surrounding area was illuminated using an IR lamp positioned approximately 0.5 meters away. Using this configuration, eye lid area can be recorded as an increase in reflection that occurs as the eyelid closes impinging on the defined eye ROI.

2.4 Wide Field fluorescence Imaging Setup:

The development in optical microscopy components as detectors, camera and lens technologies give rise to a progress in biological optical imaging. Custom wide field optical microscope has been built in our lab. This microscope has many advantages such as it is cheap, could be built easily in any lab, provide large field of view and relative higher resolution than regular wide field microscope.

Components:

CMOS camera (ORCA-Flash4.0 LT Digital CMOS camera C11440-42U; Hamamatsu, Boston, MA). It has 2 times the speed, 3 times the field of view (Figure 2-4B) and up to 5 times the signal to noise over even the best interline CCD cameras (Figure 2-4B), the following figure show that. (Figures 2-4) show the advantages of this camera over classical CCD camera. Fluorescence excitation is accomplished with a 5W LED (LZ1-00B200, 460 nm; Led Engin, San Jose CA). Image optics included a Leica N Plan 10 × 0.25 PH1 microscope objective lens, an excitation filter (HQ 470/50), dichroic mirror (FF506-Di02), emission filter (FF01-536/40), and a commercial SLR lens focused to infinity as the tube lens (Nikon Zoom-NIKKOR 80–200 mm f/4 AI-s). Hippocampal imaging data were collected and processed using a computer equipped with dual Intel Xeon processors, 128 GB RAM, and a GeForce GTX Titan video card. The use of the graphics card allowed for images to be processed offline by the GPU and therefore did not dependent on substantial amounts of available computer RAM. Images were captured as multi-page tagged image file format (mpTIFF's) using the default image-capture software bundled with the purchase of a sCMOS camera from Hamamatsu (HC Image

Live; Hamamatsu; Boston, MA). Table (2-1) shows camera specifications.

Table (2-1) camera specifications.

Effective no. of pixels	2048 (H)×2048 (V)
Cell size	6.5 μm×6.5 μm
Effective area	13.312 mm×13.312 mm
Readout speed	30 frames/s (Full resolution)

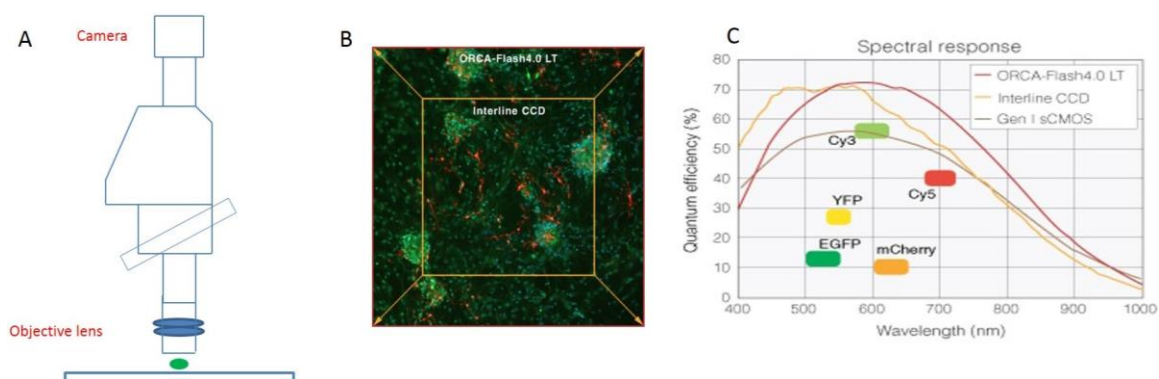


Figure (2-4). (A) Microscope Sketch, (B) The ORCA-Flash4.0 LT provides 3 times larger field of view compared to commonly used interline CCDs, (C) Excellent imaging quality (high quantum efficiency) (www.hamamatsu.com).

Calculation of Microscope Optical Resolution:

The microscope resolution limit refers to its ability to differentiate between two closely spaced Airy disks in the diffraction pattern, equation (1) describes the optical resolution limit for optical microscope.

$$\text{Objective Optical Resolution (R)} = \lambda / 2 \cdot \text{NA} \quad (1)$$

Where NA is a general term for the microscope numerical aperture and λ is imaging wavelength.

But total system resolution depends not only on Objective optical resolution but also on camera resolution, which is dependent mainly on pixel size.

$$\text{Camera Resolution (C)} = 2 \times \text{Pixel Size} \quad (2)$$

$$\text{System Resolution (S)} = C / M \quad (3)$$

Where M is Objective lens Magnification.

Calculating the Image size on Camera and pixel sizes on images

$$\text{Image Size on Camera} = R \times M \quad (4)$$

$$\text{Image pixel size} = \text{camera pixel size} / M \quad (5)$$

Calculating Field of View:

$$\text{Field of View (Camera– Objective)} = \frac{\text{Camera Sensor Size}}{\text{Objective lens magnification}} \text{ (mm)} \quad (6)$$

$$\text{Field of View (Eyepiece – Objective)} = \frac{\text{Eyepiece Field Number}}{\text{Objective lens magnification}} \text{ (mm)} \quad (7)$$

2.5 Image Processing:

Image processing was performed offline using MATLAB software package developed in Han Lab, Boston University. The goal of this procedure was to reduce the raw image sequence to a collection of one-dimensional traces, where each trace indicates the fluorescence intensity of an individual neuron over time, and the collection approximates the distinct activity of each and every neuron in the imaging field of view. The process was implemented in 3 distinct stages (Figure 2-5) as described below.

Image Pre-processing:

A- Contrast Enhancement and Motion Correction:

Alignment of each frame in the image sequence with all other frames is essential to the methods we use in subsequent steps for identifying and tracking pixels over time. Thus, the goal of the first stage is to correct for any misalignment caused by movement of the brain tissue relative to the microscope and camera. We preceded our main motion correction procedure with a contrast enhancement step that attempts to mitigate the effect of any non-uniform illumination of the brain tissue.

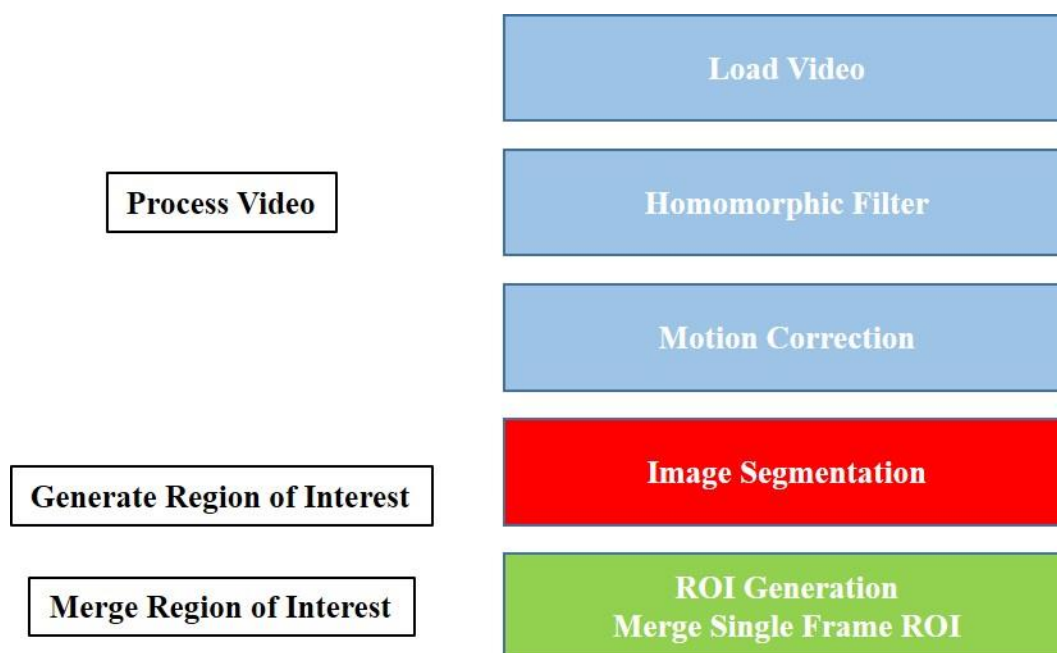


Figure (2-5). The process of image processing

Any illumination non-uniformity will be stationary in the camera's field of view despite motion of the illuminated brain, which would hamper motion detection, or alternatively produce artifacts in correctly motion-corrected frames if left uncorrected. This

enhancement is essentially a high-pass filtering operation, however the filtering must be performed in the log domain because of the multiplicative nature of light absorption. Additionally, artifacts often associated with digital high-pass filtering can be mitigated by equivalently computing a low-pass filtered component of each frame, then subtracting the low-pass component from the original image. This log-domain filtering operation is often described as “Homomorphic filtering” (see for an example; <http://blogs.mathworks.com/steve/2013/06/25/homomorphic-filtering-part-1/>). Many algorithms for estimating and correcting image displacement exist and are well described in the medical imaging literature. We elected to use phase-correlation to estimate the induced motion in each frame, as we found this method to be highly stable, moderately accurate, and most importantly, fast, especially when implemented in the frequency domain and using a quality graphics card. The operation estimates the mean translational displacement between two frames, one being the template or “fixed” frame, and the other being the uncorrected or “moving” frame. In the spatial domain this is accomplished by computing the normalized cross-correlation, which implies a 2-dimensional convolution of large matrices. The equivalent operation in the frequency domain is a simple scalar dot-product of the discrete Fourier transforms of each image normalized by the square of the template, followed by the inverse Fourier transform. The intermediate result is the cross-correlation (or phase-correlation) matrix, which should have a peak in its center for correctly aligned images, or a peak near the center, the offset of which indicates the mean offset between the two images. This peak can be found with subpixel precision by interpolation to give a more accurate alignment, although at some moderate expense in

computation time. For the template image we used a moving average of previously aligned frames when processing frames sequentially, which was averaged with a fixed mean of randomly sampled and sequentially aligned images from the entire set when processing files in parallel. The simplest way to perform this operation is to use the built-in MATLAB function *normxcorr2*, which makes optimization decisions based on image size and available hardware automatically. However, performance can be improved by tailoring the operation to your particular hardware and image size, i.e. using *fft2* and *ifft2* for large images and a good graphics card. Additional details of this procedure are well documented in the literature, as well as in the example functions provided at the following URL: <http://www.bu.edu/hanlab/resources/>. Shifting and interpolation are also covered in our MATLAB documentation and examples. After aligning sequential image frames, we were able to estimate a baseline value and other statistics for each pixel (maximum, minimum, mean, standard-deviation, etc.), and use these statistics to reduce the bit-depth of frames being passed to the next stage. This was done purely to speed computation in subsequent steps, but won't necessarily be helpful in all cases. For the results presented here, the motion-corrected images were saved as a new video file with 8 bit dynamic range, with the top 1% intensity saturated at 255 and the bottom 1% set at 0.

B-Region of Interest (ROI) detection:

The ROI detection process used an adaptive threshold on the z-score of pixel intensity to reduce each frame to binary 1's and 0's (logical true or false). These binary frames were then processed using morphological operations to find and label connected components

within each frame. For example, beginning with a z-score threshold of 1.5, all pixels that were more than 1.5 standard deviations above their mean were reduced to 1 (true), and all others reduced to 0 (false). Pixels reduced to 1 were often pixels overlying a cell that was significantly brighter during that frame due to activation of GCaMP. This initial threshold was adjusted up or down based on the number of non-zero pixels detected with each threshold. This was done to prevent spurious motion-induced shifts of the image frame from producing ROIs along high contrast borders. All morphological operations were performed using built-in MATLAB functions from the Image Processing Toolbox, which have fast parallel versions if the operation is run on a graphics card (e.g. *imclose*, *imopen*, etc.). Furthermore, the connected-component labeling and region formation operations were run using built-in MATLAB functions *bwconncomp*, and *regionprops*. Connected components were stored in a custom class and termed “single-frame ROIs,” and these were then passed to the 3rd stage of processing, which merges them into a “multi-frame ROI” that represents the location and spatial distribution of each cell identified over the entire video.

C-Region of Interest (ROI) merging:

The standard structure of region properties output by the MATLAB function *regionprops* (Area, BoundingBox, Centroid, etc.) are mimicked in a custom function called *RegionOfInterest*, where each field of the structure becomes a property of the custom class. We added additional properties for storing state information and data associated with each ROI, along with a number of methods for comparing, merging, manipulating,

and visualizing the single-frame and multi-frame ROIs. The single-frame to multi-frame ROI merging procedure is essentially a clustering process that merges single-frame ROIs together using such criteria as the proximity of their centroids, as well as proximity of their bounding-box (upper-left and lower-right corners). Performing this operation quickly was highly dependent on pre-grouping ROIs based on centroid location in overlapping blocks of the image frame, as well as grouping by size. This enabled the clustering to be performed in parallel (across CPU cores) followed by a second iteration of clustering to deal with redundancy in overlapping regions. Once ROIs are established, all video data is reloaded and passed to a method in the *RegionOfInterest* class that extracts the 1-dimensional trace for each ROI representing the fluorescence intensity in that region over time. The ROIs and their traces can then be quickly visualized using another method in the *RegionOfInterest* class, which relies on the *distinguishable_colors* function, available on the Mathworks File Exchange (http://www.mathworks.com/matlabcentral/fileexchange/29702-generate-maximally-perceptually-distinct-colors/all_files).

2.6 Blast Wave Measurements, Calibration and Procedure:

A precision dynamic high frequency piezoelectric pressure transducer (Model: 113B21 High Frequency ICP® pressure sensor, PCB Piezotronics, Inc., Depew, New York) is used to record blast waves produced by the Cranium Only Blast Injury Apparatus (COBIA). The sensor is positioned where the head of the mouse would be inside the apparatus. A constant current supply (Model 5421, Columbia Research Laboratories, Inc.

Woodlyn, PA) provides power to the transducer with a conversion constant 3612 mV/MPa. Outputs are digitized using an A to D converter (National Instruments, NI USB-6259) before saving waveforms for offline analysis. This setup produced non-lethal blast overpressures of approximately 1307 kPa (Figure 2-6B).

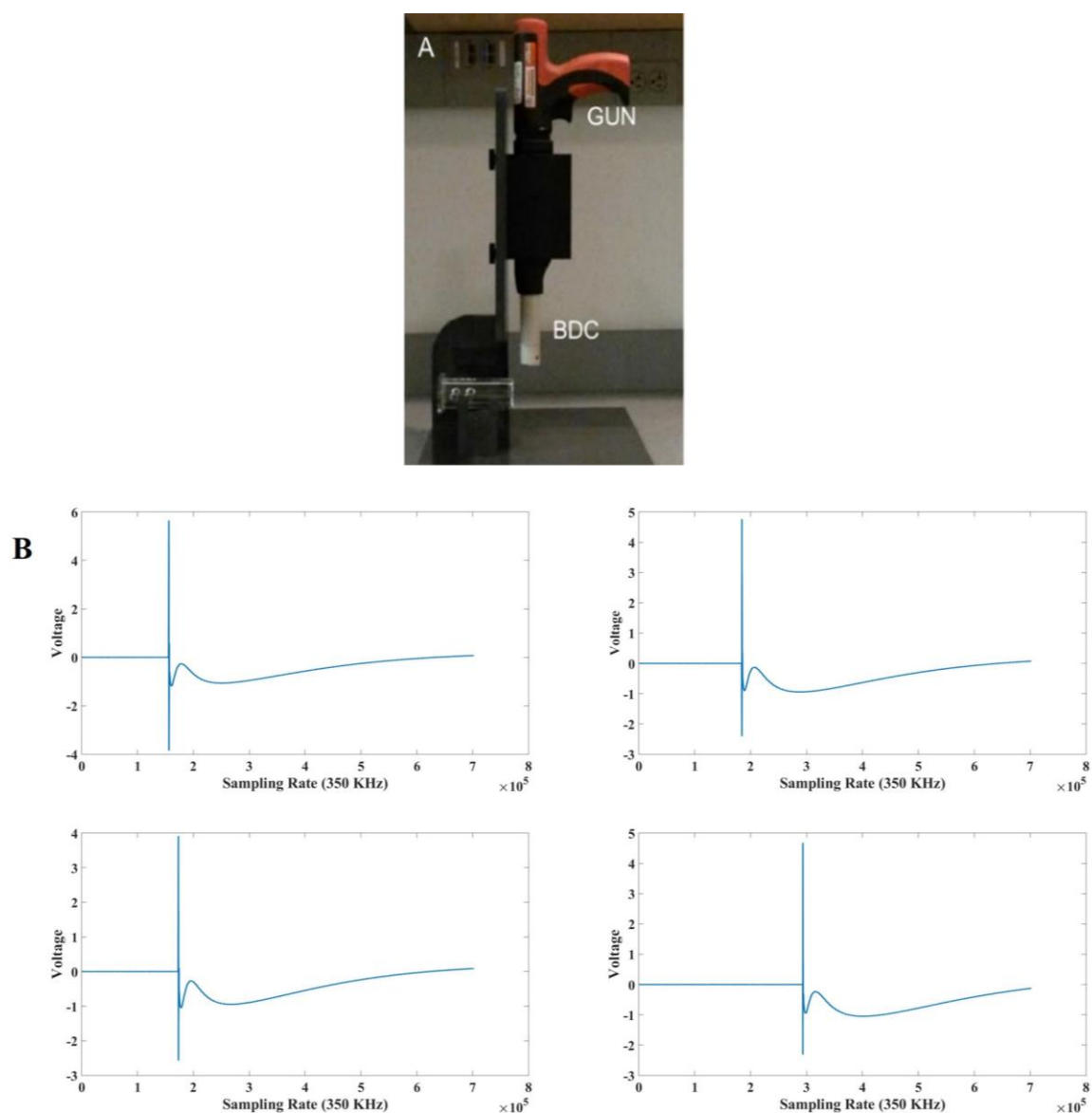


Figure (2-6). Blast pressure of our Cranium Only Blast Injury Apparatus (COBIA). (A) Our COBIA device consists a modified nail gun positioned vertically to deliver blast into the Blast Dissipation Chamber (BDC). (B) Graph of the pressure waveform generated

from the COBIA. Shown are 4 tests that resemble the overall shape of the waveform with an average pressure corresponding to 1307 kPa.

Blast procedure:

Blast injury occurs using the Cranium Only Blast Injury Apparatus (COBIA) (Figure 2-6A) as described and characterized by Kuehn et al. (2011). The COBIA consists of several elements. The central component of the COBIA is a .22 caliber, single-shot, powder-actuated tool (Ramset RS22; ITW Ramset, Glendale Heights, IL). The tool is modified by removing the piston that normally drives the fastener, making the tool function like a firearm and allowing the blast wave to propagate undamped through the barrel. The tool is held vertically using a custom-fabricated stand to allow safe and repeatable use of the tool. The blast is directed downward into a blast dissipation chamber that interfaces snugly with the muzzle of the tool (Figure 1A). This blast dissipation chamber directly delivers the blast overpressure to the head. The blast wave is generated by firing a .22 caliber crimped brass cartridge (power hammer loads power level 4, yellow color coding, with 179 ± 5 mg of smokeless powder).

All animals are inserted and secured into a mouse cylindrical restrainer (Stoelting Co. Wood Dale, IL). Custom paper cones are fitted and wetted around the head to optimally position the head of the animal in relationship to the blast pressure and to prevent potential quaternary damage from gun powder during blasts. Once restrained, animals are inserted such that the cranium is positioned two centimeters below the opening of the blast dissipation chamber. Blast injury is directed between bregma and lambda. For repetitive injuries, animals are allowed to recover 24 hours prior to the subsequent blast

exposure. Following blast(s), the animals are monitored in recovery cages heated with a 37°C heating pad to facilitate adequate thermoregulation with free access to standard chow, Diet Gel, and water. After returning to the Laboratory Animal Care Facility observation continues until the specified survival time point is reached. Control (sham) animals are mice treated identically to the blast exposed mice with the exception of exposure to blast injury. For in vivo imaging of calcium activity in relation to blast, animals are removed from the imaging rig when exposed to blast or sound of gun only and immediately re-inserted into imaging rig for recording.

2.7 Electrophysiology Recording, pharmacology and Optogenetics

All procedures described are in compliance with the National Institutes of Health Guide for the Care and Use of Laboratory Animals, conform to all PHS Policies on Human Care and Use of Laboratory Animals, and have been approved by Boston University's Institutional Animal Care and Use Committee (IACUC). We ran this experiment for awake head-fixed mice to record Local Field Potential (LFP) with glass electrodes filled with saline (impedance 1–5 MOhm). Mice were implanted with custom head-plates that allow access to both striatum and motor cortex. Simultaneous recordings were made in the striatum (stereotactic coordinate: AP (anterior posterior) = -0.2 to 0.8, ML (medial lateral) = 2.0–2.5, and DV (dorsal ventral) = 3.0–3.5) and motor cortex (AP -2, ML 1, DV .7–1). Electrical Signal was recorded with a Multiclamp 700B amplifier, digitized with a Digidata 1440 and acquired with pClamp 10 software at a sampling rate of 20 kHz (Molecular Devices). Recordings and infusions were done in Motor cortex and striatum

that receives projections from both the motor and sensory cortices (Ramanathan S, Hanley JJ, Deniau JM, Bolam JP 2002). Infusion in striata was done by using Carbamoylcholine chloride (Carbachol; from Sigma) was dissolved in saline at a final concentration of 1–2mM and infused at a 0.2 $\mu\text{L}/\text{min}$ rate for 5 mins. The infusion cannula was positioned $\sim 500 \mu\text{m}$ away from the recording electrode tip. Before carbachol infusion, baseline recordings were made for at least 5–10 minutes. Recording was performed throughout the infusion period. For optogenetic experiments, following infusion, sufficient time was allowed to elapse for carbachol-induced beta increases to appear, before optogenetic silencing was begun. In some cases, repeated infusions were made to achieve long last beta oscillations to examine the effect of optogenetic silencing of M1 on induced beta oscillations. For optogenetic silencing, an optical fiber (200 μm in diameter) was coupled to the M1 recording electrode, with the tip of the optical fiber positioned $\sim 500\mu\text{m}$ above the tip of the electrode and positioned $\sim 500 \mu\text{m}$ away from the recording electrode tip similar as infusion cannula.

Optogenetics Experiments

The recording following the beginning of (the first effective) carbachol infusion was analyzed to understand carbachol's effects on beta dynamics in the striatum and cortex. The average time from the end of the last pre-silencing carbachol infusion to the beginning of optogenetic silencing was 10 mins. Optogenetic silencing was effected in trials lasting 30 (n = 3) seconds, with the laser turned on from 5–10 seconds of each trial. In n = 5 mice, carbachol infusions were performed with no subsequent silencing.

CHAPTER THREE: High speed wide-field fluorescence imaging in awake behaving mice yields data from hundreds of individual neurons over millimeters of tissue with high temporal resolution.

3.1 Abstract:

Systems neuroscience has advanced rapidly over the last several decades as techniques for studying neural function have improved. Advances in neurotechnology have been integral to the investigation of neural circuit function in systems neuroscience. One such technique that offers great promise for advancing our understanding is optical imaging of neural tissue. Technical advancements in cameras (cMOS) and data processing combined with advances in calcium and voltage sensors are allowing optical imaging to sample the neural code on much larger scales than has traditionally been achievable. . Here we demonstrate the ability of wide-field imaging to capture the concurrent dynamic activity from hundreds to thousands of neurons over millimeters of brain tissue in behaving mice. This system allows the visualization of morphological details at a higher spatial resolution than has been previously achieved using similar functional imaging modalities to record from large networks of neurons simultaneously. These recordings can be conducted for hours at a time with limited loss of signal due to photo-bleaching. Furthermore, the dynamics of individual neurons can be dissociated from breathing or motion related artifacts and the use of high sampling rates allows for the dissociation of neural responses recruited by discrete task stimuli with millisecond precision in task performing animals.

3.2 Introduction:

A goal of systems neuroscience is to understand how the individual activity of neurons comes to encode or represent, environmental stimuli or a cognitive process. Traditionally, techniques such as unit electrophysiology have focused on sampling from a small number of neurons at once, either locally or regionally. While techniques such as EEG, MEG, fMRI, and PET have focused on global populations of neurons or regions actively engaged during a sample period although they are limited in their spatiotemporal precision, they allow non-invasive access to populations of cells in animal models and humans. One of the challenges of systems neuroscience is to effectively understand the transformation that occurs from individual units to large populations of neurons or “networks.” Particularly how do these networks come to encode information and how do these populations communicate specifically as it relates to information processing, decision making, and the execution of behaviors. Much of our understanding of systems neuroscience can be directly attributed to discoveries from extracellular electrophysiology and the measurements of individual and populations of neurons in task performing subjects. Electrophysiology has given us important insights into the temporal dynamics of neurons and has helped to determine the contributions of distinct neuron types to stimulus encoding or particular behaviors (O’Keefe and Dostrovsky 1971; Gallese, Fadiga et al. 1996; Schultz, Dayan et al. 1997; Hafting, Fyhn et al. 2005). Electrophysiology provides a distinct advantage to measuring the temporal dynamics of neurons but may not be ideally suited for all recording regions, or experimental directives. For example, classification of individual neurons that are sparse in their firing

or particular types of neurons (*i.e.*, classes of GABAergic cells) that are densely packed or share similar waveform properties are often difficult to isolate or identify and may remain undefined or undetected with traditional electrophysiology methods. In addition, recordings are limited to capturing sparse populations of neurons in close proximity to the recording site, leading to challenges in inferring network computations in large populations systems. Sparseness can be overcome in part by larger electrode arrays, but band-width limitations and stability of chronic recordings over days or weeks remain major technical challenges. Even if these factors can be addressed, issues of size and weight of the recording array continue to be a concern, particularly in small rodent model systems like mice, during awake behavior.

Optical imaging techniques concurrent with real-time voltage sensors (St-Pierre, Marshall et al. 2014) or calcium indicators (Andermann, Kerlin et al. 2010; Huber, Gutnisky et al. 2012; Ziv, Burns et al. 2013) offers a potential alternative for recording the ongoing activity of neuronal ensembles during longitudinal behavioral studies. The newest generation of calcium sensors (GCaMPs and GCaMPf), for example, are sensitive enough to characterize single action potential events both *in vitro* and in behaving animals (Chen, Wardill et al. 2013; Sun, Badura et al. 2013).

Optical imaging has traditionally involved wide-field imaging or two photon imaging, each with their own distinctive advantages and disadvantages (Hamel, Grewe et al. 2015; see for recent comparative review of the two techniques). In recent years, two photon microscopy has been a preeminent choice for imaging in tissue, because of its high

spatial resolution, and tissue penetrating features (Hamel, Grewe et al. 2015). Two photon calcium imaging has been broadly applied to individual cells or subcellular components of neurons including spines and axons. Recent studies using two-photon imaging have revealed important insights into how individual cell types contribute to the coding of specific stimuli within neural networks. Because two-photon microscopy employs a scanning mechanism, the signal to noise ratio is primarily influenced by the time spent on imaging each point, and the spatial resolution is primarily determined by the number of points scanned for each image. (Petreanu, Gutnisky et al. 2012; Xu, Harnett et al. 2012; Chen, Wardill et al. 2013; Glickfeld, Andermann et al. 2013). Because two photon microscopy uses a scanning mechanism, the signal to noise ratio is influenced by the time spent imaging each point, and the spatial resolution is determined by the number of points scanned to obtain each image. As a result, the size of the imaging field is inversely correlated with the overall temporal resolution when the signal-to-noise ratio is kept constant. To achieve a relatively high signal-to-noise ratio, conventional two-photon calcium imaging is often performed on small brain areas or across a sparse network of cells, to maintain temporal fidelity.

Wide-field or single photon imaging of neural tissue – either through a microscope or similarly constructed macroscope has proved a useful tool in neuroscience labs for several decades. This approach was first employed to characterize vascular architecture and measure functional indicators of neural activity such as hemodynamic changes in brain tissue (Grinvald, Lieke et al. 1986). This technique's popularity has seen a renaissance recently due to its simple instrumentation, relatively low cost, and

the revolutionary improvement in the fidelity and stability of neural signal indicators. This combined with the synergistic increase in the sensitivity and dynamic range of optoelectronic sensors used for fluorescence detection has made this an increasingly viable tool for neuroscience researchers. New innovations, including the ability to perform wide-field calcium imaging in freely moving animals, through miniaturized microendoscopes systems (Ziv, Burns et al. 2013) and there are promises to increase applicability for the types of experiments that can be performed using this technique. Although wide-field imaging lacks the spatial resolution to resolve fine subcellular structure or the penetrating properties available with two-photon, it is capable of resolving clear neurites and somatic features, including spike detection (Ghosh, Burns et al. 2011). Wide-field microscopy, unlike two-photon imaging, does not rely on scanning features, so it can be used to sample across a large field without having to sacrifice temporal resolution. Additionally, fluorophores may be less bleached using wide-field imaging compared to two photon imaging (Patterson and Piston 2000; Hopt and Neher 2001), which makes it possible to perform sustained illumination and subsequent imaging for an extended period of time – a desired feature for analyzing neural networks during some behavior paradigms (*e.g.*, repeated trial learning paradigms). Thus, wide-field imaging offers an advantage if the objective is to simultaneously recording hundreds of neurons in the brain of a living and behaving animal with high temporal fidelity.

We have set out to illustrate how to assemble and implement a low cost wide-field

imaging system capable of recording the activity of hundreds to thousands of neurons simultaneously in a behaving animal. We also carefully address prominent issues in the field not often discussed including image stabilization, and cell labeling or ROI generation. We then utilize this system to record from the hippocampal CA1 area of awake behaving mice during a well characterized hippocampal dependent behavior task-trace eyeblink conditioning (Solomon, Vander Schaaf et al. 1986; Moyer, Deyo et al. 1990; Tseng, Guan et al. 2004; Sakamoto, Takatsuki et al. 2005; Gruart, Munoz et al. 2006). We conclude by presenting data that demonstrates wide-field imaging responses can be classified with high temporal resolution to discrete elements of task behavior and offer our perspective for the future of this technique, what challenges are left to address, and where we believe emphasis ideally should be placed going forward.

3.3 Result:

Design: wide-field Ca²⁺ imaging of hippocampal CA1 neural network in awake behaving mice:

To demonstrate the use of wide-field microscopy across large brain areas at high spatial and temporal resolution we constructed a conventional epifluorescence microscope for recording in awake head fixed mice. The microscope consists of a 10X objective lens for increased imaging area, a high-intensity LED that can be precisely controlled via TTL pulses, a filter set appropriate for imaging GCaMP6 fluorescence, and a scientific CMOS camera capable of imaging large areas at high speed (Fig. 3-1A). In order to achieve high image quality with good signal-to-noise ratio, we imaged

the hippocampal CA1 region; the CA1 region consists of a thin and densely packed pyramidal cell layer nested between two thick and sparsely populated layers (Fig. 3-1B). This unique anatomical organization of CA1 makes it ideal for wide-field imaging, because there is limited fluorescent signal adjacent to the imaging plane to contaminate the signals from the pyramidal cell bodies.

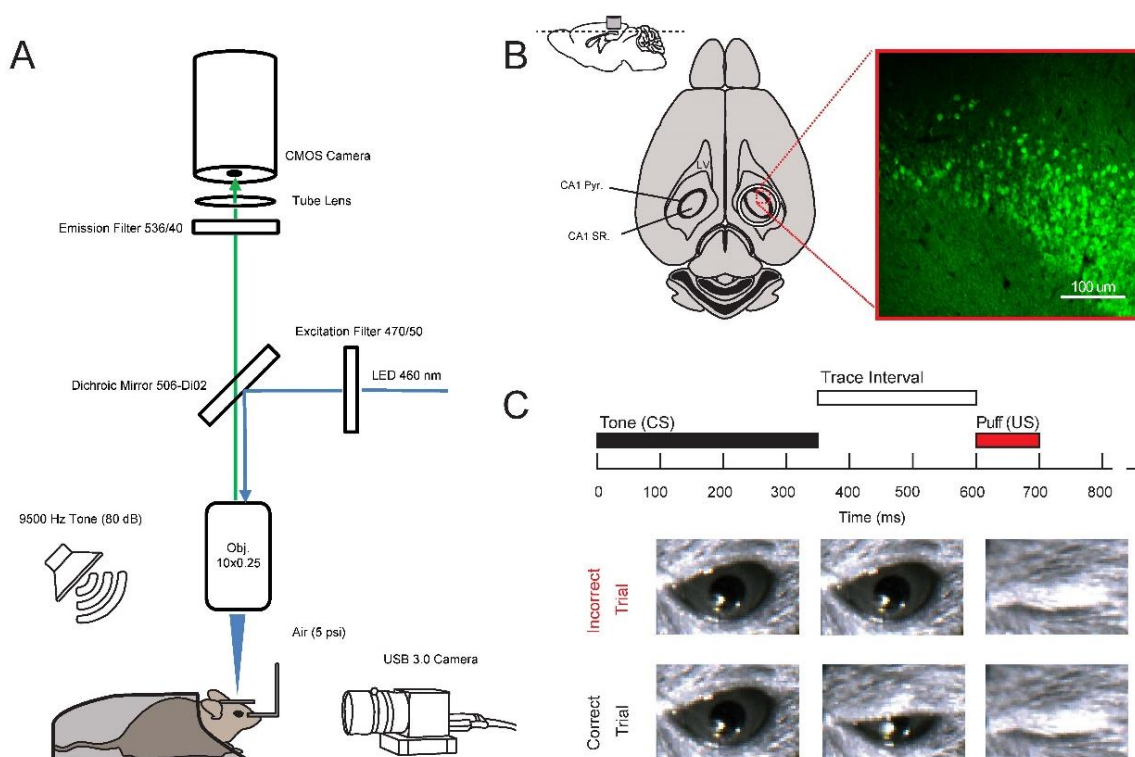


Figure (3-1). (A) Diagram of image acquisition system and behavioral apparatus. Ca^{2+} signals were captured using a CMOS camera and illumination was achieved using a 460 nm LED. Animals were positioned via a head holder under a 10X objective lens. Air puffs were delivered via a cannula directed at the right eye and a USB 3.0 camera was used to monitor eyelid position at 20 Hz. Auditory cues were delivered at 80 dB from a speaker positioned behind the animal. (B) Anatomical depiction of cannula placement and imaging plane. A representative confocal image from the animal analyzed in Figs (3-2, 3-3, 3-4,3-5). Cannula is to scale: note that dorsal CA1 pyramidal cell layer below the cannula (CA1 pyr: stratum pyramidale; SR, stratum radiatum; LV, lateral ventricle). (C) Trace eye-blink paradigm. A 350 ms duration, 9500 Hz pure tone served as the conditioned stimulus (CS). The CS was followed by a 250 ms trace interval, which was followed by a 5 psi, 100 ms long, air puff to the eye

that served as the unconditioned stimulus (US). Eyelid displacement was analyzed offline at the conclusion of the recording.

Mice were surgically injected with AAV-synapsin-GCaMP6f virus into the CA1 pyramidal cell layer, and then chronically implanted with an imaging window for optical recording (Fig. 3-1B). To illustrate the potential of using this system, we utilized the fastest GCaMP6, GCaMP6f, in reporting neural activity changes during behavior. We trained mice on a simple trace conditioning behavioral task that is known to depend on the hippocampus (Moyer, J. R. Jr., Deyo, R. A. & Disterhoft, J. F. 1990; Sakamoto, T. et al. 2005; Solomon, P. R. Thompson, R. F. & Weisz, D. J. et al. 1986; Tseng, W., Guan, R., Disterhoft, J. F. & Weiss, C. 2004) and involve CA1 neurons (Weisz, D. J. & Thompson, R. F. et al. 1983; Green, J. T. & Arenos, J. D. 2007; McEchron, M. D. & Disterhoft, J. F. 1997; . Modi, M. N., Dhawale, A. K. & Bhalla, U. S. 2014). In trace conditioning, animals come to associate two stimuli that are otherwise unrelated. In this case, the conditioned stimulus, a 350 ms long tone, precedes the unconditioned stimulus, a gentle air puff to one eye, with a 250 ms interval (the trace interval) (Fig. 3-1C). Each training session consisted of 40 tone-puff trials with a 31–36 second randomized inter-trial interval (ITI). Performance is quantified via anticipatory eyelid movement that occurs in response to tone, but precedes air puff (Fig. 3-1C). Trace eye blink conditioning is a well-established behavioral paradigm, where mice generally learn the association over 1–3 behavioral training sessions (Sakamoto, T. et al. 2005; Tseng, W., Guan, R., Disterhoft, J. F. & Weiss, C. 2004; Kishimoto, Y. et al. 2001; Kirino, Y. & Kano, M. et al. 2006)

Fluorescence imaging was performed at 20 Hz with an image resolution of 1024×1024 pixels, while an animal was performing trace conditioning training (Supplemental Videos 1, 2 and 3). Although higher resolution and higher sampling rates are achievable (30–100 Hz depending on hardware configuration), this intermediate value allowed us to capture large areas while maintaining high fidelity. The camera was coupled to a 10X objective lens and thus each pixel corresponds to $1.312 \times 1.312 \mu\text{m}^2$, which yields an imaging field of view of $1.343 \times 1.343 \text{ mm}^2$ (Fig. 3-2Ai,ii). Because CA1 pyramidal cells exhibit a diameter of approximately $15 \mu\text{m}$, each cell is represented by several tens to hundreds of pixels, providing a high degree of morphological detail where large dendrites are often clearly observable, especially when they are adjacent to cell bodies (Supplemental Videos 2 and 3). Imaging data were acquired at 16 bits/pixel, which results in about 50 GB of imaging data in a typical 25 minutes recording session. The recording duration was chosen to match other eye-blink studies in terms of the number of trials presented and the duration of the inter-trial interval (Sakamoto, T. et al. 2005; Tseng, W., Guan, R., Disterhoft, J. F. & Weiss, C. 2004; Kishimoto, Y. et al. 2001; Kirino, Y. & Kano, M. et al. 2006). Data acquisition was performed with the commercial software package HCLive running on a multicore computer. We streamed data from the camera directly to RAM to ensure precisely timed acquisition and to avoid potential frame dropping associated with write delays and buffer overflow. At the end of a recording session, imaging data were transferred from RAM to the hard drive for long-term storage and processing. Although, imaging data can be streamed directly from camera to high speed solid state

drives during acquisition, we found that direct streaming in this manner resulted in a small number of missing frames within a behavior session. Behavioral stimuli and image acquisition were triggered by TTL pulses that were controlled via customized MATLAB functions, and recorded for offline validation. Imaging data were stored as multi-page tagged image file format (mpTIFF) and processed offline.

Image processing for motion correction and region of interest (ROI)

identification:

We first performed a series of image pre-processing steps to attenuate motion artifact that is associated with inherent physiological processes, such as respiration, changes in blood flow, or skeletal muscle movement that directly influences the position of the brain. Because the brain is surrounded by cerebral spinal fluid within the skull, any flexing in skeletal plates or jaw movements promote brain displacement in head fixed mice. Motion induced changes in the XY plane can largely be corrected during the image registration process, but changes in depth (Z) or non-rigid deformations in the imaging plane are more troublesome and cannot be easily compensated for.

The motion correction process begins with contrast enhancement to correct for any non-uniformity in illumination of the imaging plane to enhance features for better calculation of correlation in later steps. The motion correction process utilizes phase correlation to measure displacement between the current frame and a reference image consisting of all previously corrected frames averaged together. The frame is then

shifted in the XY plane to offset the displacement. The displacement between images determined during motion correction provides a metric of the magnitude of motion within a recording session. We found that the magnitude of displacement for each imaging session remained relatively constant across animals, with an average of $0.96 \pm 1.32 \mu\text{m}/\text{frame}$ (mean \pm standard deviation, over the 3 imaging sessions analyzed across all 3 mice). We note that z-direction motion cannot be compensated during image processing and that future improvements in hardware instrumentation will be critical to correct this type of motion. In the following analysis, we present detailed characterization from a representative mouse dataset (mouse 26) with an overall displacement of $1.18 \pm 1.65 \mu\text{m}/\text{frame}$ (mean \pm standard deviation across frames). Population data for motion displacement, behavioral performance, and task relevant ROIs for all 3 mice recorded and analyzed are summarized in Tables 3-1, 3-2, and 3-3.

where this problem has been reported that fluctuations of up to $2 \mu\text{m}$ can occur in head fixed animals (Adelman, T. L. & Tank, D. W. et al. 2007). Movement of this magnitude in two-photon imaging can alter signal dramatically as the scanning plane limits the spatial resolution to a few microns. Subtle z-plane movements, however, have a much smaller impact in a wide-field imaging preparation because the focal plane spans tens of microns.

After motion correction, regions of interest (ROIs) were isolated according to the spatial distribution of the fluorescent signals at each pixel. We first selected pixels with relatively high intensity within each frame, and then clustered them into single-

frame ROIs using proximity between activated pixels. Single-frame ROIs were then grouped and merged based on spatially overlapping presentations across frames, and restricted by CA1 neuron morphology. Upon completion of automatic analysis, our software identified 1086 ROIs in the example dataset from mouse 26. This algorithm does not utilize traditional principle component analysis (PCA). Instead it applies fluorescence intensity thresholds for pixel selection and limits the spatial extent of pixel comparisons, thus requiring significantly fewer computational resources and processing data at much faster speeds. Moreover, the computational resources used by this algorithm scales linearly with image resolution, a feature critically needed for analyzing increasingly large datasets in any reasonable period of time. This is in contrast to traditional algorithms like PCA that scale exponentially with image size. Finally, we calculated the signal-to-noise ratio for each of the identified ROI's to determine signal quality. We found that the mean signal-to-noise ratio of all ROIs exceeded 6 in all animals (12.92 ± 0.44 , mean \pm standard error of mean; see Table 3-1).

Table 3-1: Behavioral performance and imaging signal to noise ratio.

Type	Correct Trials	Incorrect Trials	Signal to Noise Ratio
Mouse 26	33	7	20.38+0.68
Mouse 22	30	10	8.56+1.57
Mouse 23	36	4	6.70+0.19

Next, we manually inspected each ROI from the example dataset to determine how the automatic algorithm performed in identifying individual ROIs (Fig. 3-2B). We confirmed that ROI identification was successful when labelling was relatively sparse. However, upon visual inspection, we found that at areas where labelling was dense, it

is in general difficult to distinguish cells that present greater spatial overlaps, especially when these overlapping cells also have significant temporally coincident fluorescence signals. We utilized the default set of parameters in our automatic ROI identification algorithm, with the goal of maximizing the identified number of truly distinct cells, even if they overlap spatially. In order to obtain clearly separable signals from distinct ROIs, we manually selected 422 ROIs that exhibited clear single neuron morphology, as well as defined spatial segregation (Fig. 3-2Aiii). This stringent manual selection process eliminated ROIs that may faithfully represent single neuron activities, but allowed us to avoid repeating or over-representing pixels originating from neurons that share the same anatomical location. A better dissociation would likely be achieved through sparser labeling, as well as better use of temporally segregated fluorescent signals.

Upon completion of semi-automated neuron identification, we extracted the averaged fluorescent intensity of the 422 ROIs for subsequent analysis (Fig. 3-2C). Upon closer examination of the 422 ROIs, we found that these ROIs exhibit fluorescence changes that matched the expected GCaMP6f temporal dynamics associated with neural activity (Fig. 3-2D). Different ROIs exhibit vastly different features, with some sparsely active and others highly dynamic (Fig. 3-2C). For some ROIs, there are clear examples of summation of fluorescence intensity over brief time intervals, likely corresponding to sustained neuron activity over a short period (Fig. 3-2D, E). The highly interspersed temporal patterns of Ca^{2+} responses are consistent with that reported in electrophysiology (Redish, A. D. et al. 2001), and imaging studies of CA1

pyramidal cells (Ziv, Y. et al. 2013; Looger, L. L. & Tank, D. W. et al. 2010). Based on

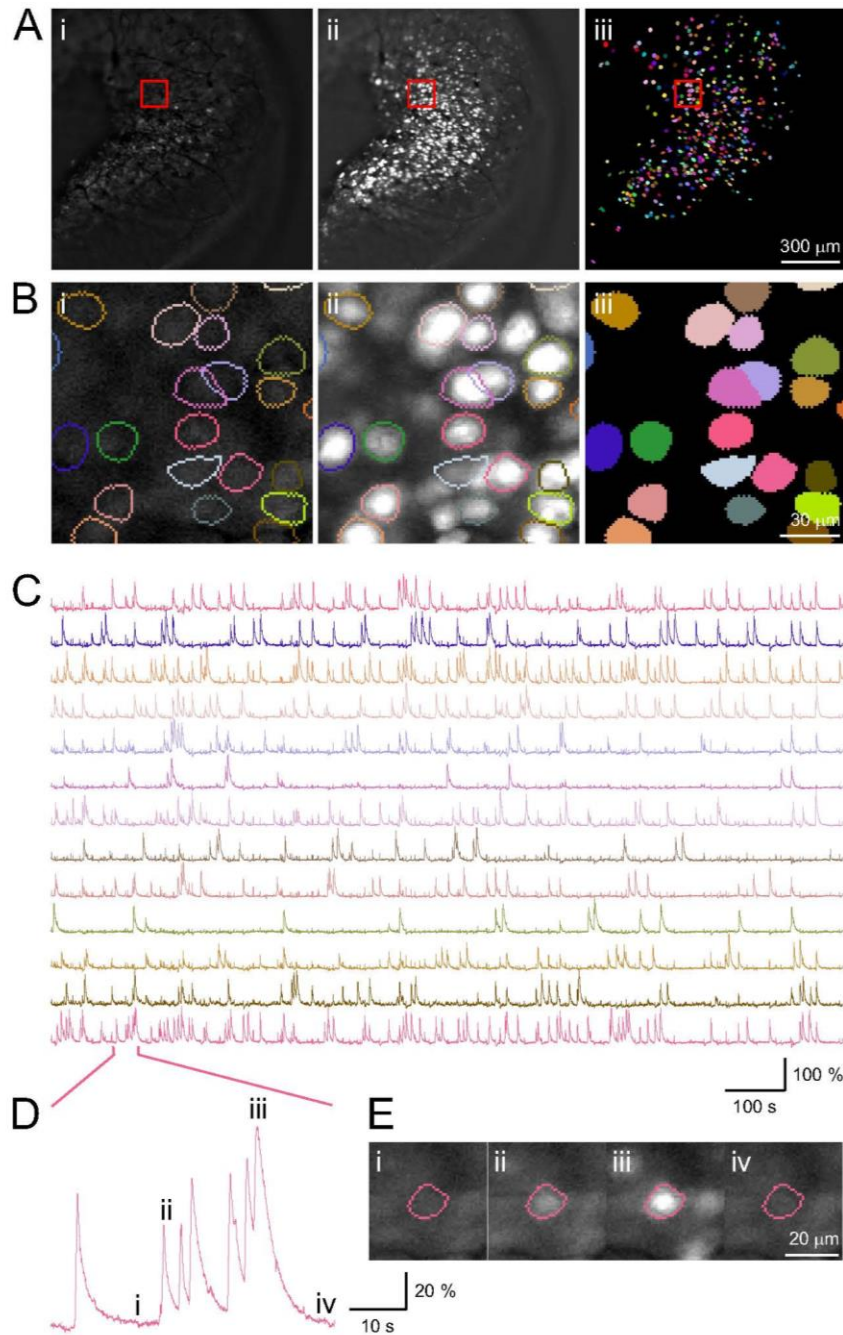


Figure (3-2): Imaging and identification of individual CA1 neurons. (Ai) A representative image frame from a standard imaging session (imaging field is $1343 \times 1343 \mu\text{m}^2$). (Aii) Projection of maximum fluorescence intensity value across all frames. (Aiii) Color plot of all 422 semi-automatically identified neurons

superimposed onto the imaging field of view. **(B)** Zoom in illustration from the area highlighted in the red box from **(A)** (the field is $131.2 \times 131.2 \mu\text{m}^2$). **(C)** Fluorescence traces extracted for neurons shown in **(B)**, with the color for each trace matching those presented in **(B)**. Single dimensional fluorescence amplitude was independently scaled for each neuron. **(D,E)** An example neuron that exhibits highly dynamic features. **(Di,iv)** indicate periods with little activity, and **(Dii,iii)** indicate periods with higher levels of activity.

this evidence, we concluded that these selected ROIs represent individual CA1 neurons. Another examples of ROIs have been shown in (Fig. 3-6) for more mice used in this study.

Ca²⁺ signals in the hippocampus during eyeblink conditioning represent task

related behavior:

We characterized task related neural activity in the identified CA1 neurons by aligning Ca²⁺ responses to tone onset, and then sorting by trial outcome (Fig. 3-3). Trial outcome was assessed by monitoring eyelid position via a USB camera, and calculating eyelid displacement in the interval from tone onset until puff onset. Correct trials were defined as those with significant eyelid displacement relative to baseline, and prior to the air puff, whereas incorrect trials were defined as lack of significant eyelid displacement. For the dataset quantified here, behavioral performance was 82%, consistent with asymptotic performance of 50–90% reported in other trace eye-blink studies (Sakamoto, T. et al. 2005; Kishimoto, Y. et al. 2001; Kirino, Y. & Kano et al. 2006). Behavioral performance data for all animals are reported in Table 3-2.

We found that many neurons showed robust changes upon tone or puff presentation, either showing an increase in fluorescence intensity or a cessation of activity that

lasted several seconds. Several neurons showed Ca^{2+} transients correlated with trial outcome in that they were much more likely to respond to the tone on correct trials as opposed to incorrect trials (Fig. 3-3B, Neurons 172 and 298). Interestingly, some neurons were less likely to exhibit Ca^{2+} transients immediately after tone onset, or a cessation of activity, and thus showed an overall reduction in their trial averaged Ca^{2+} responses (Fig. 3-3B, Neuron 266). This reduction lasted several seconds, which cannot be explained by the brief fluorescence changes associated with motion-mediated artifacts that typically last tens to hundreds of milliseconds (Fig. 3-S1). It was also apparent that many neurons exhibited differential responses depending on whether the animal correctly performed the trial. These findings parallel prior electrophysiology studies demonstrating that the hippocampus codes for relevant task stimuli, and that some neurons exhibit differential neural activity depending on trial outcome 26.

To estimate task involvement from the entire population of simultaneously recorded neurons in this animal, we sorted the 422 neurons based on their mean responses during the 2 second window following tone onset for correct trials (Fig. 3-3C left, 33 correct trials), and for incorrect trials (Fig. 3-3C right, 7 incorrect trials). Upon further analysis, we found that 41% of these neurons showed significant changes within 2 seconds of tone onset on correct trials, with 81 neurons (18%) exhibiting increases in Ca^{2+} responses, and 102 (23%) showing a reduction. We note that because of the limited number of trials used here, it is possible that more neurons may have been

modulated but failed to reach statistical significance. In general, our estimation of 41% is consistent with findings from prior electrophysiology studies (Solomon, P. R., Vander Schaaf, E. R. 1986; Green, J. T. & Arenos, J. D. 2007; McEchron, M. D. & Disterhoft, J. F. 1997; Weiss, C. & Disterhoft, J. F. et al. 2015; McEchron, M. D. & Disterhoft, J. F. 1999). Together, these results demonstrate that Ca^{2+} changes in CA1 can be matched to relevant task stimuli in a classical eye-blink conditioning task, and highlight that GCaMP6f is sensitive enough to represent neuronal dynamics that reflects comparable results from electrophysiology studies.

We then analyzed the responses from the automatically detected 1086 ROIs, using the same categorization criteria. 590 ROIs (53%) showed significant changes in the 2 second window following tone onset, with 216 (19%) exhibiting an increase in Ca^{2+} responses, and 374 (34%) showing a reduction. These ratios are remarkably similar to that obtained from the smaller dataset that were manually selected, suggesting that our automatic ROI detection algorithms achieved reasonable performance. We then applied the same algorithm to classify the neuronal responses from the datasets of all animals recorded and found that in every animal, both positively and negatively modulated subsets of neurons could be identified (see Table 3-2). While it remains unclear how different parameters would impact ROI identification accuracy; additional signal processing methods, such as the ones that evaluate multi-dimensional spatiotemporal interactions (Cowley, B. R. et al. 2013), will likely improve the performance of automatic ROI identification algorithms. Such automated algorithms will make it feasible to process increasingly large datasets

associated with behavioral experiments that often involve multiple sessions from many animals.

Table 3-2: Summary of ROIs detected and motion indexes from all animals in study.

Dataset	Image shift(um/frame, mean±sd)	# of ROI	Positively modulated	Negatively modulated
Mouse26 (selected ROIs)	7.29±4.29	422	81 (19.19%)	102 (24.17)
Mouse 26 (all ROIs)	7.29±4.29	1086	216 (19.89%)	374 (34.44%)
Mouse 26 (no motion correction, selected ROIs)	N/A	422	100 (23.70%)	128 (33.33%)
Mouse 26 (no motion correction, all ROIs)	N/A	1086	304 (27.99%)	330 (30.39%)
Mouse 22 (all ROIs)	23.76±2.11	1797	277 (15.41%)	119 (6.62%)
Mouse 23 (all ROIs)	0.43±1.34	763	471 (61.73)	43 (5.64)

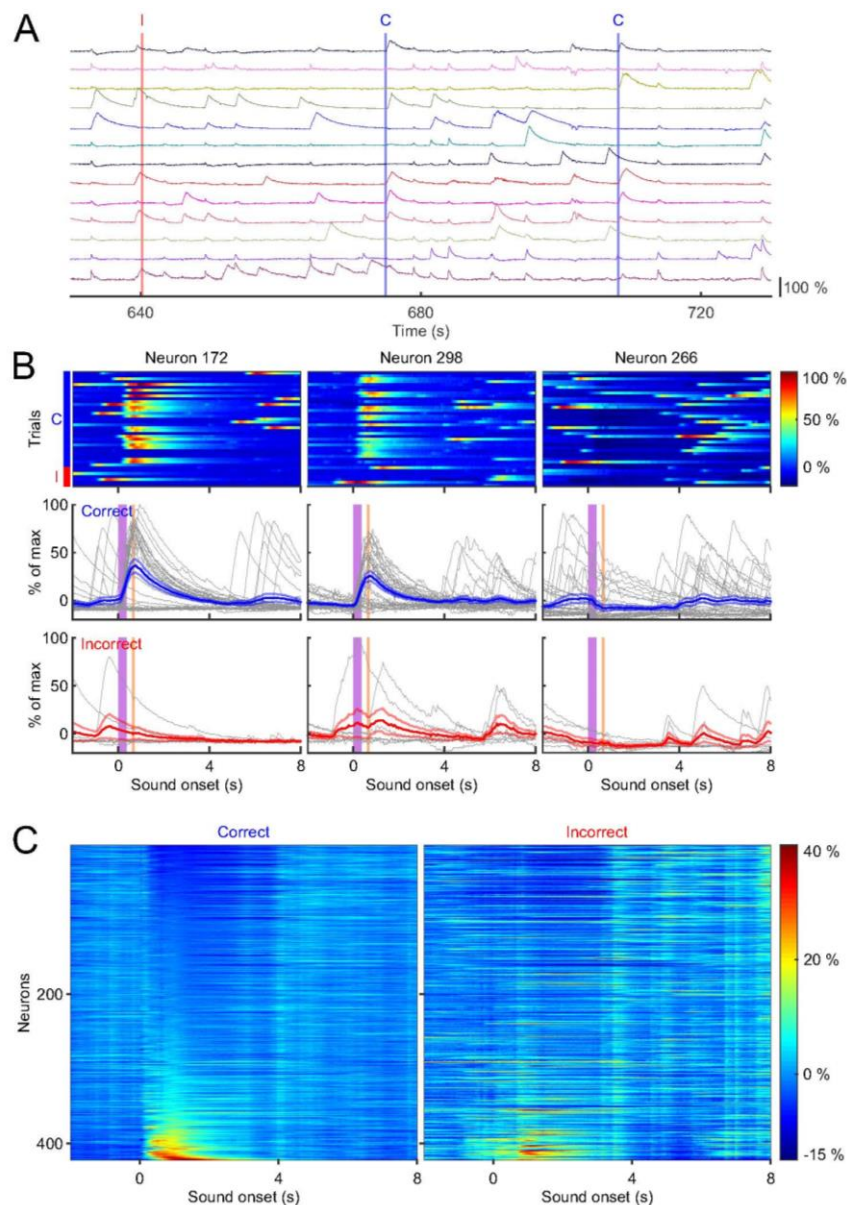


Figure (3-3): Tone evoked responses sorted by response magnitude. (A) Individual traces from 13 representative neurons from a continuous 3 trial window of time. The red vertical demarcation indicates an incorrect trial (labelled with “I” at the top), and the blue lines indicate correct trials (labelled with “C” at the top). (B) Responses of three individual neurons plotted for all 40 trials. Top: plots of Ca^{2+} response magnitude sorted by correct trials (33 trials on the top, indicated by the blue bar to the left) and incorrect trials (7 trials at the bottom, indicated by the red bar to the left). Bottom: individual responses sorted by trial outcome, with each trial response plotted in gray, and averaged response \pm SEM plotted in blue or red depending on trial outcome. (C) Mean response amplitude of all neurons sorted by least responsive (top) to most responsive (bottom), during 0–2 seconds of tone onset, separated by trial outcome.

Temporal resolution of GCaMP6f fluorescence signals in representing neural network dynamics:

Neural network computation by necessity must happen on a rapid time scale, and therefore, maintaining the fidelity of neural interactions is highly relevant in systems neuroscience. Electrophysiology has a unique advantage in temporal precision, capable of resolving the timing of action potentials with sub millisecond precision. To evaluate the temporal resolution of individual Ca^{2+} transients in representing neural dynamics of behavior, we analyzed the time when calcium responses reached the peak after tone onset in the example dataset. We sorted the latency to peak amplitude for all neurons from tone onset until 8 seconds later (Fig. 3-4A), and found that a large portion of the population (184 out of 422) reached their peak within 2 seconds of tone onset (Fig. 3-4B). Of these 184 neurons, 83 reached their peak within 600 ms of tone onset, prior to the puff, suggesting that they are likely responsive to the tone. The remaining 101 neurons peaked between 600 ms and 2 seconds after tone onset, which could represent either sustained activity during the trace interval or a response to the air puff.

We also noticed that many neurons (238 out of 422 ROIs) that did not show a peak response in the 2 second window analyzed, reaching their peak intensity within the several seconds that followed. It is intriguing that these neurons showed delayed peaks that extend into the ITI period, which may reflect the general involvement of CA1 in the maintenance or storage of recent events. Although we cannot specifically pinpoint the functional significance of these delayed signals, it suggests that task relevant

signals may exist in windows of time that have traditionally been deemed task inconsequential.

We then further analyzed the population of 81 neurons that were positively modulated, whose response dynamics can be easily characterized (Fig. 3-4C). These neurons exhibit distinct temporal patterns and reached their peak fluorescence at different time points after tone presentation during correct trials. Interestingly, their activity patterns during incorrect trials are rather different, with many neurons showing robust responses to puff onset instead of tone onset. The differential response profiles between correct and incorrect trials further confirm the task dependent properties of these neurons.

In addition to the difference in the latency to peak amplitude, we also observed distinct kinetic differences in the rate of fluorescence changes. Some neurons showed rapid rises in calcium and reached peak amplitude shortly after tone onset (Fig. 3-4D,E, ROI 327), while others rose more slowly and took longer to reach peak amplitude (Fig. 3-4D,E, ROI 143 and 312). These findings suggest that Ca^{2+} response profiles in the hippocampus can occur over wide time scales, consistent with a functional role in possibly binding distinct events during behavioral trace intervals (Solomon, P. R., Vander Schaaf, E. R. 1986; Sullivan, D. W. & Wu, X. B. et al. 2005). Taken together, our results indicate that calcium imaging using GCaMP6f is sufficiently fast to discriminate neural responses to discrete behavioral elements of the trace eye-blink task.

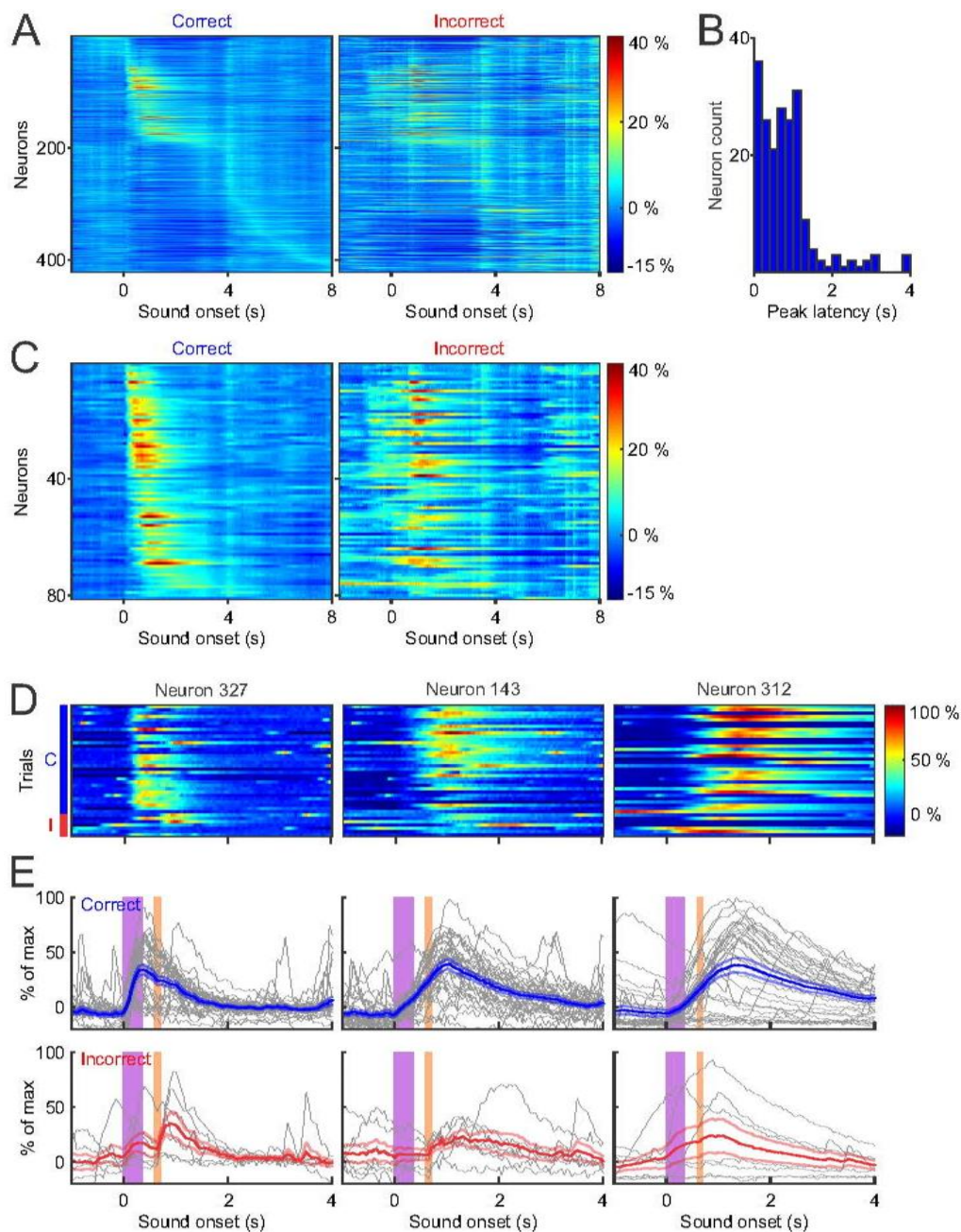


Figure (3-4): Tone evoked responses sorted by latency to peak amplitude. (A) Neurons sorted based on latency following tone presentation over an 8 second window. (B) Histogram distribution of the latency for neurons that reached peak activity within 4 seconds of tone onset. (C) Statistically positively modulated neurons ($n = 81$) sorted by peak latency by trial outcome. (D, E) Three representative neurons that exhibit variability in response kinetics, defined as the rate of fluorescence increase after tone onset. Individual trial responses were plotted in gray, and mean responses \pm SEM were plotted in blue or red, depending on trial outcome.

Anatomical clustering in CA1 hippocampal networks during trace conditioning:

One of the benefits of using wide-field imaging is the ability to sample over very large areas at high temporal resolution. Using our particular experimental configuration, we were able to measure across $1.343 \times 1.343 \text{ mm}^2$, with a theoretical maximum spatial resolution of $1.312 \times 1.312 \text{ }\mu\text{m}^2/\text{pixel}$ without considering light scattering in brain tissue. This distance is large enough to capture a majority of the dorsal CA1 region, allowing us to address previously intractable questions, such as the spatial and temporal topography of neurons over large areas. For example, electrophysiology experiments have suggested that CA1 neurons that respond to a given environmental stimulus are often largely heterogeneous and intermixed (Redish, A. D. et al. 2001; McNaughton, B. L. & O'Keefe, J. et al. 1983; O'Keefe, J. A. 1979); although, there may be some local organization over very small distances, due to the likelihood of receiving coincident inputs as in spatial hippocampal maps (Eichenbaum, H., Shapiro, M. L. & Cohen, N. J. et al. 1989).

In order to examine the spatial distribution of cells that are task relevant, we mapped responses of individual neurons based on their relative anatomical locations. We plotted the location of all 422 neurons from the example dataset based on their average amplitude during the cue-response window defined as the 2 seconds following tone onset (Fig. 3-5A). We did not identify any spatial patterns across the whole imaging field, but did notice that many neurons with similar responses tend to cluster together. For example, we saw neurons that were often in close proximity to other neurons with

similar responses (shown as similar colors in Fig. 3-5A). We further color coded neurons that are either positively modulated (Fig. 3-5B, red), negatively modulated (blue), or unmodulated (gray). Interestingly, positively modulated neurons tended to be largely interspersed throughout the recording window (median distance between cells = 479.05 μm ; Resampling test $p = 0.002$, Fig. 3-5B and Fig. 3-7A) when compared to the median distance between all cells resampled ($402.23 \pm 23.48 \mu\text{m}$, mean of median \pm standard deviation of median). We then looked to see if this phenomenon was conserved across all animals. We found that positively modulated ROIs were more sparsely distributed across all subjects ($567.1 \pm 107.6 \mu\text{m}$; mean \pm SD; $F(1,2) = 26.88$, $p = 0.035$) than non-modulated neurons ($517.8 \pm 96.5 \mu\text{m}$; mean \pm SD; $F(1,2) = 0.01$, $p = 0.914$) when compared to the population distribution. This finding reveals that one advantage of monitoring calcium dynamics over large areas is that that the simultaneous activity of functionally interconnected neurons spread over large distances may be sampled in the same imaging window. In addition, the sensitivity to both increases and decreases of activity could be used to map reciprocal relationships that may differ in polarity of the response based on functional connectivity or anatomical location.

In the example shown in Fig. 3-5B, it is also easily observable that some positively modulated neurons (red) are often in close proximity to other positively modulated neurons, and negatively modulated neurons tend to be next to other negatively modulated neurons, thus forming small red or blue clusters with each containing a few cells. In order to quantify this effect, we calculated the proximal distribution of

neurons of each type (positive, negative, or non-modulated) within a 50 μm distance from the center of each ROI in all animals. We found that across all animals (see Table 3-3), positively modulated neurons tend to be adjacent to other positively modulated neurons as opposed to all other cell types ($p = 0.003$, $z = 2.97$, Mann-Whitney). Such correlated responses in small networks is consistent with previous observations during trace condition using two-photon imaging (Modi, M. N., Dhawale, A. K. & Bhalla, U. S. 2014), and future development in data analysis techniques will likely reveal important insights on the anatomical significance of different functional network activity patterns.

Table 3-3: Spatial clustering of neurons by modulation type.

Type	Positive modulated (# of neurons/50 $\mu\text{m}\pm\text{sd}$)	Negative modulated (# of neurons/50 $\mu\text{m}\pm\text{sd}$)	Non modulated (# of neurons/50 $\mu\text{m}\pm\text{sd}$)
Positively modulated (all)	1.17+1.25	0.41+0.90	2.01+2.22
Negatively modulated (all)	0.81+1.22	1.66+1.62	3.02+1.88
Non modulated (all)	0.81+1.03	0.62+1.08	3.33+2.32

We also looked at whether neurons might cluster by the time course of their responses for all 422 neurons (Fig. 3-5C), and for the 81 positively modulated neurons (Fig. 3-5D). We found no topographical organization based on response latencies when neurons were compared to one another, consistent with what has been previously observed in CA1 cells during spatial navigation (Redish, A. D. et al. 2001).

Interestingly, the small clusters of cells that share similarity in amplitude modulation are not observed in the latency maps, suggesting heterogeneously intermixed temporal patterns of task relevant CA1 neurons, even at small distances. Together, we found

evidence for both spatial and non-spatial organizations across different spatial scales. While at very small scales, some neurons may form clusters according to their task related amplitude modulation, such clusters were not observed when timing was considered. Moreover, while no distinct clusters are observed across the large CA1 network, there may be enhanced segregation between positively modulated neurons.

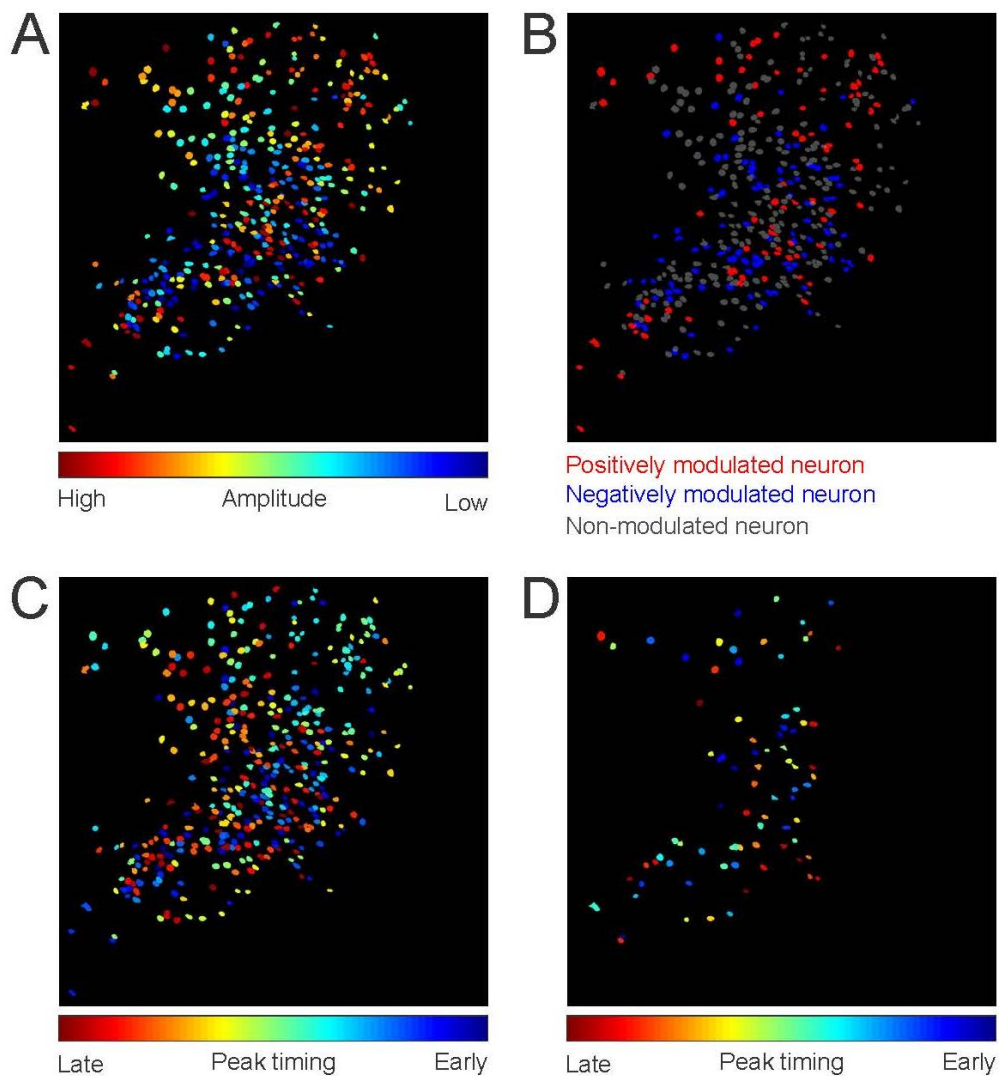
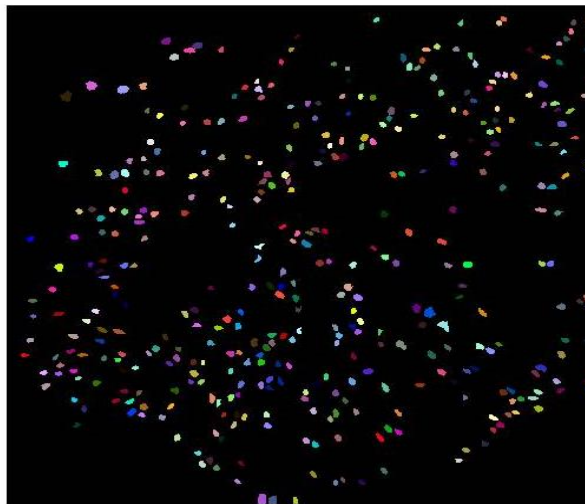


Figure (3-5): Spatial organization of task related CA1 neurons. (A) Spatial distribution of all 422 neurons sorted by averaged amplitude during the cue-response window (0–2 seconds after tone onset). Neurons in dark red demonstrate the highest peak amplitude, whereas neurons in dark blue represent biggest negative amplitudes

during this window. **(B)** Neurons are colored according to their task relevance, with red being significantly positively modulated ($n = 81$ neurons), blue being significantly negatively modulated ($n = 102$ neurons), and gray being not modulated ($n = 239$ neurons). Note, some anatomical clustering of the same color labelled neurons within close proximity to one another. **(C)** Spatial distribution of all 422 neurons sorted by the latency to peak amplitude. Neurons in blue reached peak amplitude quickly, whereas neurons in red reached peak amplitude more slowly. **(D)** Spatial distribution of the 81 positively modulated neurons, sorted by the latency to peak amplitude.

Mouse 22



Mouse 23

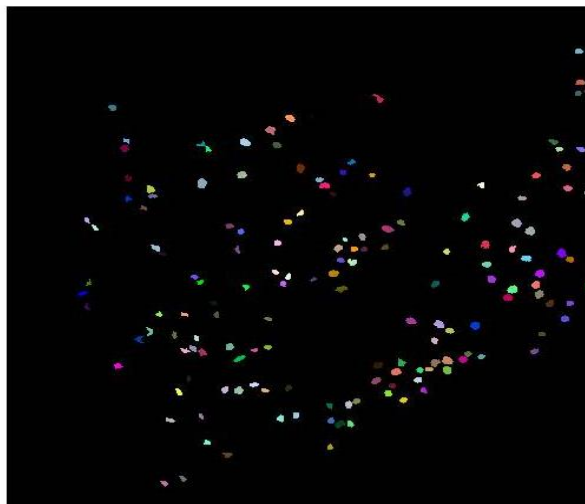


Figure (3-6): Wide field ROI maps for other study subjects. Maps represent all ROIs automatically generated by the algorithm for the other mice analyzed and compare to the map shown in Figure 3-2A.

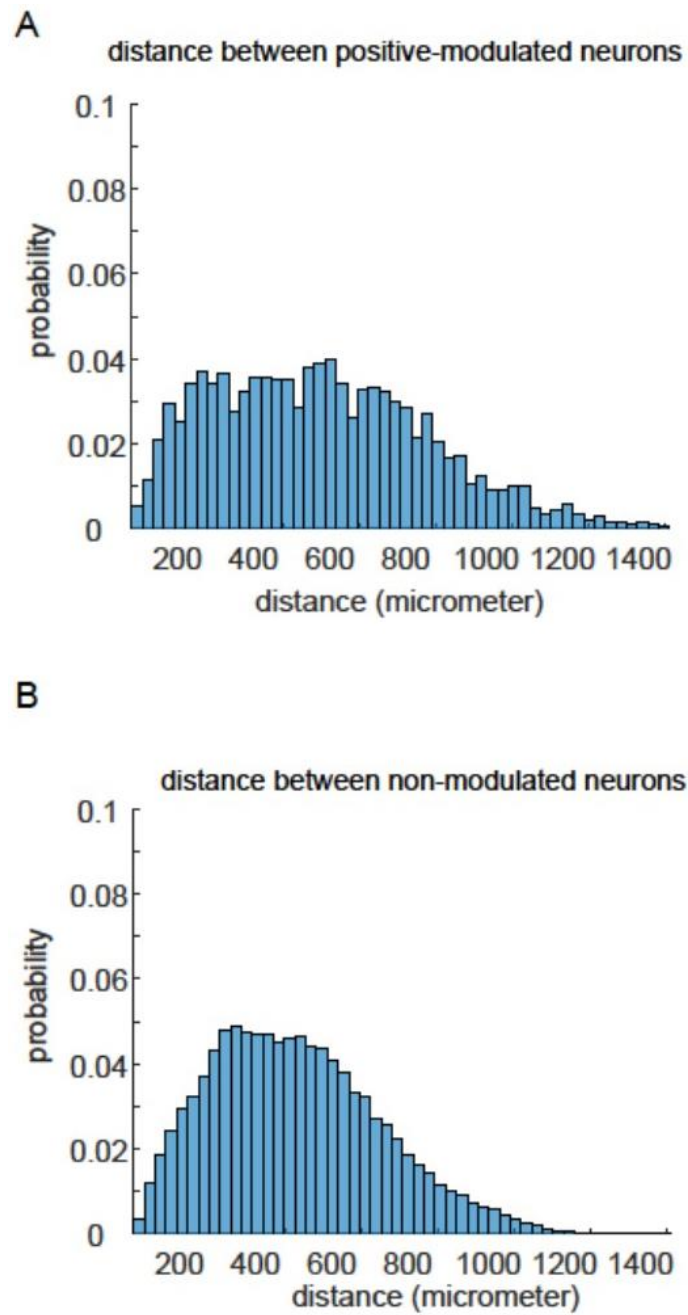


Figure (3-7): Histograms of distance between cells that are positively modulated (A) and non-modulated (B), as defined in Fig. 3-5.

3.4 Discussion:

In this Chapter we have outlined a simple and economical wide-field microscopy optical imaging system that allows for recording the simultaneous activity of hundreds to thousands of neurons in task performing animals. We also demonstrate a software that processes large data sets and identifies the simultaneous activity of hundreds to thousands of neurons. This system is easy to implement and handles large datasets with relative ease. We also address several technical issues related to motion correction, ROI selection, and neuron identification. Although several solutions currently exist for the processing of imaging data as open-source code, no one utility processes full datasets from pre-processing to ROI identification. The software described here combines many of these existing algorithms and features into a single utility that can effectively handle large datasets quickly and effectively, with clear advantages in terms of output, processing time, application, cost, autonomy, and usability.

We used traditional image registration algorithms for motion correction that rely on nonlinear least-square optimization solutions that have been developed for functional imaging data which work well and are freely available (Thevenaz, P., Ruttimann, U. E. & Unser, M. 1998). For example, the NIH program ImageJ, and the associated plugin TurboReg works well for image registration on small datasets of <4 GB (Ghosh, K. K. et al. 2011; Markowitz, J. E. et al. 2015; Mukamel, E. A., Nimmerjahn, A. & Schnitzer, M. J. 2009). However, as data size increases, ImageJ requires increasing demands on user input and processing time, with large files >30 GB taking 4–8 times longer when

compared to this software using the same computer. This includes the time spent to manually load files, initiate concatenation, and to start the registration process (see Table 4). Once finished, user input is also required to save the output files for further processing. Each of these steps is automated using the software provided here. Another advantage is that the software here is not limited by available desktop RAM. The use of ImageJ required available desktop RAM at 2.5X the original recording file, limiting the size of files that can be processed by standard computers. In addition to automating the registration process, we also automated ROI detection as an alternative to the commonly used method of defining ROIs manually. In order to do this we utilize a threshold based ROI selection algorithm. This method does not rely on principle component analysis (PCA) or independent component analysis (ICA), thereby requiring significantly less computational resources and time. Excellent software algorithms are available that apply PCA/ICA based algorithms (Mukamel, E. A., Nimmerjahn, A. & Schnitzer, M. J. 2009) and are well suited for ROI identification. However, we found that on our large datasets, computational time was prohibitive to daily data collection and analysis. Therefore we developed an algorithm that applies an adaptive threshold to normalized pixel intensity and groups neighboring thresholded pixels into single-frame ROIs based on proximity (see methods for details). Single frame ROIs were then clustered into multi-frame ROIs that were used to describe the spatial extent of each highlighted neuron. We found that this produced reliable ROI identification in approximately 1/12 of the time of PCA based strategies using the same analysis computer.

We applied this system to recordings from CA1 neurons in a well characterized hippocampal dependent task and confirmed that the calcium dynamics observed in a large fraction of these neurons are task related, consistent with prior electrophysiology studies (Thompson, R. F. & Weisz, D. J. et al. 1986; Green, J. T. & Arenos, J. D. 2007; McEchron, M. D. & Disterhoft, J. F. 1997; Weiss, C. & Disterhoft, J. F. et al. 2015; McEchron, M. D. & Disterhoft, J. F. 1999; McEchron, M. D., Weible, A. P. & Disterhoft, J. F. 2001; Fernandez-Mas, R. & Delgado-Garcia, J. M. et al. 2001). Because of the ability to image a large portion of the CA1 region, we found that task related CA1 neurons showed little clustering across a large spatial and temporal scales, but tended to form small spatial clusters that were modulated in response amplitude but not response latencies. We also demonstrate that Ca^{2+} imaging provides sufficient temporal resolution to measure neural network dynamics associated with distinct phases of behavior.

Based on our characterization, we conclude that for a variety of tasks, wide field imaging offers the potential to answer questions that other techniques may not. Although GCaMP6f has an improved temporal response relative to other genetically encoded Ca^{2+} indicators, its temporal resolution remains limited to resolving signals separated by tens or hundreds of milliseconds. Electrophysiology has far better temporal resolution when it can be applied, but may not be suitable for all experimental conditions. Future advances are likely to alleviate some of these concerns as larger and less invasive electrical recording arrays are developed along with the technology to enhance sampling bandwidth. As of now though, if information from

large populations or from specific cell types that can be genetically targeted is required, Ca^{2+} imaging provides a unique alternative. In addition, Ca^{2+} imaging offers the potential to capture more sparsely active neurons providing an opportunity to analyze additional network dynamics that might otherwise be missed.

We found that, although minor, motion artifacts are an omnipresent issue inherent to recordings made in awake behaving animals. It is likely that motion will remain an inherent problem in all imaging techniques, as many physiological processes introduce micro-movements that need to be compensated for. We observed small rhythmic motion, such as respiration and heart rate that is virtually undetectable following motion registration. For larger motion artifact due to skeletal muscle movement, such as grooming or posture shifts, our motion correction algorithms largely attenuated this motion artifact. Despite the success of our algorithm, we do believe that imaging at a faster speed could further improve motion correction, because motion displacement between frames will be minimized. Additionally, the use of a second fluorescent label utilizing a Ca^{2+} insensitive fluorophore might offer better motion estimation, and serve as a more ideal template for ROI identification. Another advantage of a second label would be that it could provide a better estimation regarding the number of neurons in the recording field, regardless of neural activity.

Wide-field imaging can be easily applicable to different brain regions and can be used to target specific cell types through transgenic or viral based gene targeting strategies (Sayeg, M. K. et al. 2015; Han, X. 2012). Wide-field imaging also provides a solution

for long term tracking of neural signals over days or weeks offering insight into questions about how individual cell populations come to form ensembles and how such representations are stabilized over days and weeks (Ziv, Y. et al. 2013). While two-photon has been a prime choice for imaging neural activities because of its superb spatiotemporal resolution, wide-field imaging represents a complementary choice at lower cost for imaging a larger brain area at higher speed. Wide-field imaging also may be less sensitive to photobleaching (Hopt, A. & Neher, E. 2001; Patterson, G. H. & Piston, D. W. 2000), allowing for much longer continuous recordings without the fear of a deleterious reduction in signal. Over the ~25 minute recording sessions analyzed in this manuscript, we found photobleaching accounted for ~6.7% reduction in signal intensity across all animals ($6.70 \pm 5.74\%$, mean \pm SD).

An additional future challenge of recording from larger number of neurons with high spatial and temporal resolution will be downstream image processing and data analysis, particularly as better voltage and calcium indicators are developed with finer temporal profiles. Further improvement of signal processing algorithms as well as data acquisition procedures would allow better representation and segregation of optical signals from individual neurons in wide-field imaging. Considering the potential to record from thousands to tens of thousands of neurons is in the foreseeable future, it will be beneficial to optimize data processing and analysis algorithms (Mukamel, E. A., Nimmerjahn, A. & Schnitzer, M. J. 2009; Freeman, J. et al. 2014). It is also unclear how different signal processing methods might bias neuron selection or activity detection, underscoring the importance of contrasting sorting methodologies. Beyond

identification, analysis of interactions amongst thousands of individual neurons across behavioral conditions is going to require novel tools that increase the ease of performing multi-dimensional analysis (Cowley, B. R. et al. 2013). It is our view that the continued development of optical imaging methods in systems neuroscience fundamentally relies on a collective effort that furthers the development of analysis software tools available via open access.

CHAPTER FOUR: Calcium Imaging Enables The Analysis of Neural Network Upon Mechanical Blast Relevant to Traumatic Blast Injury.

4.1 Abstract:

Traumatic brain injury (TBI) is characterized by symptoms including cognitive deficits and behavioral difficulties resulting from mechanical injury to the head and brain. The physiologic changes that invoke these symptoms are largely unknown, and consequently there are no methods for identifying or treating this illness. Thus it is important to study this disease in an animal model. This can be accomplished by inducing mechanical injury by brain blasting in awake animals, monitoring the progression of TBI symptoms in the long term, and tracking activity in injured neural circuits. Blasting induced TBI has the potential role of short term changes in neuronal Calcium dynamics that might lead to long term change in neural circuitry. In vivo work in this research area is sparse. In our study we are trying to shed light on the transient change in Calcium signals that occurs after blasting. Our implemented Wide field Optical microscope gives us the opportunity to image thousands of neurons with high spatial and temporal resolution over long periods of time. This study contributes a new method to enhance our understanding of the transient blasting effect.

4.2 Introduction:

Changes in intracellular calcium concentration that are correlated with optical signals from calcium imaging play an important role in understanding the pathophysiology of mechanical injury to the brain and how this perturbs brain activity. These changes in

calcium systems could induce changes in single neurons, many neurons, or entire circuit function (Delorenzo et al. 2005). Because glutamate receptors can sense or respond to mechanical force that is applied during traumatic brain injury, this stimulation could damage or kill neurons by excessive increase in free calcium during the early injury phase (Raghupathi, 2004; Delorenzo et al. 2005). It is demonstrated in hippocampal neuronal culture model that calcium remains elevated in for a long time after the initial injury (Raza et al. 2001). The elevation in neuronal Calcium dynamics plays an important role in mediating the persistent neuronal plasticity. Many studies demonstrated changes in Calcium dynamics in the acute time period following TBI (Sahuquillo et al. 2001). However, there are no studies on calcium dynamics following traumatic brain injury in vivo.

In our study we imaged baseline calcium activity for a short period of time (Imaging Protocol of Blasting) then repeated the same imaging session after 24 hours followed by a first blast then we started imaging calcium activity again after increasing intervals. The following day we repeated the same procedure with a second blasting session. We found that there is an abrupt change in calcium activity following each blast. The change shows that many neurons exhibit prolonged calcium accumulation and other neurons exhibit a long period of silencing. These results demonstrate that blasting caused alterations in both Calcium levels and in hippocampal neurons in head-fixed wake animal. This elevation and change suggest that long-term changes in Calcium buffering or Calcium release may contribute to the alterations in Calcium dynamics in the surviving Blasting

neurons and offer new insights into our understanding of the pathophysiology of brain injury related to mechanical force.

4.3 Result:

In this experiment we used 6 mice; 3 mice were used to investigate the effect of blasting on hippocampal neurons in awake mice and the other 3 were used as control mice to investigate the effect of “sham” blasting over hippocampal neurons.

The Effect of Blasting on Calcium signaling over time:

We began this experiment by imaging for 100 seconds immediately before blasting to establish a baseline measure of calcium activity. Immediately after blasting we imaged for another 100 second period, followed by 4 more periods beginning at 10 minutes, 20 minutes, 30 minutes and 60 minutes after the blast.

Fig (4-1B,C) show some examples of ΔF traces extracted from ROIs over exemplary neurons picked from a blasted mouse (Day 1- Blast 1). Most neurons demonstrate normal activity over time, except the first 3 neurons (Neuron 19, Neuron 105 and Neuron 150) which show a transient increase in calcium signal over 100 seconds after blasting but begin to return back to normal condition 10 minutes after blasting. Plotting all neurons which we imaged per session over time provides clear evidence of how the mechanical force of a blast interrupts neural activity, which might lead or be connected to traumatic brain injury.

Fig (4-2) shows us the behavior of hundreds of neurons over time (972 ROIs detected from Mouse 1 – Blast 1). We sorted all neurons in each figure based on the average ΔF over the first 100 seconds of the included timeline. Fig (4-2A) represents 100 seconds of imaging immediately before blasting and sorted by average response amplitude. Activity across the population appears normally distributed. Following the blast (Fig 4-2B) we observe that a small segment of the population demonstrates a substantial increase in sustained calcium entry as identified by increased fluorescence that remains for a duration exceeding fluctuations observed in normal baseline activity (~100 neurons). The remainder of the population exhibits the opposite effect, i.e. substantial decrease in fluorescence that persists for seconds to minutes before returning to baseline activity. When we look at calcium activity after 10 minutes (start at 200 seconds on graph), it is clear that most inactive neurons successfully resume their normal activity. Fig (4-2C) is similar to fig (4-2B), except that neurons are sorted based on the average response amplitude during the last 100 seconds to make sure that what we saw in previous figure is not a sorting artifact.

Data from the second blast session for the same mouse (Fig 4-3, 1024 ROIs detected from Mouse 1 – Blast 2) exhibit the same general effect as those from the first blast session (Fig 4-2). However, the fraction of neurons showing a substantial elevation in calcium activity is much smaller (~50 neurons). Blasting session data from two more mice also exhibit this effect, except that from the first session of the second mouse, which may have been compromised by movement at the time of the blast. While the general effect is relatively consistent, there is variability in the number of neurons showing an

elevation in calcium signal from mouse to mouse and even from day to day for the same mouse.

Fig 4-4 shows the spatial distribution of the calcium fluorescence response to blasting (Ai, Bi) in the same mouse on two different days, as well as the neural response after 60 minutes of recovery (Aii, Bii). The change in the spatial distribution of calcium fluorescence response to blasting suggests different neurons may be responding differently in each day. However, while the spatial response is variable the timeline of recovery of neural activity to baseline levels is consistent.

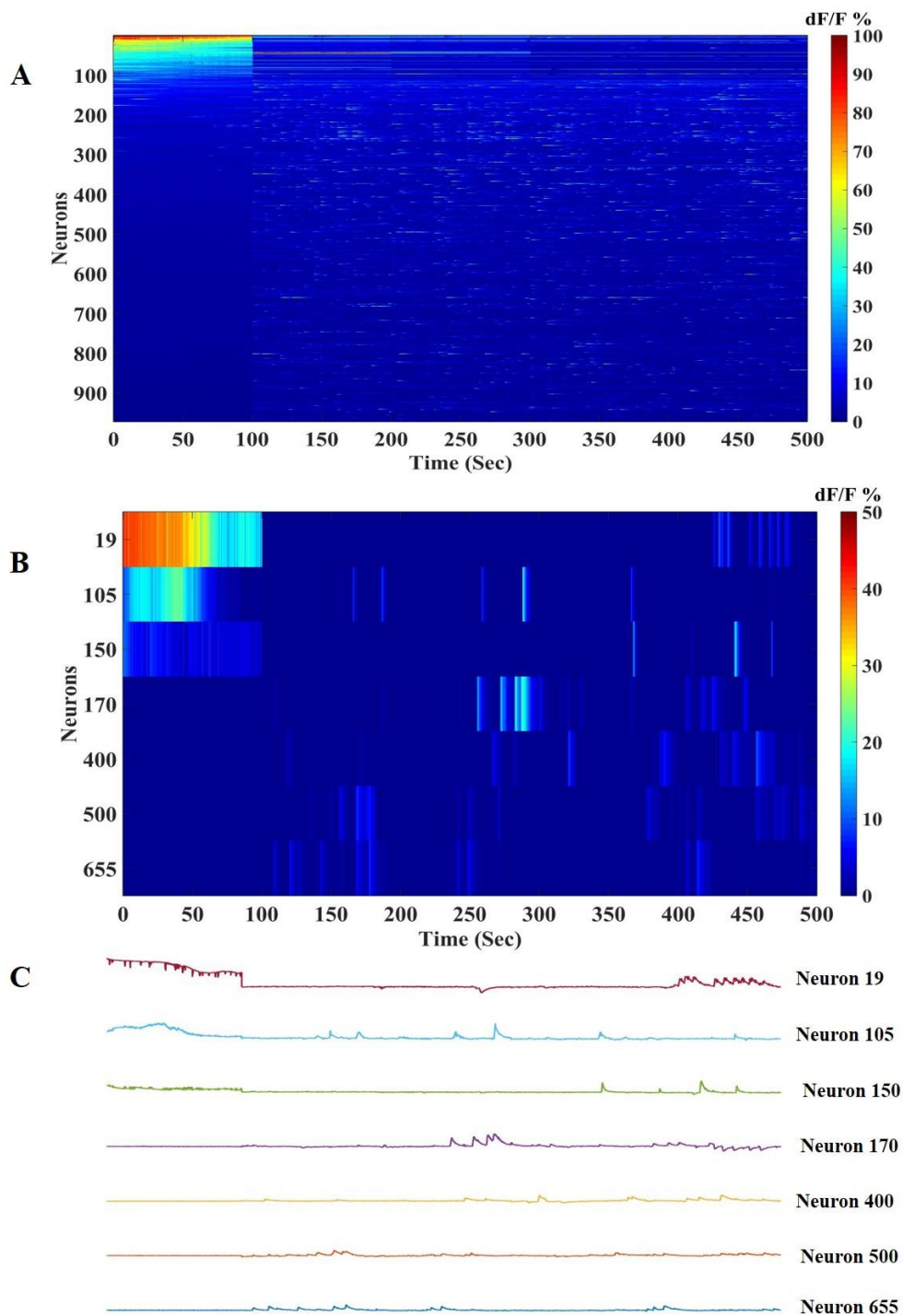


Figure (4-1). Example of some individual imaging CA1 neurons over time, (A) All Neurons response magnitude after blasting, (B) Few neurons from (A) zoomed in (C) Fluorescence traces extracted for neurons shown in (B),

Control sessions were run with 3 mice. In these sessions mice were only exposed to the sound generated by blasting by moving the animal holder away from the gun by at least 30 cm. Figures 4-6 show the first control mouse (Day 1 – Sham Blast 1, Day 2 – Sham Blast 2), These figures were generated in the same way as figures 2 & 3; neurons are sorted based on the average fluorescence response amplitude before blasting (A_i & B_i) and average response amplitude of first 100 seconds after blasting (A_{ii} & B_{ii}). The results in these figures demonstrate a clear difference between blasted mice and control mice in the neural response during the first 100 seconds after a blasting event. Also, the rest of control mice show the same normal response before and after sham blasting.

To quantify this effect we normalized fluorescence intensity for each neuron to scale between 0 and 100, then quantized the mean normalized fluorescence intensity during each continuous imaging period and measured the entropy of the population using Shannon's formula (equation 4-1). This gives a measure of randomness or uncertainty in population activity, and can be used to indicate a general effect of an external disturbance on an entire neural population.

$$\text{Entropy} = - \sum_{i=0}^n P(x_i) * \log_2(P(x_i)) \quad (4-1)$$

Where $P(x_i)$ is the probability of having x neurons having a mean normalized fluorescence intensity in bin i ($n = 10$ bins). the minimum value of Entropy is zero and there is no limit to maximum value.

Figure 4-7 shows the difference in entropy of the neural population response magnitude between a group of blasted mice and a group of control mice. The blasted mice show a

consistent reduction in individual and average entropy from the first 100 second imaging period to the last 100 second imaging period recorded 1 hour later. This is also consistent with figure 4-4 which shows a reduction in overall average amplitude of calcium signal. In contrast the individual and average entropy for control mice is almost constant between the first and last imaging period.

Calculating the maximum difference in entropy by subtracting the minimum entropy from maximum value of entropy for each mouse and each day (fig 4-8) gives us a statistical number which represent the average of maximum difference in entropy which is equal to 0.5 ± 0.159 for blasted mice and equal to 0.137 ± 0.087 for control mice.

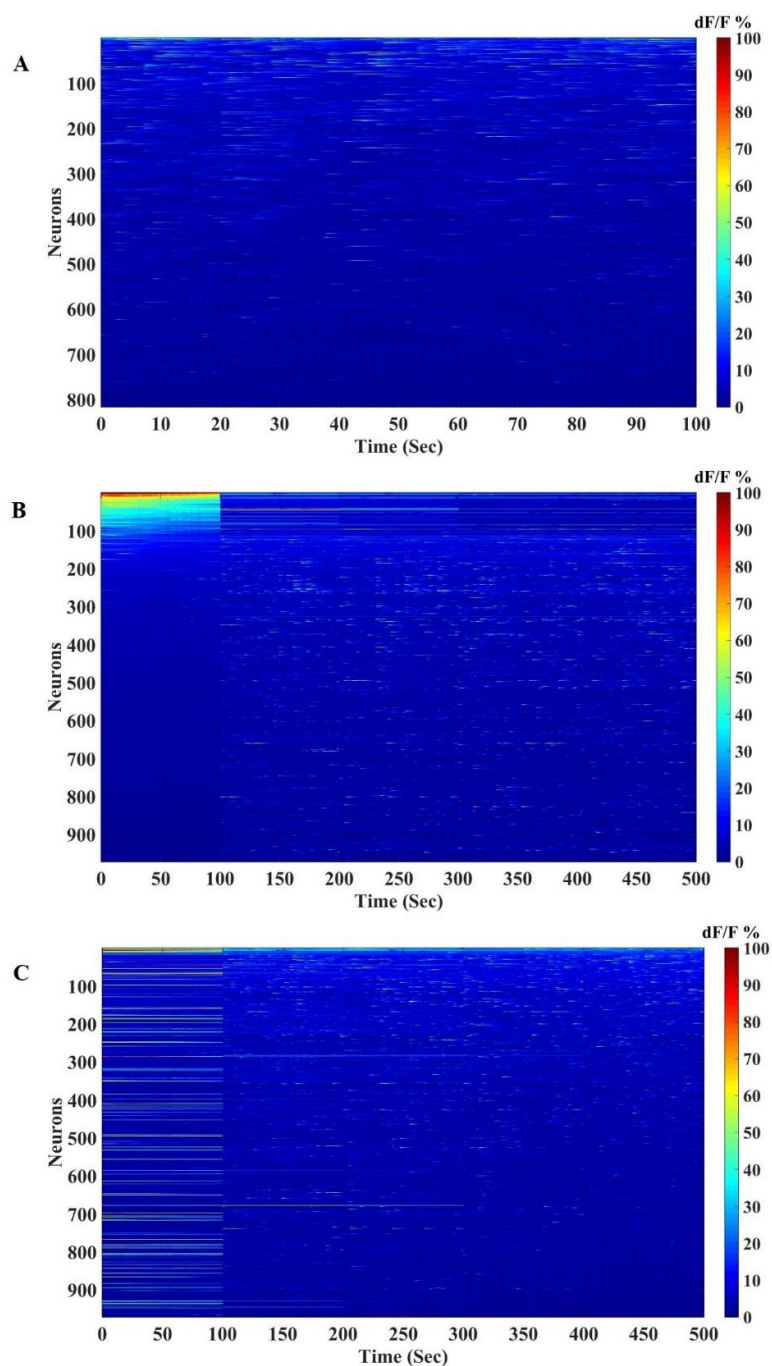


Figure (4-2). Neurons response magnitude before and after blasting of blasted mouse 1-Day 1, (A) Showing Neurons response magnitude right before blasting sorted by descending magnitude based on average of magnitude over whole trace, (B) Showing Neurons response magnitude after blasting sorted by descending magnitude based on average of magnitude over first 100 (Sec), (C) Showing Neurons response magnitude after blasting sorted by descending magnitude based on average of magnitude over last 100 (Sec).

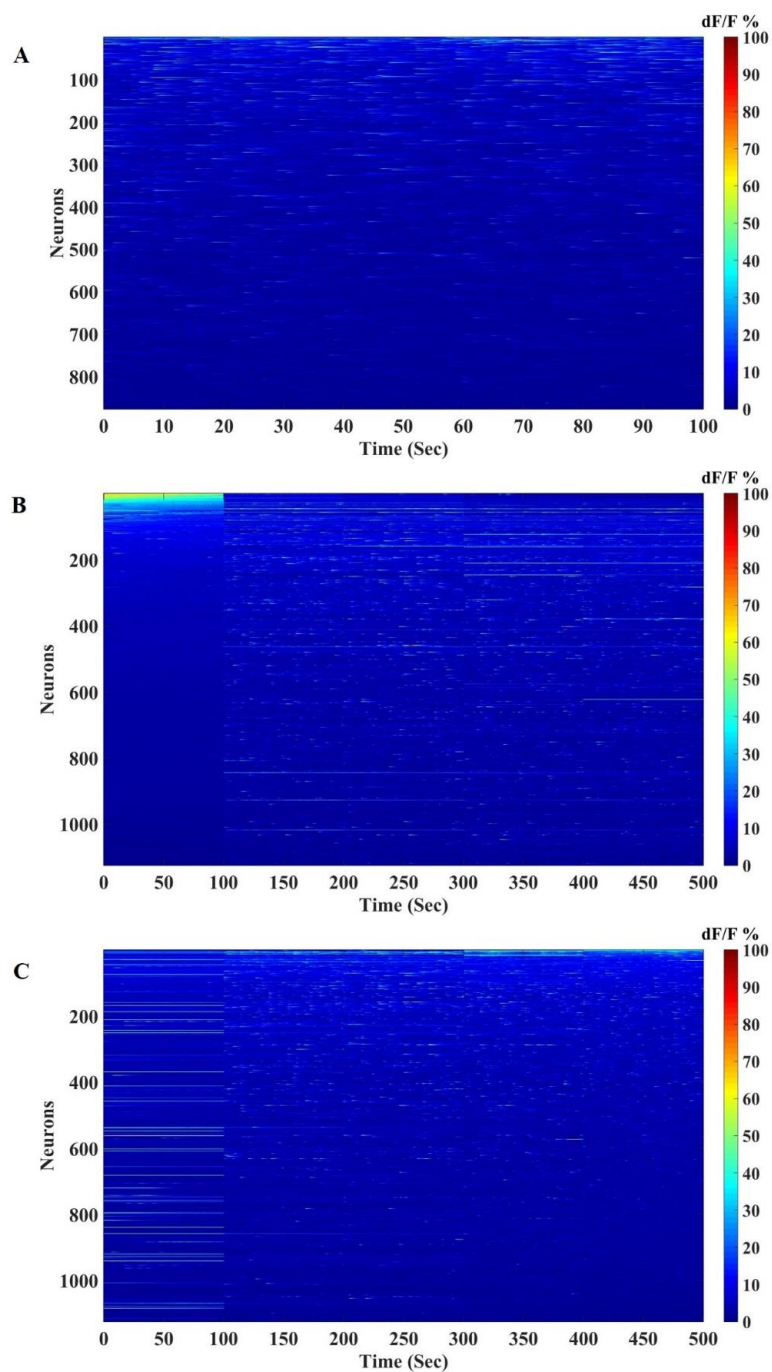


Figure (4-3). Neurons response magnitude before and after blasting of blasted mouse 1-Day 2, (A) Showing Neurons response magnitude right before blasting sorted by descending magnitude based on average of magnitude over whole trace, (B) Showing Neurons response magnitude after blasting sorted by descending magnitude based on average of magnitude over first 100 (Sec), (C) Showing Neurons response magnitude after blasting sorted by descending magnitude based on average of magnitude over last 100 (Sec).

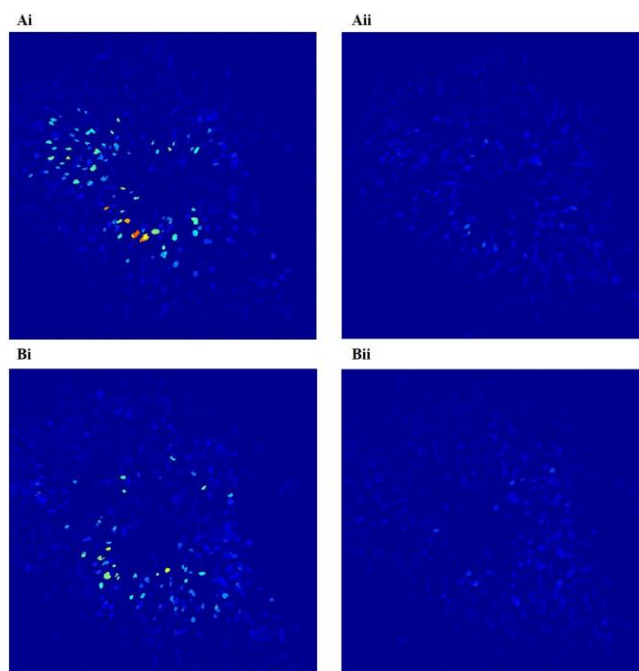


Figure (4-4). Z-stack projection of average fluorescence magnitude value. (Ai) projection for the first 100 Sec after blasting for mouse 1 – Day 1, (Aii) projection for the last 100 Sec after blasting for Mice 1 – Day 1, (Bi) projection for the first 100 Sec after blasting for mouse 1 – Day 2, (Bii) projection for the last 100 Sec after blasting for mouse 1–Day 2.

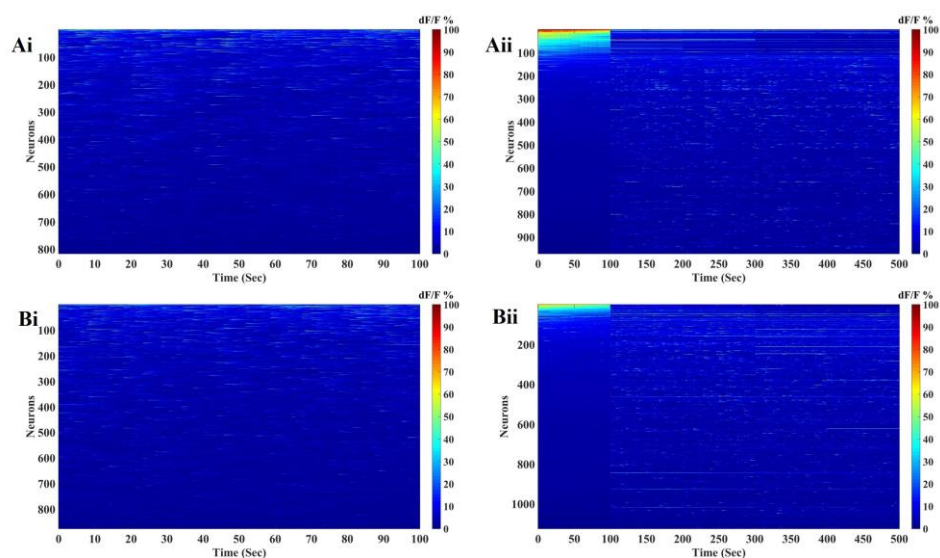


Figure (4-5). Summary of Day1 and Day 2 for the first blasted mouse (Ai) represent 100 sec baseline right before blasting for Day 1 (Aii) represent the time course after blasting for Day1, (Bi) represent 100 sec baseline right before blasting for Day 2 (Bii) represent the time course after blasting for Day 2,

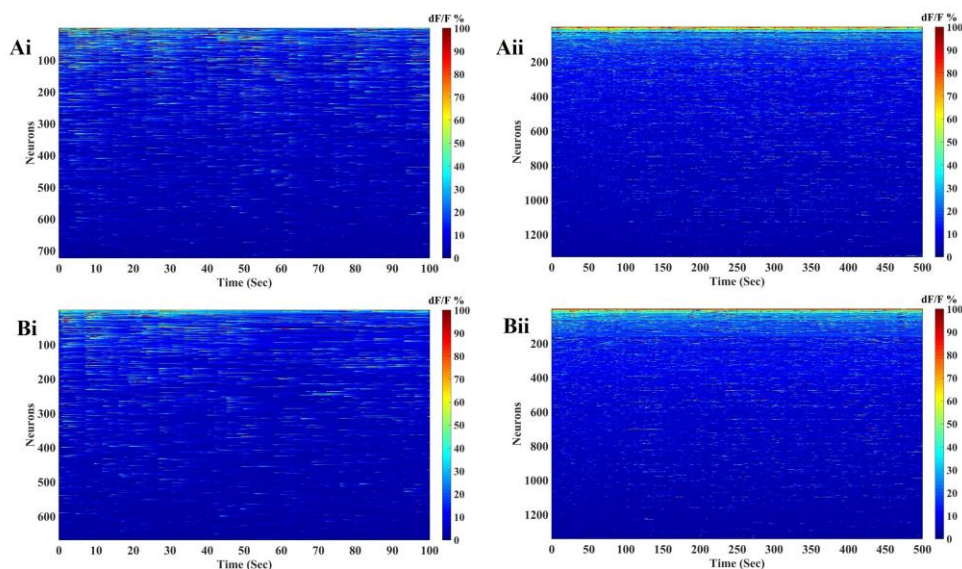


Figure (4-6). Summary of Day1 and Day 2 for control mice (Ai) represent 100 sec baseline right before sham blasting for Day 1 (Aii) represent the time course after sham blasting for Day1, (Bi) represent 100 sec baseline right before blasting for Day 2 (Bii) represent the time course after sham blasting for Day 2,

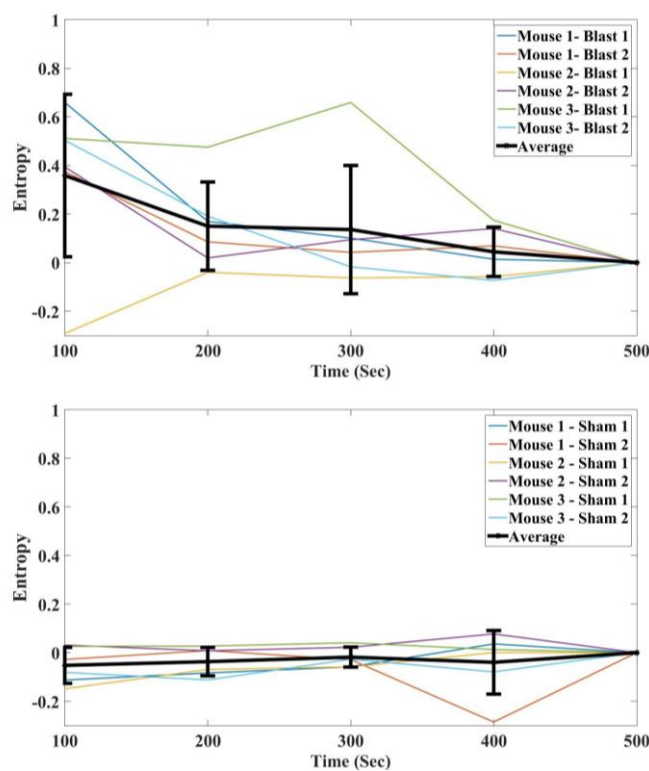


Figure (4-7). Calculating Entropy for All of our mice Over Time windows, (A) Blasted Mice, (B) Control Mice.

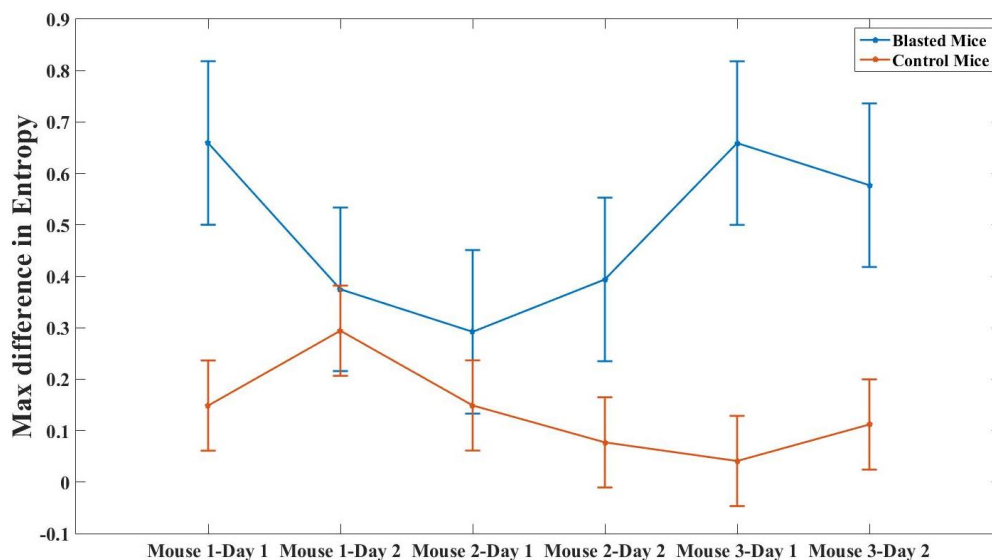


Figure (4-8). Calculating Maximum difference in Entropy for All of our mice for Blasted Mice and Control Mice.

4.4 Discussion:

Mechanical deformation of brain tissue which triggers or initiates traumatic brain injury has been studied extensively in vitro. The mechanism of changes in cellular physiology in response to mechanical events is still unknown. Substantial elevation in extracellular glutamate and other neurotransmitters have been observed in associated with calcium entry to neurons, which is called stretch induced delayed depolarization (Tavalin et al., 1995). The findings of our study which is done in vivo have shown that mechanical injury can induce sustained abnormal elevations in calcium signal followed by a return to normal state within 1 hour. This trend is consistent with previous work on cultured neurons which show elevations in calcium entry in response to a blast of air which return to baseline after 24 hours.

Computational modeling of brain concussion induced by blast wave is very demanding to assess the physiological change of traumatic brain injury that evoke brain disorders reflecting in behavior changes, cognitive deficits and motor impairment. Due to the lack of imaging techniques providing information about the impact of blasting on activity of neural populations at cellular level. It is hard to assess the mechanical effect on neural activity at cellular level.

Blasting wave produces physical impacts relating to relative motion of brain to skull, the initial impact occurs when skull accelerates or decelerates suddenly. Then brain hit against skull at least twice in different directions. This impact leads to microscopic structure damage, which affects the supply of nutrition to those areas.

Neural stretching causes an ionic influx and efflux for Ca^{2+} and K^{+} respectively and a reduction in blood supply. To restore neural membrane potential, ionic pump should work to compensate neural ionic concentration to normal level. This will increase demand for adenosine triphosphate (ATP) which in turn increase glucose metabolism and blood supply. fMRI and CT scan could provide information about blood flow but their poor temporal and spatial resolution, we could not get enough information to understand the impact of blasting over individual neurons.

Our sensor GCaMP6f is used in first study to track temporal dynamics of Ca^{2+} ion but in this study GCaMP6f has been used as a potential sensor to estimate force distribution at each imaged neuron upon blasting if we know Elasticity parameters then we could evaluate the amount of stress and strain at each point in brain to evaluate the amount of

damage that might evoke a cascades of events lead to TBI symptoms but our sensor is limited by saturation level of Ca^{2+} to know exactly how much Ca^{2+} influx inside damaged neuron. Our study is a new simple method trying to introduce a new paradigm to collect information from blasted brain which might help to know how blasting wave interact with brain at cellular level.

CHAPTER FIVE: Optogenetics Interrogation of Basal Ganglia Network Relevant for Parkinson's disease

5.1 Abstract:

Optogenetics techniques add a new horizon to investigate neural circuitry and understand mechanisms associated with some neural disease. In this chapter we trying to understand the source of enhanced oscillations in the beta frequency band (8–30 Hz) which are a characteristic neural signature observed in the cortical-basal ganglia-thalamic (CBT) loop of Parkinson's disease (PD) patients. While beta oscillations have been shown to be correlated with parkinsonian motor symptoms, the mechanisms underlying the generation and propagation of beta oscillations in PD are not well-understood. Our Lab have previously shown both computationally and experimentally that increased cholinergic activation in the striatum can lead to enhanced beta oscillations in normal, non-parkinsonian mice (McCarthy et al., 2011). Here, we infused the acetylcholine agonist carbachol into the striatum of normal adult mice to produce beta oscillations and used optogenetics silencer in Motor Cortex and recorded simultaneously from the striatum and motor cortex (M1). We found that striatal carbachol-induced beta oscillations can propagate to M1, engaging distinct sub-frequency oscillation patterns. Also silencing M1 excitatory neurons did not significantly alter power in the beta frequency range in either striatum or M1

5.2 Introduction:

The invention of optogenetics toolbox contributed significantly in the field of system neuroscience. It provides a precise highly spatiotemporal control for a specific type of neurons to crack down neural circuitry and give insight about the function and role of each type of neurons in the investigated circuit (Kay M. Tye and Karl Deisseroth, 2012).

In previous chapters, a genetic indicator fluorescence protein (GCaMP) has been used as a calcium sensor to optically track neural activity over time but our imaging speed is limited by the speed of recording camera and GCaMP kinetics plus we could not manipulate neural activity to quantify the role of neurons in circuit. In addition to that a neural calcium imaging does not give us a full information about brain wave (Local Field Potential).

In this study, Optogenetics and Electrophysiology tools have been used to understand the cortical-basal ganglia-thalamic (CBT) loop of Parkinson's disease (PD). Given the importance of network dynamics in the CBT loop to both movement and movement disorders, it has previously not been shown whether the carbachol-induced beta propagates to other nuclei in the basal ganglia-thalamo-cortical loop. By inducing beta oscillations in the striatum using carbachol infusion and investigated: (i) whether striatal beta propagates, (ii) the relationship between beta oscillations in different regions of the loop and (iii) how optogenetics affect this beta oscillation. To address this, we recorded simultaneous LFPs from the striatum and M1 in normal mice during striatal carbachol infusion. We found that increases in beta oscillation power appear simultaneously in both M1 and striatum after striatal carbachol infusion. While motor cortex and striatum were

nearly synchronized at beta frequencies before carbachol infusion, striatum phase led M1 at beta frequencies < 20 Hz after carbachol infusion.

These observations suggested that striatally generated high beta oscillations may propagate to M1 when striatal MSNs are over-excited, for example during a state of artificially increased cholinergic tone. To further dissociate the roles of cortex and basal ganglia in the expression of beta oscillations within the CBT loop, we optogenetically silenced M1 excitatory neurons, including those that project from cortex to basal ganglia, in carbachol-infused mice. Silencing M1 pyramids did not significantly alter beta power in either striatum or M1, suggesting M1 input to basal ganglia is not critical for the production of elevated beta oscillations under the condition of high striatal cholinergic tone. These results interpreted in the context of our previous modeling work, suggest the existence of a beta generator in basal ganglia networks, independent of cortical input but requiring a sufficient level of excitation in striatum.

5.3 Results:

Increased striatal cholinergic tone increases beta frequency oscillations in striatum

We have previously demonstrated that local infusion of non-selective cholinergic agonist carbachol in the striatum in normal mice resulted elevated striatal beta oscillations [McCarthy, M.M., et al. 2011]. To further characterize the cholinergic induced oscillations across distinct frequency bands within the striatum, and other structures of the CBT network, we here performed simultaneous recording in the striatum, and the primary motor cortex (M1), while infusing carbachol in the striatum Fig. (5-1).

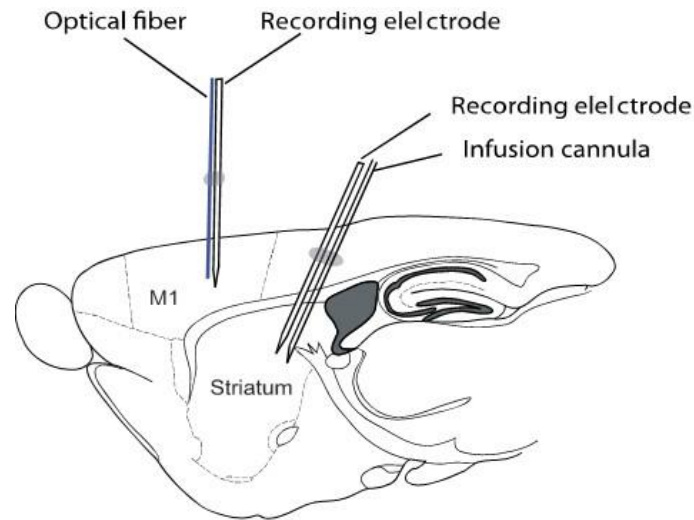


Figure (5-1). Illustration of the infusion cannula, recording electrodes and optogenetic stimulation fiber configurations. Carbachol was infused into the striatum. LFPs were recorded in both striatum and M1. The optical fiber in M1 was used to optogenetically silence deep layer M1 excitatory neurons.

We observed periodic beta increases in the striatum at varying times following carbachol infusion, consistent with what we observed in our earlier study (McCarthy et al., 2011). The beta produced by carbachol infusion was often burst, and often interrupted by large LFP deflections that accompanied tic-like movements. These large LFP deflections had characteristic peak-like deflections (“peaks”) were observed in all mice, and are in particular prominent in 3 animals examined (Fig. 5-2C). Such large LFP deflections produced a broadband increase in power spectrum analysis with the most energy at low frequencies and thus biased the estimation of oscillation power at specific frequency bands.

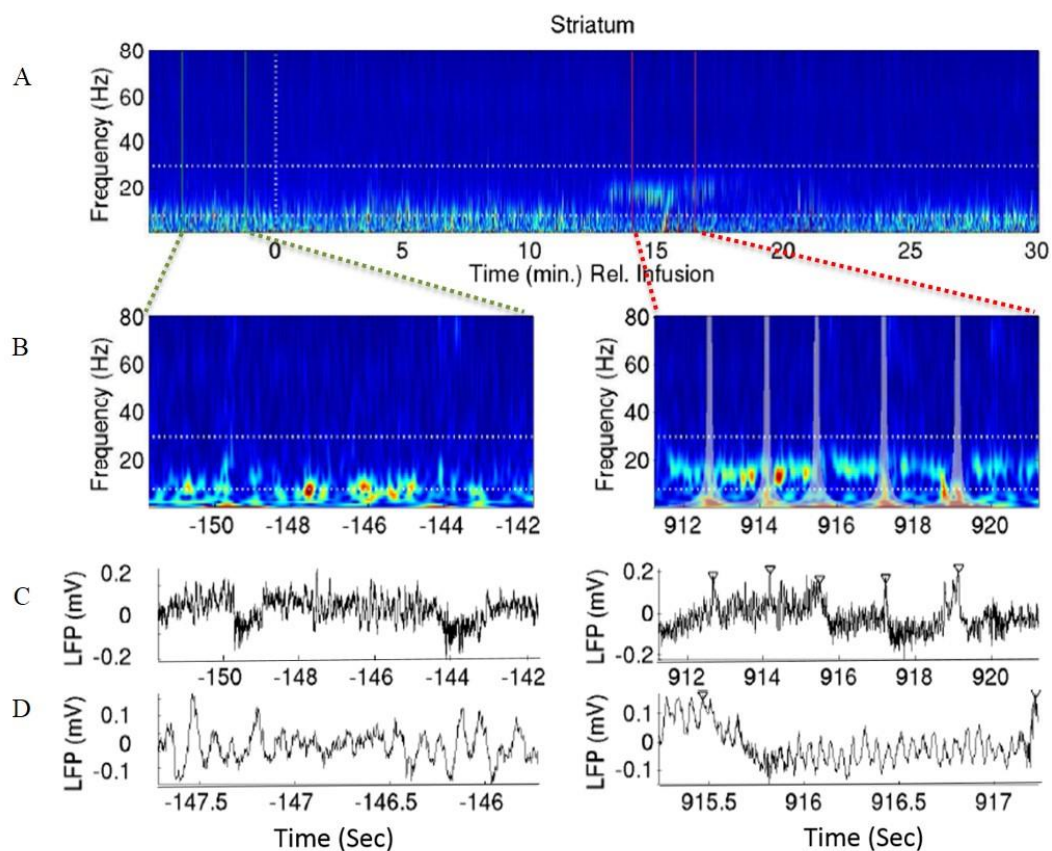


Figure (5-2). (A) Spectrogram from an individual mouse pre and post striatal carbachol infusion. The peak of the beta elevation occurs about 15 mins after the start of infusion. Green and red vertical lines denote the time periods shown in B. (B) Close-up of spectrogram for pre and post-infusion times in B. (C) Raw LFP recordings for the pre and post-infusion times shown in B. Inverted triangles represent artifacts that were removed before analysis of the LFP. (D) Close-up of the pre and post-infusion LFPs shown in C.

We found that striatal Carbachol infusion selectively increased oscillation powers at beta frequencies, around 15 – 30 Hz in the striatum, with a well-defined oscillatory peak centered at approximately 20Hz (Figure 5-2). In contrast, oscillatory power below or above beta frequencies was all reduced, including theta frequencies (~3–8 Hz) and gamma frequencies (~55–165 Hz) (Fig. 5-3A, B). We previously demonstrated an increase in beta frequency oscillation power in striatum in response to carbachol infusion

[McCarthy et al., 2011]. Here we confirm and extend these results to show that striatal carbachol infusion leads to a selective increase in beta frequency power in striatum.

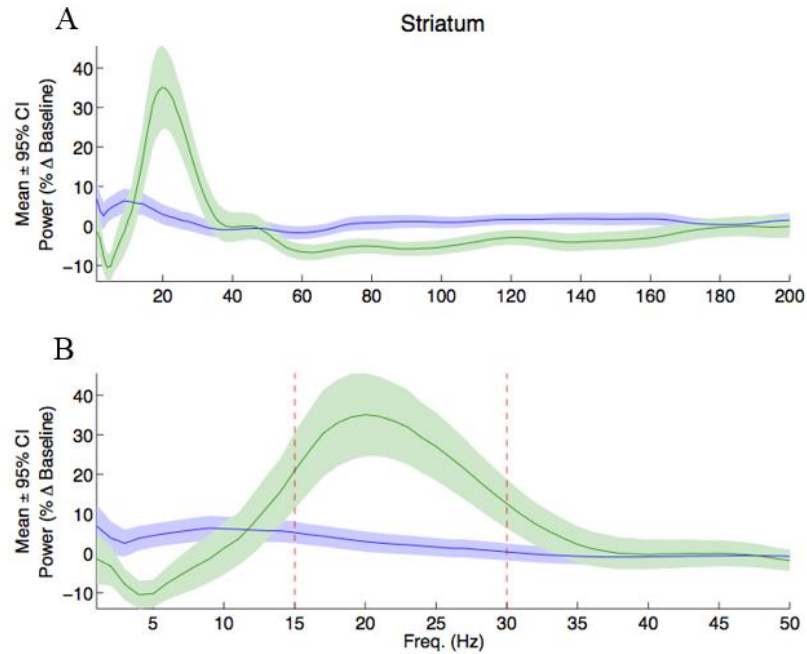


Figure (5-3). (A) Population striatum LFP power spectral density before (blue line) and after (green line) carbachol infusion. (B) Close-up of A with the red dashed lines denoting the limits of the beta band

Carbachol-induced beta elevation in striatum is accompanied by elevated beta oscillations in the primary motor cortex (M1)

To examine whether elevations in striatal beta power after carbachol infusion were paralleled by an elevation of beta oscillatory power in other brain structures of the CBT networks, we examined the spectral power in the simultaneously recorded LFPs in M1. M1 is most directly connected to voluntary movement within the CBT network, as outputs from M1 project to the spinal motor neurons and interneurons [Baker, S.N., et

al. 2015]. We calculated the oscillations observed in LFPs recorded in M1, during periods of elevated beta oscillations in the striatum.

After striatal carbachol infusion, beta oscillations increased in M1, as that observed in the striatum (Fig. 2A, B, 4A, B). The large LFP deflections observed in striatum (Fig. 5-2C) also occurred in M1 (Fig. 5-4C).

Consistent with that observed in the striatum, the increase in oscillations in M1 is selective to beta frequencies, around 15–30Hz, with a well-defined center at approximately 27Hz (Fig. 5-4D,E). Interestingly, the peak of the beta oscillation in M1 was slightly higher than the peak in striatum (Fig. 5-4E). This upward shift in the peak frequency between striatal beta oscillations and M1 cortical beta oscillations was also noted in a recent study during a cued choice task in normal rats [Leventhal, D.K., et al. 2012], suggesting that striatal Carbachol induced beta oscillations may recruit the regular beta generation mechanisms as occur in natural conditions.

Additionally, in contrast to the broadband decrease in gamma power seen in striatum after carbachol infusion, we found two significant dips in oscillatory power in the gamma frequency range: one centered around 60 Hz and the other centered around 150 Hz (Fig. 5-4A,B). In summary, a selective increase in M1 beta power occurs simultaneously with increased beta power in striatum after striatal carbachol infusion, suggesting that striatal carbachol infusion can effectively engage the CBT network at beta frequencies.

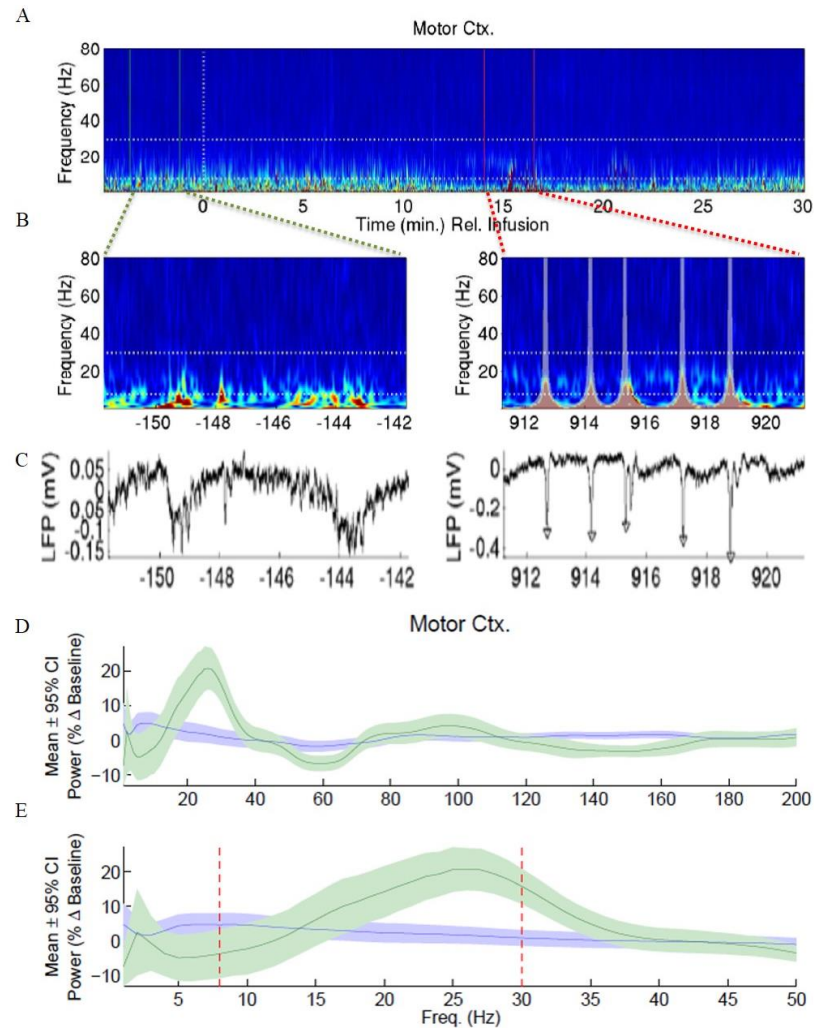


Figure (5-4) Recording in striatum and M1 by using carbachol infusion into the striatum and optogenetic silencing of M1 pyramidal cells (Emx-Arch transgenic mice).

M1 and striatal beta power not altered by M1 silencing

In order to assess the role of intrinsic M1 connectivity as well as the role of the cortico-basal ganglia pathways in the emergence of beta oscillations in striatum and M1 under conditions of high striatal cholinergic tone, we optogenetically silenced the excitatory neurons in the deep layers of M1.

This silencing took place an average of 10 mins after the end of carbachol infusion. Since this silencing effectively blocks cortico-striatal inputs to basal ganglia, we expect striatal beta oscillations to be diminished if the expression of striatal beta depends on these pathways. However, silencing M1 excitatory neurons did not significantly alter power in the beta frequency range in either striatum or M1 with respect to the laser-off condition (Fig. 5-5A, B). In striatum, the power at all frequencies above 10 Hz was non-significantly lowered most likely reflecting a general decrease in excitation due to loss of M1 excitatory input (Fig. 3). In M1, statistically significant decreases in oscillatory power with respect to the laser-off periods were noted only in the alpha and low gamma band (~ 35–60 Hz); all other frequencies above 10 Hz showed a non-significant lowering of power most likely representing a general decrease in excitation in M1 due to silencing of the excitatory neurons.

These results imply that post-carbachol striatal beta power is independent of cortico-basal ganglia input. Suggesting that basal ganglia may be the source of beta oscillations after striatal carbachol infusion. These results also suggest M1 beta oscillations are independent of local excitatory connections within M1 itself.

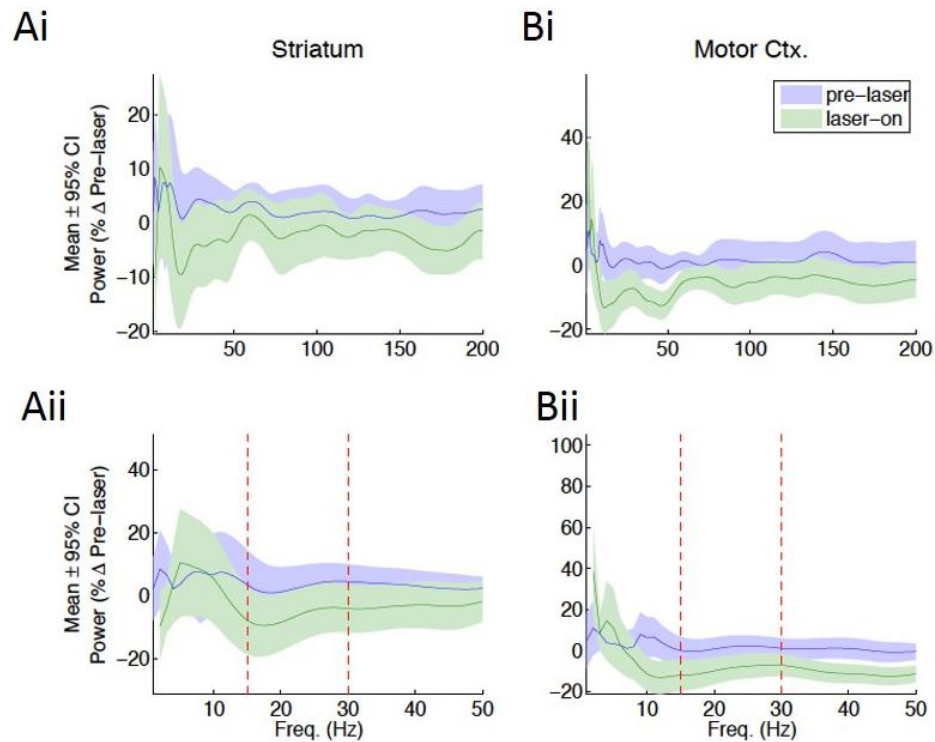


Figure (5-5) Recording in striatum and M1 by using carbachol infusion into the striatum and optogenetic silencing of M1 pyramidal cells (Emx-Arch transgenic mice).

5.4 Discussion:

Striatum as a potential generator of beta oscillations:

Increasing striatal cholinergic tone by the infusion of carbachol into normal mice elevates beta frequency oscillations in both striatum and M1. The elevation in LFP power is selective for the beta frequency range, with the peak of the elevation occurring in the beta range and very little elevation of power for frequencies outside the beta frequency range. We additionally find that optogenetic silencing of M1 excitatory neurons does not alter the beta power in either striatum or M1, or qualitatively change the phase relationships between these structures.

Our lab previous work suggests striatum has the intrinsic cellular and network connectivity to produce robust beta oscillations under conditions of elevated MSN excitability, including the condition of high striatal cholinergic tone [McCarthy et al., 2011].

Here we test this prediction by simultaneously measuring beta oscillations in paired recordings from striatum and M1. We find that striatal carbachol infusion produces exaggerated beta oscillations not only in striatum, but also in M1, demonstrating that the effect of high striatal cholinergic tone on beta oscillations is not limited to striatum.

However, because the frequency peak of the beta oscillation was slightly higher in M1 than striatum, these results suggest that the beta oscillations are not necessarily propagated unchanged from one structure to another in the CBT loop.

We additionally find that these elevated beta oscillations are not dependent on cortico-basal ganglia input: beta remains elevated after silencing deep layer excitatory neurons in M1, including neurons that form the cortico-striatal and hyperdirect pathways. We find that optogenetically silencing M1 excitatory neurons does not significantly decrease beta oscillations in either M1 or striatum. These results suggest that high striatal cholinergic tone is sufficient to produce exaggerated beta oscillations independent of M1 input. Our results suggest a basal ganglia origin for the carbachol-induced beta oscillations.

Furthermore, neither M1 nor striatal beta was significantly reduced after M1 silencing suggesting the elevated beta oscillations do not rely on input from cortex when striatal cholinergic tone is elevated. Since silencing M1 did not decrease beta oscillations in

either M1 or striatum, it seems likely that the elevated beta oscillations seen in cortex and striatum after striatal carbachol infusion do not originate in cortex. In the present study, striatal dopaminergic tone was not directly altered. Striatal carbachol may have an indirect suppressive effect on dopamine in striatum, however the suppression was not chronic and the elevation in beta usually came around 11 minutes after the end of the carbachol infusion.

In summary, our results demonstrate that striatal carbachol infusion acutely elevates beta oscillations simultaneously in striatum and M1 and that the elevation in beta is not dependent on cortico-basal ganglia projections. Our results support our previous modeling study suggesting striatum as a potential generator of beta oscillations. The link between elevated striatal cholinergic tone and elevated beta oscillations in cortico-striatal circuits highlights the potentially important role of elevated striatal cholinergic tone in mediating one of the major electrophysiological findings in the parkinsonian basal ganglia.

CHAPTER SIX: Conclusion and Future Work

Here, we demonstrate the promise of wide field optical imaging technology to measure more neurons in a large field of view, which is equal to 1.3 mm with a system optical resolution reaching to the theoretical maximum of 1.3 μm . This was enabled by the development of faster and more sensitive cameras, and new generation of genetically-encoded Sensor GCaMP6f that has high $\Delta F/F$, high signal to noise ratio, rapid rising time of ~ 48 millisecond and decay time of ~ 150 millisecond. Using this technology, we tracked calcium responses of myriad of neural activities that are relevant to behavior, and our data show that Calcium responses could resolve behavioral events separated by hundreds of millisecond. In addition, we demonstrate that our system provides a robust optical platform to image calcium responses induced by mechanical blast. We found heterogeneous neuron responses upon blast, which are informative and novel in the field of traumatic brain injury research and could not be measured by other techniques, such as fMRI or CT scan. These results can help understand the transient effect of mechanical blast at the cellular level, and provide evidence on how fast neural circuitry can recover. Finally, we investigate the capability of using optogenetics to manipulate neural activity of basal ganglia network to understand the source and function of enhanced beta oscillation. The experimental outcomes revealed that motor cortex silencing did not affect beta oscillation in the striatum of the basal ganglia.

As we demonstrated in this dissertation, these optogenetics platform provide a wealth of information of how neural circuits respond during cognitive behavior, and how controlling neural activity in disease model could provide us with more information about

how a neural network functions. Integrated all optical control and imaging platform of neural activity as demonstrated here can provide a high-throughput platform for quantitative understanding of neural circuitry interactions.

References.

- Adelman, T.L. & Tank, D.W. et al. (2007). “Imaging large-scale neural activity with cellular resolution in awake, mobile mice”. Neuron 56, 43–57.
- Akerboom, J. et al. (2012). “Optimization of a GCaMP calcium indicator for neural activity imaging”. Journal of Neuroscience 32, 13819–13840.
- Andermann, M. L., Kerlin, A. M. & Reid, R. C. (2010). “Chronic cellular imaging of mouse visual cortex during operant behavior and passive viewing”. Frontiers in Cellular Neuroscience 4, 3.
- Baker, S.N., et al. (2015). “Pathways mediating functional recovery”. Progress in Brain Research 218, 389–412.
- Barnes, C. A., McNaughton, B. L. & O’Keefe, J. (1983). “Loss of place specificity in hippocampal complex spike cells of senescent rat”. Neurobiology of Aging 4, 113–119.
- Beaurepaire, E. & Mertz, J. et al. (2002). “Epifluorescence collection in two-photon microscopy”. Applied Optics 41, 5376–5382.
- Belmont, Agar, & Azouvi, (2009). “Subjective fatigue, mental effort, and attention deficits after severe traumatic brain injury”. Neurorehabilitation and Neural Repair 23, 939–944.
- Berger, T. W., Rinaldi, P. C., Weisz, D. J. & Thompson, R. F. (1983). “Single-unit analysis of different hippocampal cell types during classical conditioning of rabbit nictitating membrane response”. Journal of Neurophysiology 50, 1197–1219.
- Bevan M. D., et al. (2002). “Move to the rhythm: oscillations in the subthalamic nucleus-external globus pallidus network”. Trends in Neurosciences 25, 525–531.
- Bigler ED. (2013). “Traumatic brain injury, neuroimaging, and neurodegeneration”. Frontiers in Human Neuroscience 7, 395.
- Brown, P. et al. (2004). “Neuronal Oscillations in the Basal Ganglia and Movement Disorders: Evidence from Whole Animal and Human Recording”. Journal of Neuroscience 24(42), 9240–9243.
- Cagnan, H., E.P. Duff, and P. Brown (2015). “The relative phases of basal ganglia activities dynamically shape effective connectivity in Parkinson's disease”. Brain 138(Pt 6), 1667–1678.
- Chen, T. W. et al. (2013). “Ultrasensitive fluorescent proteins for imaging neuronal activity”. Nature 499, 295–300.

- Connor, J. A. & Llinas, R. R. et al. (1988). “Spatially resolved calcium dynamics of mammalian Purkinje cells in cerebellar slice”. Science 242, 773–777.
- Cowley, B. R. et al. (2013). “DataHigh: graphical user interface for visualizing and interacting with high-dimensional neural activity”. Journal of Neural Engineering 10, 066012.
- Damodaran, S., et al. (2015). “Desynchronization of fast-spiking interneurons reduces beta-band oscillations and imbalance in firing in the dopamine-depleted striatum”. Journal of Neuroscience 35(3), 1149–1159.
- DeBoer et al., (1996) ‘Quality of life in patients with Parkinson's disease: development of a questionnaire’ Journal of Neurology, Neurosurgery, and Psychiatry 61,70–74.
- DeBoer, P., et al. (1996). “Spontaneous release of acetylcholine in striatum is preferentially regulated by inhibitory dopamine D2 receptors”. European Journal of Pharmacology 317(2–3), 257–262.
- Delorenzo et al. (2005). “Cellular mechanisms underlying acquired epilepsy: The calcium hypothesis of the induction and maintenance of epilepsy” Pharmacology & Therapeutics 105(3), 229–266.
- Denk, W. & Svoboda, K et al. (1997). “Photon upmanship: why multiphoton imaging is more than a gimmick”. Neuron 18, 351–357.
- Dombeck, D. A., Harvey, C. D., Tian, L., Looger, L. L. & Tank, D. W. (2010). “Functional imaging of hippocampal place cells at cellular resolution during virtual navigation”. Nature Neuroscience 13, 1433–1440.
- Dombeck, D. A., Khabbaz, A. N., Collman, F., Adelman, T. L. & Tank, D. W. (2007). “Imaging large-scale neural activity with cellular resolution in awake, mobile mice”. Neuron 56, 43–57.
- Eichenbaum, H., Wiener, S. I., Shapiro, M. L. & Cohen, N. J. (1989). “The organization of spatial coding in the hippocampus: a study of neural ensemble activity”. Journal of Neuroscience 9, 2764–2775.
- Eusebio, A., Cagnan, H., & Brown, P. (2012). “Does suppression of oscillatory synchronisation mediate some of the therapeutic effects of DBS in patients with Parkinson’s disease”. Frontiers in Integrative Neuroscience, 6, 47.
<http://doi.org/10.3389/fnint.2012.00047>.
- Faul, F., Erdfelder, E., Lang, A. G. & Buchner, A (2007). “G*Power 3: a flexible statistical power analysis program for the social, behavioral, and biomedical sciences”. Behavior Research Methods 39, 175–191.

- Flusberg, B.A. et al. (2008). “High-speed, miniaturized fluorescence microscopy in freely moving mice”. Nature Methods 5, 935–938.
- Freeman, J. et al. (2014). “Mapping brain activity at scale with cluster computing”. Nature Methods 11, 941–950.
- Gallese, V., Fadiga, L., Fogassi, L. & Rizzolatti, G. (1996). “Action recognition in the premotor cortex. Brain”. Brain 119(Pt. 2), 593–609.
- Ghosh, K. K. et al. (2011). “Miniaturized integration of a fluorescence microscope”. Nature Methods 8, 871–878.
- Glickfeld, L. L., Andermann, M. L., Bonin, V. & Reid, R. C. (2013). “Cortico-cortical projections in mouse visual cortex are functionally target specific”. Nature Neuroscience 16, 219–226.
- Green, J. T. & Arenos, J. D. (2007). “Hippocampal and cerebellar single-unit activity during delay and trace eyeblink conditioning in the rat”. Neurobiology of Learning and Memory 87, 269–284.
- Grinvald, A., Lieke, E., Frostig, R. D., Gilbert, C. D. & Wiesel, T. N. (1986). “Functional architecture of cortex revealed by optical imaging of intrinsic signals”. Nature 324, 361–364.
- Hafting, T., Fyhn, M., Molden, S., Moser, M. B. & Moser, E. I. (2005). “Microstructure of a spatial map in the entorhinal cortex”. Nature 436, 801–806.
- Hamel, E. J., Grewe, B. F., Parker, J. G. & Schnitzer, M. J. (2015). “Cellular level brain imaging in behaving mammals”. An engineering approach. Neuron 86, 140–159.
- Hammond et al., (2007). “Pathological synchronization in Parkinson’s disease: Networks, models and treatments”. Trends in Neurosciences 30, 357–364.
- Han, X. (2012). “In vivo application of optogenetics for neural circuit analysis”. ACS Chemical Neuroscience 3, 577–584.
- Hattori, S., Chen, L., Weiss, C. & Disterhoft, J. F. (2015). “Robust hippocampal responsivity during retrieval of consolidated associative memory”. Hippocampus 25, 655–669.
- Heim, N. & Griesbeck, O. et al. (2004). “Genetically encoded indicators of cellular calcium dynamics based on troponin C and green fluorescent protein”. Journal of Biological Chemistry 279, 14280–14286.
- Hopt, A. & Neher, E. (2001). “Highly nonlinear photodamage in two-photon fluorescence microscopy”. Biophysical Journal 80, 2029–2036.

- Huber, D. et al. (2012). “Multiple dynamic representations in the motor cortex during sensorimotor learning”. Nature 484, 473–478.
- Ikarashi, Y., et al. (1997). “Regulation of dopamine D1 and D2 receptors on striatal acetylcholine release in rats”. Brain Research Bulletin 43(1): 107–115.
- Johansson, Berglund, & Rönnbäck, (2009). “Mental fatigue and impaired information processing after mild and moderate traumatic brain injury”. Brain Injury 23, 1027–1040.
- Jung, J. & Schnitzer, M. et al. (2003). “Multiphoton endoscopy”. Optics Letters 28, 902–904.
- Kerr, J.N. & Helmchen, F. et al. (2004). “Sulforhodamine 101 as a specific marker of astroglia in the neocortex in vivo”. Nature Methods 1, 31–37.
- Kerr, R. et al. (2000). “Optical imaging of calcium transients in neurons and pharyngeal muscle of *C. elegans*”. Neuron 26, 583–594.
- Kishimoto, Y. et al. (2001). “Impairment of eyeblink conditioning in GluRdelta2-mutant mice depends on the temporal overlap between conditioned and unconditioned stimuli”. European Journal of Neuroscience 14, 1515–1521.
- Kishimoto, Y., Nakazawa, K., Tonegawa, S., Kirino, Y. & Kano, M. (2006). “Hippocampal CA3 NMDA receptors are crucial for adaptive timing of trace eyeblink conditioned response”. Journal of Neuroscience 26, 1562–1570.
- Kohl, Wylie, Genova, Hillary, & Deluca, (2009). “The neural correlates of cognitive fatigue in traumatic brain injury using functional MRI”. Brain Injury 23, 420–432.
- Kreitzer A. C. et al. (2009). “Physiology and pharmacology of striatal neurons”. Annual Review of Neuroscience 32, 127–147.
- Lee E. Goldstein (2012). “Chronic Traumatic Encephalopathy in Blast-Exposed Military Veterans and a Blast Neurotrauma Mouse Model”. Science Translational Medicine. 4 (134), 134ra60.
- Leventhal, D.K., et al. (2012). Basal ganglia beta oscillations accompany cue utilization”. Neuron. 73(3), 523–36.
- Levy, W. B., Sanyal, A., Rodriguez, P., Sullivan, D. W. & Wu, X. B. (2005). “The formation of neural codes in the hippocampus: trace conditioning as a prototypical paradigm for studying the random recoding hypothesis”. Biological Cybernetics 92, 409–426.
- Lovett-Barron, M. et al. (2014). “Dendritic inhibition in the hippocampus supports fear learning”. Science 343, 857–863.

- Lystad RP, Pollard H. (2009). "Functional neuroimaging: a brief overview and feasibility for use in chiropractic research". Journal of the Canadian Chiropractic Association 53, 59–72.
- Magill PJ, et al. (2001). "Dopamine regulates the impact of the cerebral cortex on the subthalamic nucleus-globus pallidus network". Neuroscience 106(2), 313–330.
- Mark J Schnitzer et al. (2011). "Miniaturized integration of a fluorescence microscope", Nature Methods 8, 871–878.
- Markowitz, J. E. et al. (2015). "Mesoscopic patterns of neural activity support songbird cortical sequences". PLoS Biology 13, e1002158.
- McEchron, M. D. & Disterhoft, J. F. (1997). "Sequence of single neuron changes in CA1 hippocampus of rabbits during acquisition of trace eyeblink conditioned responses". Journal of Neurophysiology 78, 1030–1044.
- McEchron, M. D. & Disterhoft, J. F. (1999). "Hippocampal encoding of non-spatial trace conditioning". Hippocampus 9, 385–396.
- McEchron, M. D., Weible, A. P. & Disterhoft, J. F. (2001). "Aging and learning-specific changes in single-neuron activity in CA1 hippocampus during rabbit trace eyeblink conditioning". Journal of Neurophysiology 86, 1839–1857.
- Modi, M. N., Dhawale, A. K. & Bhalla, (2014). "U. S. CA1 cell activity sequences emerge after reorganization of network correlation structure during associative learning". Elife 3, e01982.
- Moyer, J. R. Jr., Deyo, R. A. & Disterhoft, J. F. (1990). "Hippocampectomy disrupts trace eye-blink conditioning in rabbits". Behavioral Neuroscience 104, 243–252.
- Mukamel, E. A., Nimmerjahn, A. & Schnitzer, M. J. (2009). "Automated analysis of cellular signals from large-scale calcium imaging data". Neuron 63, 747–760.
- Munera, A., Gruart, A., Munoz, M. D., Fernandez-Mas, R. & Delgado-Garcia, J. M. (2001). "Hippocampal pyramidal cell activity encodes conditioned stimulus predictive value during classical conditioning in alert cats". Journal of Neurophysiology 86, 2571–2582.
- Nakai, J., Ohkura, M. & Imoto, K. et al. (2004). "A high signal-to-noise Ca²⁺ probe composed of a single green fluorescent protein". Nature Biotechnology 19, 137–141.
- O'Keefe, J. & Dostrovsky, J. (1971). "The hippocampus as a spatial map. Preliminary evidence from unit activity in the freely-moving rat". Brain Research 34, 171–175.
- O'Keefe, J. (1979). "A review of the hippocampal place cells". Progress in Neurobiology 13, 419–439.

- Oheim, M., E., Mertz, J. & Charpak, S. et al. (2002). "Two photon microscopy in brain tissue: parameters influencing the imaging depth". Journal of Neuroscience Methods 111, 29–37.
- Ohki, K., Kara, P. & Reid, R. C. et al. (2005). "Functional imaging with cellular resolution reveals precise micro-architecture in visual cortex". Nature 433, 597–603.
- Otazu, G. H., Chae, H., Davis, M. B. & Albeanu, D. F. (2015). "Cortical Feedback Decorrelates Olfactory Bulb Output in Awake Mice". Neuron 86, 1461–1477.
- Patterson, G. H. & Piston, D. W. (2000). "Photobleaching in two-photon excitation microscopy". Biophysical Journal 78, 2159–2162.
- Petreaanu, L. et al. (2012). "Activity in motor-sensory projections reveals distributed coding in somatosensation". Nature 489, 299–303.
- Plenz D., et al. (1999). "A basal ganglia pacemaker formed by the subthalamic nucleus and external globus pallidus". Nature 400, 677–682.
- Priori et al., (2004). "Rhythm-specific pharmacological modulation of subthalamic activity in Parkinson's disease". Experimental Neurology 189 (2):369–79.
- Raghupathi et al. (2004). "Cell Death Mechanisms Following Traumatic Brain Injury". Brain Pathology 14(2), 215–222.
- Ramanathan S, Hanley JJ, Deniau JM, Bolam JP (2002) "Synaptic convergence of motor and somatosensory cortical afferents onto GABAergic interneurons in the rat striatum". Journal of Neuroscience 22, 8158–8169.
- Raza et al. (2001). "Long-term alteration of calcium homeostatic mechanisms in the pilocarpine model of temporal lobe epilepsy". Brain Research 903(1–2), 1–12.
- Redish, A. D. et al. (2001). "Independence of firing correlates of anatomically proximate hippocampal pyramidal cells". Journal of Neuroscience 21, RC134.
- Sabatini, B. L., Oertner, T. G. & Svoboda, K. et al. (2002). "The life cycle of Ca²⁺ ions in dendritic spines". Neuron 33, 439–452.
- Sahuquillo et al. (2001). "Current aspects of pathophysiology and cell dysfunction after severe head injury". Current Pharmaceutical Design 7(15), 1475–1503.
- Sakamoto, T. et al. (2005). "Role of hippocampal NMDA receptors in trace eyeblink conditioning". Brain Research 1039, 130–136.
- Sawinski, J. et al. (2009). "Visually evoked activity in cortical cells imaged in freely moving animals". Proceedings of the National Academy of Sciences of the United States of America 106, 19557–19562.

- Sayeg, M. K. et al. (2015). Rationally Designed MicroRNA-Based Genetic Classifiers Target Specific Neurons in the Brain. ACS Synthetic Biology 4, 788–795.
- Schultz, W., Dayan, P. & Montague, P. R. (1997). “A neural substrate of prediction and reward”. Science 275, 1593–1599.
- Shen W., et al. (2008). “Dichotomous dopaminergic control of striatal synaptic plasticity”. Science 321, 848–851.
- Silberstein P, et al. (2005). “Cortico-cortical coupling in Parkinson's disease and its modulation by therapy”. Brain 128, 1277–1291.
- Solomon, P. R., Vander Schaaf, E. R., Thompson, R. F. & Weisz, D. J. (1986). “Hippocampus and trace conditioning of the rabbit's classically conditioned nictitating membrane response”. Behavioral Neuroscience 100, 729–744.
- St-Pierre, F. et al. (2014). “High-fidelity optical reporting of neuronal electrical activity with an ultrafast fluorescent voltage sensor”. Nature Neuroscience 17, 884–889.
- Sun, X. R. et al. (2013). “Fast GCaMPs for improved tracking of neuronal activity”. Nature Communications 4, 2170.
- Svoboda, K., Denk, W., Kleinfeld, D. & Tank, D.W. et al. (1997). “*In vivo* dendritic calcium dynamics in neocortical pyramidal neurons”. Nature 385, 161–165.
- Tada, M., Takeuchi, A., Hashizume, M., Kitamura, K. & Kano, M. (2014). “A highly sensitive fluorescent indicator dye for calcium imaging of neural activity in vitro and in vivo”. European Journal of Neuroscience 39, 1720–1728.
- Tank, D. & Denk, W. et al. (2001). “A miniature head-mounted two-photon microscope: high-resolution brain imaging in freely moving animals”. Neuron 31, 903–912.
- Tavalin et al. (1995). “Mechanical perturbation of cultured cortical neurons reveals a stretch-induced delayed depolarization” Journal of Neurophysiology 73(6), 2767–2763.
- Thevenaz, P., Ruttimann, U. E. & Unser, M. (1998). “A pyramid approach to subpixel registration based on intensity”. IEEE Transactions on Image Processing 7, 27–41.
- Tian, L. et al. (2009).” Imaging neural activity in worms, flies and mice with improved GCaMP calcium indicators”. Nature Methods 6, 875–881.
- Tsai-Wen Chen & Douglas S. Kim. et al. (2013). “Ultra-sensitive fluorescent proteins for imaging neuronal activity” Nature 499, 295–300.
- Tseng, W., Guan, R., Disterhoft, J. F. & Weiss, C. (2004). “Trace eyeblink conditioning is hippocampally dependent in mice”. Hippocampus 14, 58–65.

- Wachowiak, M. et al. (2013). “Optical dissection of odor information processing in vivo using GCaMPs expressed in specified cell types of the olfactory bulb”. Journal of Neuroscience 33, 5285–5300.
- Wang, Y. et al. (2004). “Stereotyped odor-evoked activity in the mushroom body of *Drosophila* revealed by green fluorescent protein-based Ca²⁺ imaging”. Journal of Neuroscience 24, 6507–6514.
- Wilt, B.A. et al. (2009). “Advances in light microscopy for neuroscience”. Annual Review of Neuroscience 32, 435–506.
- Xu, C. & Webb, W.W. et al. (1996). “Measurement of two-photon excitation cross sections of molecular fluorophores with data from 690 to 1,050 nm”. Journal of the Optical Society of America. B, Optical Physics 13, 481–491.
- Xu, N. L. et al. (2012). “Nonlinear dendritic integration of sensory and motor input during an active sensing task”. Nature 492, 247–251.
- Yamawaki, N., et al. (2008). “Pharmacologically induced and stimulus evoked rhythmic neuronal oscillatory activity in the primary motor cortex in vitro. Neuroscience”. 151(2), 386–395.
- Zariwala, H. A. et al. (2012). “A Cre-dependent GCaMP3 reporter mouse for neuronal imaging in vivo”. Journal of Neuroscience 32, 3131–3141.
- Ziv, Y. et al. (2013). “Long-term dynamics of CA1 hippocampal place codes”. Nature Neuroscience 16, 264–266.
- Zomeran & van den Burg, (1985). “Residual complaints of patients two years after severe head injury”. Journal of Neurology, Neurosurgery, and Psychiatry 48, 21–28.

Curriculum Vitae
Ali Ibrahim Ali Mohammed

Education

Ph.D.	Boston University	2016
M.Sc.	Texas Tech University	2011
B.Sc	Helwan University	2001

Research (PhD Level):

- Development and Application of an Optogenetics Platform for Controlling and Imaging a Large Number of Individual Neurons.

Research (Master Level):

- Reorientational Dynamics of Ionic Liquid and Nonconfinement Effects Studied by Optical Kerr Effect Spectroscopy.
- Studies on Bistability of a Dissipative Optical Medium inside a Resonator.
- Study Myelin Basic Protein interaction with lipid by Solid state NMR Spectroscopy.

PUBLICATIONS:

Mohammed, A. I. *et al.* An integrative approach for analyzing hundreds of neurons in task performing mice using wide-field calcium imaging. *Sci. Rep.* **6**, 20986; doi: 10.1038/srep20986 (2016)

Young adult born neurons enhance hippocampal dependent performance via influences on bilateral networks (eLife – Submitted)

Increased striatal cholinergic tone augments beta oscillations and perturbs phase relationships in the cortico-basal ganglia loop (In progress).

Impact of Mild Traumatic Brain Injury on Neuronal Networks activity in wake behaving animal (In preparation).

Effect of Cation Symmetry on the Morphology and Physicochemical Properties of Imidazolium Ionic Liquids, W. Zheng*, A. Mohammed*, L. G. Hines Jr., D. Xiao, O. J. Martinez, R. A. Bartsch, O. Russina, A. Triolo, and E. L. Quitevis, *J. Phys. Chem. B*, 115, 6572-6584, (2011). Published on Web 05/02/11.

Effect of Spectral Profile of a Driving Field on the Bistability of a Dissipative Medium inside a Resonator. *Optics & Laser Technology*, 39 (2007) 1243–1253 M.M. EL-Nicklawy, A.F. Hassan, A.T. Matar, A.A. Hemeda, A.I. Ali.

Studies on the Bistability of a Dissipative Medium inside a Resonator. *Egypt. J.Solids*, Vol. (29), No. (1), (2006) M. M. EL-Nicklawy, A.F. Hassan, A. T. Matar, A.Hemeda, and A. I. Ali.

Posters:

Effect of Cation Symmetry on the Morphology and Physicochemical Properties of Imidazolium Ionic Liquids, American Chemical Society Meeting August (2009).

Optical Heterodyne optical Kerr Effect spectroscopy on ionic liquid. Texas Tech University (2009).

Increased Striatal Cholinergic Tone modulates distinct beta band sub-frequencies and phase relationships in the cortical basal ganglia network, Society of Neuroscience (2015).